

Design and Development of a UAV System for Multispectral Imaging and Remote Sensing Applications

by

Jorge Marin Marcano

A thesis submitted in partial fulfillment of the requirements for the degree of

Master of Science

in

Computer Engineering

Department of Electrical and Computer Engineering

University of Alberta

© Jorge Marin Marcano, 2018

Abstract

The increasing use of the Unmanned Aerial Vehicles (UAVs) over the past few years has opened the door to a large number of applications in research, commercial, and industrial areas. UAVs have become an efficient, cost effective, and environmentally friendly (less or zero CO₂ emissions) platform for remote sensing compared to manned vehicles. One major field in this category is multispectral sensing. Commercial solutions of UAV-compatible multispectral cameras are available but tend to have a high cost and, in most cases, lack certain flexibility when it comes to custom development. This thesis is organized in three basic sections. It begins with the development of a modular fixed-wing UAV that includes a customized airframe, integrated avionics with a custom UAV system board with redundant power supply, and single board computer (SBC) for payload interfacing. The other two sections of this thesis are focused on the design, development, and testing of two revisions of a custom multispectral imaging system.

The customized fixed-wing airframe was redesigned aiming for modularity and reliability. The open-source UAV system board integrates all essential sensors and components in a small and compact board, reducing the amount of wiring and connectors, which in turn reduces weight and increases reliability. The UAV system board includes a detachable and novel redundant power supply board that provides main and backup power regulation. The complete UAV system design is presented as an efficient, and flexible platform.

The multispectral imaging system is based on multiple USB 2.0 camera modules and optical filters. The first iteration, or proof of concept, introduces a 3-band multispectral imaging system based on 3 rolling shutter cameras synchronized by software, with optical filters for the green, red, and near-

infrared bands. The cameras were controlled by the SBC on board of the UAV. The imaging system was tested over a grass field, and the images collected were post-processed. Resulting images were aligned and NDVI images were produced where it was possible to detect vegetation and identify different levels of vegetation stress. This system proved to be a low cost and simple, yet effective approach for custom UAV multispectral imaging.

The next evolution of the system is a 12-band multispectral imaging platform based on USB 2.0 camera modules. Cameras used in this revision have a global shutter and a trigger functioning mode that allows hardware synchronization. A novel bridge board was designed to integrate all USB communications via USB HUBs and also include a microcontroller unit (MCU) in charge of triggering the cameras. The USB HUB network has selectable routes for grouping cameras to different upstream USB ports depending on the bandwidth requirements of the application. The system was tested and characterized for the maximum number of simultaneous cameras per root USB port depending on camera configuration. With the highly integrated bridge board the overall size and weight of the system was reduced, making it compatible with most UAVs. Software was also developed, based on third party tools, that allows extensive configuration of the cameras and control over the imaging system.

The result of this work introduces a detailed methodology for UAV systems development, introduces a comprehensive UAV system board, and explores the capacities of USB 2.0 camera modules as part of complex imaging systems. The hardware and software platforms developed throughout this thesis are cost effective and efficient solutions that allow customization and expansion, making them an ideal development tool for UAV systems and UAV multispectral imaging applications.

Preface

The work in this thesis, including the conceptualization, design, implementation, data processing, and analysis, was carried out by me under the supervision of Dr. Duncan Elliott from the Department of Electrical and Computer Engineering at the University of Alberta.

The work was done in working space provided by the University of Alberta Aerial Robotics Group (UAARG), and later in Dr. Michael Lipsett's laboratory, from the Department of Mechanical Engineering at the University of Alberta.

Acknowledgements

I would first like to thank my supervisor Dr. Duncan Elliott from the Electrical and Computer Engineering Department of the University of Alberta for his insights and guidance, and Dr. Michael Lipsett from the Mechanical Engineering Department at the University of Alberta for his support.

I would also like to thank the University of Alberta Aerial Robotics Group (UAARG) for their help during the first steps of the project. Many thanks to Andrew Jowsey, Sebastian Werner, Cindy Xiao, and Brian Hinrichsen. Their knowledge and experience were of great importance. I would like to specially thank Rijesh Augustine for his vital contributions throughout the project. I would also like to acknowledge Stream Technologies Inc. for their valuable support in the final stages of the project.

Finally, I must express my profound gratitude to my family, friends, and to my loving spouse, for their continuous support and encouragement throughout my years of study and through the process of conducting research and writing this thesis. This accomplishment would not have been possible without them. Thank you.

Jorge Marin.

Contents

| | |
|--|-------------|
| List of Tables | x |
| List of Figures | xii |
| List of Abbreviations | xvii |
| Chapter 1: Introduction | 1 |
| 1.1 Objective of the Thesis | 2 |
| 1.2 Organization of the Thesis | 3 |
| Chapter 2: Literature Review | 4 |
| 2.1 Imaging Systems and Cameras | 4 |
| 2.1.1 Fundamentals of Optics and Imaging Systems | 4 |
| 2.1.2 Image Sensor | 8 |
| 2.1.2.1 CCD vs. CMOS Technologies | 8 |
| 2.1.2.2 Rolling vs. Global Shutter | 9 |
| 2.1.2.3 Performance Metrics of Image Sensors | 9 |
| 2.1.3 Lenses | 11 |
| 2.1.4 Modulation Transfer Function | 11 |
| 2.1.4.1 Resolution | 12 |
| 2.1.4.2 Contrast | 14 |
| 2.1.4.3 Slanted-Edge MTF Measurement | 17 |

| | | |
|-------------------|--|-----------|
| 2.1.5 | USB Camera Modules | 19 |
| 2.1.5.1 | USB Video Class (UVC) | 19 |
| 2.1.5.2 | Video for Linux Two (V4L2) API | 20 |
| 2.1.5.3 | GStreamer | 20 |
| 2.2 | Spectral Imaging | 21 |
| 2.2.1 | Vegetation, Soil and Water Reflectance | 22 |
| 2.2.2 | Landsat Thematic Mapper | 23 |
| 2.2.3 | Lightweight UAV-Compatible Multispectral Imaging Systems | 24 |
| 2.3 | UAV-Based Spectral Remote Sensing | 27 |
| 2.3.1 | Crop Inspection and Precision Agriculture | 27 |
| 2.3.2 | Surface and Soil Study | 30 |
| 2.3.3 | Surface Hydrocarbon Detection | 30 |
| 2.3.4 | Environmental Monitoring | 31 |
| 2.3.5 | Archaeology | 31 |
| Chapter 3: | UAV Development | 33 |
| 3.1 | UAV Electronic System | 33 |
| 3.1.1 | UAV System Board | 34 |
| 3.1.1.1 | Microcontroller Unit (MCU) | 35 |
| 3.1.1.2 | Inertial Measurement Unit (IMU) | 35 |
| 3.1.1.3 | GPS | 36 |
| 3.1.1.4 | XBee and Data-logger | 36 |
| 3.1.1.5 | PWM Outputs | 36 |
| 3.1.1.6 | Power Regulation | 36 |
| 3.1.1.7 | Additional Features | 37 |
| 3.1.2 | Redundant Power Supply Board | 38 |
| 3.1.2.1 | Principle of Operation | 40 |
| 3.1.3 | Firmware and Ground Control Station (GCS) | 43 |
| 3.2 | Payload Computer | 44 |

| | | |
|-------------------|---|-----------|
| 3.3 | UAV Avionics Module | 45 |
| 3.4 | Airframe | 45 |
| 3.4.1 | Falcon I | 47 |
| Chapter 4: | Proof of Concept Multispectral Imaging System | 53 |
| 4.1 | USB Camera Modules | 53 |
| 4.1.1 | Selection and Evaluation | 54 |
| 4.1.2 | Software Development | 55 |
| 4.1.3 | Lens Testing - Modulation Transfer Function | 57 |
| 4.2 | 3-Band Multispectral Imaging System | 58 |
| 4.2.1 | Cameras and Lenses | 59 |
| 4.2.2 | Optical Filters | 61 |
| 4.2.3 | Software Development | 63 |
| 4.2.4 | UAV Setup | 65 |
| 4.2.5 | Flight Campaigns | 66 |
| 4.2.6 | Image Alignment | 67 |
| 4.2.7 | Vegetation Indices | 70 |
| Chapter 5: | 12-Band Multispectral Imaging Platform | 73 |
| 5.1 | System Concept | 73 |
| 5.2 | USB Camera Modules | 74 |
| 5.2.1 | Optical Filters | 76 |
| 5.3 | Camera Bridge Board | 76 |
| 5.3.1 | USB HUB | 79 |
| 5.3.2 | Trigger | 80 |
| 5.4 | Software | 81 |
| 5.5 | Testing | 81 |
| 5.6 | Costs | 85 |
| 5.7 | Focusing | 86 |
| 5.8 | Image Alignment | 89 |

| | |
|--|------------|
| Chapter 6: Conclusions and Future Work | 91 |
| 6.1 Future Work | 93 |
| Bibliography | 95 |
| Appendix A: UAV System Board User Guide | 105 |
| Appendix B: Camera Bridge Board Schematics | 154 |
| Appendix C: Camera Bridge Board Bill-of-Materials | 167 |
| Appendix D: 3D Printer Settings | 171 |

List of Tables

| | | |
|-----|---|----|
| 2.1 | Features comparison between CCD and CMOS image sensors. | 9 |
| 2.2 | Spatial frequency unit conversion chart. | 15 |
| 2.3 | Landsat Thematic Mapper Bands for Vegetation Monitoring. | 24 |
| 2.4 | Comparison of common multispectral imaging systems. | 26 |
| 3.1 | UAV System Board Features | 38 |
| 3.2 | Technical Specifications of the ODROID-C2 | 44 |
| 4.1 | Features of the ELP-USB500W02M camera. | 54 |
| 4.2 | Settings of the ELP-USB500W02M camera. | 55 |
| 4.3 | Frame Rates for the ELP-USB500W02M camera based on output video format and resolution. | 56 |
| 4.4 | Results of different M12 lenses tested using the slanted-edge MTF method. | 57 |
| 4.5 | Features of the ELP-USB130W01MT-B/W camera. | 59 |
| 4.6 | Settings of the ELP-USB130W01MT-B/W camera. | 60 |
| 4.7 | Frame Rates for the ELP-USB130W01MT-B/W camera based on output video format and resolution. | 60 |
| 4.8 | Technical details of the optical filters. | 62 |
| 4.9 | Flight campaigns details. | 67 |
| 5.1 | Specifications of the DMM 42BUC03-ML camera. | 74 |
| 5.2 | Video formats and frame rates available in the DMM 42BUC03-ML camera. | 76 |

| | | |
|-----|--|-----|
| 5.3 | Settings of the DMM 42BUC03-ML camera. | 76 |
| 5.4 | Test results of USB traffic with different configurations. Cameras were connected to a single USB upstream port and triggered simultaneously. Data transferred based on a single frame from each camera. | 82 |
| 5.5 | Comparison of common multispectral imaging systems with the system presented in this work. | 84 |
| 5.6 | General costs of components for the multispectral imaging system hardware. . . . | 85 |
| 5.7 | Costs per set/unit based on order quantity for Bridge Board bare PCB and BOM. . . | 85 |
| D.1 | 3D printer settings. | 171 |

List of Figures

| | | |
|------|---|----|
| 2.1 | Illustration of the fundamental parameters of an imaging system. | 5 |
| 2.2 | Geometry of a basic optics system using the thin-lens model. | 5 |
| 2.3 | Angle of view and its horizontal, vertical and diagonal components [18]. | 6 |
| 2.4 | Focal length and angle of view of a “full frame” (35mm) image sensor [19]. | 7 |
| 2.5 | Conversion and charge transferring principles between CCD and CMOS technologies [20]. | 8 |
| 2.6 | Comparison between rolling shutter and global shutter captures on moving target [21]. | 10 |
| 2.7 | Perfectly clear pattern before (left) and after (right) passing through a low resolution lens [25]. | 12 |
| 2.8 | Resolving two black stripes. If the space between the stripes is too small (a) the camera sensor will not be able to resolve them as separate stripes [25]. | 13 |
| 2.9 | Different levels of contrast plotted as a square wave [25]. | 14 |
| 2.10 | Contrast comparison in resulting images at low (a) and high (b) frequency, and MTF plot (c) [27]. | 16 |
| 2.11 | SFR target with horizontal and vertical (highlighted) slanted edges. | 17 |
| 2.12 | Flowchart of the operations in the edge gradient analysis. | 18 |
| 2.13 | Different MTF shapes and their meaning. | 18 |
| 2.14 | Diagram of GStreamer components [38]. | 21 |
| 2.15 | Illustration of hyperspectral imaging. Each pixel in the image forms the spectrum trough imaged wavebands. | 21 |

| | | |
|------|--|----|
| 2.16 | Comparison of band classifications in multispectral (few wide bands) and hyperspectral (several narrow bands) models. Units are in micrometers for the multispectral ranges. | 22 |
| 2.17 | Reflectance spectrum of water, soil and vegetation. | 22 |
| 2.18 | Reflectance spectrum of water, soil and vegetation together with the Landsat TM bands in the 0-2.5 μm range. | 23 |
| 2.19 | (a) Tetracam Mini MCA6. (b) Sentek GEMS. (c) Sentera QUAD. (d) Parrot Sequoia. | 25 |
| 2.20 | Comparison of spectral bands used in each camera. | 26 |
| 3.1 | Block diagram of the UAV system board hardware. | 35 |
| 3.2 | UAV system board. 90x52mm 4-layers PCB with a weight of 29 grams. A detailed manual and user guide for the board can be found in Appendix A. | 37 |
| 3.3 | Redundant Power supply module. 41x46mm 4-layers PCB with a weight of 14 grams. There are four voltage regulators, from bottom left and clockwise: autopilot main, payload, servo backup, and autopilot backup. | 39 |
| 3.4 | Redundant Power supply module block diagram. Greyed blocks and dashed lines are inactive. (a) Normal power operation mode: all systems are on and powered from main battery. (b) Backup power operation mode: autopilot and servos are powered from backup battery; motor, payload and Electronic Speed Controller (ESC) / Battery Eliminator Circuit (BEC) are off. | 40 |
| 3.5 | Main and backup power supplies connection diagram. Both power supplies are connected in parallel and there is a voltage difference between the two, where V_{MAIN} is slightly higher than V_{BACKUP} when in normal operation mode. | 41 |
| 3.6 | Variation of the current sank by the backup voltage regulator circuit (i_S) with the voltage difference $\Delta V = V_{MAIN} - V_{BACKUP}$, including the point of current inversion for a low ΔV in which i_S becomes negative. | 41 |
| 3.7 | Variation of the current sank by the backup voltage regulator circuit (i_S) with the voltage difference ΔV when both voltage regulators are on ($\Delta V = V_{MAIN} - V_{BACKUP}$). | 42 |
| 3.8 | Variation of the current sank by the backup voltage regulator (i_S) circuit with the output voltage level (V_{OUT}) when the backup voltage regulator is off (output in high impedance). | 42 |
| 3.9 | Paparazzi-UAV Ground Control Station (GCS) interface during a flight. | 43 |
| 3.10 | Hardkernel ODROID-C2. | 44 |

| | | |
|------|--|----|
| 3.11 | UAV avionics module fully assembled with all its components. | 45 |
| 3.12 | HobbyKing EPP FPV airframe. | 46 |
| 3.13 | Inside of the HobbyKing EPP FPV fuselage after splitting. Inside cuts are marked and nose was removed. | 47 |
| 3.14 | Side of the fuselage with cuts and some plastic parts glued already (right). | 47 |
| 3.15 | (a) Original EPP FPV fuselage. (b) Modified fuselage (Falcon I design). | 48 |
| 3.16 | (a) Top fuselage module. (b) Assembled wing centre module. (c) Assembly attachment glued to the wings. (d) Wings assembly. | 49 |
| 3.17 | (a) Original EPP FPV tail. (b) Modified tail (Falcon I design). | 50 |
| 3.18 | Internal wiring of the fuselage. | 50 |
| 3.19 | (a) Default foam nose. (b) Custom plastic nose for installing a USB camera board. | 51 |
| 3.20 | Rendering cut of the fuselage with internal components. | 51 |
| 3.21 | 3D model of the Falcon I full assembly. | 52 |
| 3.22 | Falcon I full assembly on the ground (a) and during flight (b). | 52 |
| 4.1 | USB camera module ELP-USB500W02M from ELP Ailipu Technology Co. | 54 |
| 4.2 | MTF plot for lens 5 (6mm focal length). | 58 |
| 4.3 | Simple block diagrams of a single camera (a), and the 3-band multispectral imaging system (b). | 59 |
| 4.4 | Quantum Efficiency of the Aptina / ON Semiconductor AR0130CS image sensor. | 61 |
| 4.5 | Spectral response or transmissivity of the green, red, and NIR band-pass filters chosen for the system. | 62 |
| 4.6 | Comparison of chosen bands with bands used in other commercial multispectral cameras. | 62 |
| 4.7 | From left to right; green, red, and NIR filters mounted on lens cap adapters. | 63 |
| 4.8 | Back of a lens with IR cut filter (left), and after IR cut filter removal (right). | 63 |
| 4.9 | Diagram of the Gstreamer pipeline application for three ELP-USB130W01MT-B/W cameras. | 64 |
| 4.10 | 3D model of custom plane nose with 3 cameras. (a) Isometric view. (b) Side cross-section view. | 65 |
| 4.11 | (a) Custom plane nose with 3 cameras and filters. (b) Nose installed in the plane. | 65 |

| | | |
|------|---|----|
| 4.12 | Map of Bremner Field indicating the delimited area for flight operations. | 66 |
| 4.13 | Correlation plot of alignment algorithm indicating maxima. | 68 |
| 4.14 | Example of pixel offset and cropping of images for alignment. | 69 |
| 4.15 | Superposition of red, green, and NIR band images before and after alignment. . . . | 69 |
| 4.16 | Result of image alignment algorithm. (a) Superposition before alignment. (b) Superposition after alignment. | 70 |
| 4.17 | Example NDVI test of leaves with different levels of stress. (a) RGB image. (b) False colored NDVI image. | 71 |
| 4.18 | Sample pictures of a flights at Bremner Field showing the NIR and Red band images and the NDVI resulting image. | 72 |
| 5.1 | DMM 42BUC03-ML camera module from The Imaging Source, including S-Mount lens holder and lens. | 74 |
| 5.2 | Quantum efficiency of the ON Semiconductor AR0134CS image sensor. | 75 |
| 5.3 | Timing diagram of the trigger, exposure, and image readout processes. | 75 |
| 5.4 | Camera board with S-Mount (M12) lens and optical filter installed using the 3D printed adapter. | 77 |
| 5.5 | Diagram of the basic connections between the camera array and the bridge board. The bridge board routes all USB communications into selectable upstream ports and sends trigger signals to the cameras. | 77 |
| 5.6 | Altium Designer layout view of the bridge board with top layer (red), bottom layer (blue), and silkscreen (yellow). | 78 |
| 5.7 | CAD 3D model of the bridge board. | 78 |
| 5.8 | Diagram of the configurable USB HUB network. SW 1, SW 2, and SW 3 are 2-to-1 bidirectional USB 2.0 switches with inputs controlled by user selectable jumpers. USB 1, USB 2, USB 3, are the isolated upstream ports, and USB M is the master upstream USB port. | 79 |
| 5.9 | Diagram of the trigger system based on a microcontroller unit (MCU). Trigger signals are generated via GPIOs. A UART connection via USB is provided for interactively interfacing with the MCU via serial commands. | 80 |
| 5.10 | Multispectral imaging system hardware with 12 cameras installed. | 84 |
| 5.11 | Example of a sample gray scale image (left) after applying the positive Laplacian operator (right). | 87 |

| | | |
|------|---|----|
| 5.12 | Graph of the focus measure calculated using the above algorithm as the focus is adjusted from out of focus (too far) to out of focus (too close), passing through the in-focus point. Any point outside the in-focus point is out of focus. The graph highlights two random out of focus points for reference, one too far and one too close. | 88 |
| 5.13 | Sample images of the three highlighted points in the graph of Figure 5.12 . (a) Out of focus (too far). (b) In-focus. (c) Out of focus (too close). | 88 |
| 5.14 | Result of aligning two images. (a) Template or reference image. (b) Test image aligned to template image. It is possible to see the black borders filling the empty spaces after alignment. | 90 |
| 5.15 | Result of image alignment algorithm. (a) Superposition before alignment. (b) Superposition after alignment. | 90 |

List of Abbreviations

| | |
|-------|--|
| AGL | Above Ground Level |
| BEC | Battery Eliminator Circuit |
| CCD | Charge-Coupled Devices |
| CMOS | Complementary Metal–Oxide–Semiconductor |
| CPI | Camera Parallel Interface |
| CSI | Camera Serial Interface |
| DOF | Degrees of Freedom |
| DOF | Depth of Field |
| DOM | Degrees of Measurement |
| DSC | Digital Still Camera |
| EPP | Expanded Polypropylene |
| ESC | Electronic Speed Controller |
| FOV | Field of View |
| FPS | Frames Per Second |
| GNDVI | Green Normalized Difference Vegetation Index |
| GPS | Global Positioning System |
| GSD | Ground Sampling Distance |
| GUI | Graphical User Interface |
| IMU | Inertial Measurement Unit |

| | |
|-------|---|
| MCU | Microcontroller Unit |
| MTF | Modulation Transfer Function |
| NDRE | Normalized Difference Red Edge Index |
| NDVI | Normalized Difference Vegetation Index |
| NIR | Near Infrared |
| PCB | Printed Circuit Board |
| PLA | Polylactic Acid |
| PMAG | Primary Magnification |
| ROI | Region of Interest |
| SBC | Single Board Computer |
| SFR | Spatial Frequency Response |
| SNR | Signal-to-Noise Ratio |
| UAARG | University of Alberta Aerial Robotics Group |
| UAV | Unmanned Aerial Vehicle |
| USB | Universal Serial Bus |
| UVC | USB Video Class |
| V4L2 | Video for Linux Two |
| WD | Working Distance |

Chapter 1

Introduction

Aerial and satellite photography are remote sensing techniques that have contributed to numerous developments due to the extensive coverage and large amount of data that can be collected in a short period of time. Remote sensing is based on collecting data about an object or phenomenon from a distance, without making physical contact with the object. Multispectral imaging is a major remote sensing method in the field of spectroscopy that studies the amount of light that is emitted by or reflected from materials and its energy fluctuations with wavelengths. In the context of aerial and satellite multispectral imaging, data is collected by detecting the energy that is reflected from the Earth's surface. Multispectral imaging focuses on a small number of carefully selected bands, usually 3 to 10 bands, that are not necessarily adjacent and tend to be 30-40 nm wide. These bands are usually selected for a specific application by knowing the type of materials that will be studied and their spectral response. Aerial and satellite multispectral imaging has a wide range of applications, that go from research to commercial and industrial.

The Landsat Thematic Mapper (TM) [1] is a satellite mounted whisk broom multispectral scanning sensor from NASA, that has been used for extensive characterization and identification in multiple applications [2, 3, 4, 5]. The TM has a total of 7 spectral bands, 3 in the visible spectrum and 4 in the infrared spectrum. Each band has been carefully selected for the reflectance properties of certain materials of interest, such as vegetation, soil, and water. Manned aircrafts are also used for flying multispectral imaging equipment [6, 7]. While imaging payloads in satellites and manned aircrafts have been useful and effective, the costs and complexity associated with these implementations make them unfeasible for small scale and low cost applications. With the increasing use of Unmanned Aerial Vehicles (UAV) in recent years, and the advances and miniaturization in imaging systems technologies, costs and complexity have been considerably reduced.

UAVs have been successfully used for flying multispectral cameras for a variety of applications. Experiments have shown that UAV-based spectral data has a high correlation with equivalent ground

level measurements. Nebiker et al. [8] validated the use of a UAV mounted high-end multispectral sensor, showing high correlation with respect to ground level reference measurements, together with a low-cost commercial near-infrared (NIR) camera that showed reasonable performance.

A major application of UAV-based multispectral cameras is crop inspection and precision agriculture. Part of Nebiker et al. [8] experiments included plant vitality assessment and plant disease detection. Roosjen et al. [9] used a UAV mounted spectrometer to gather spectral anisotropy data from several agricultural crops as a way to measure crop growth. Candiago et al. [10] also proved the use of UAV-based multispectral imaging for vegetation mapping and crop assessment.

Multispectral images taken from UAVs have also been successfully used for surface and terrain studies, detecting soil and vegetation marks, and surface modeling. Themistocleous et al. [11] combined UAV and ground spectral data to study the formation of crop and soil marks for archaeological applications, while Turner et al. [12] used a multispectral camera together with a visible camera and a thermal infrared camera to study the physiological state of Antarctic moss ecosystems. Multispectral tests from a UAV were reported by Hassan-Esfahani et al. [13] in successful estimation of surface soil moisture over a large field irrigated by a center pivot sprinkler system.

UAV-based multispectral imaging is a growing field that continues to have a major impact in vegetation assessment, crop inspection, and precision agriculture. With recent advances in multispectral sensing technologies, small and lightweight commercial solutions have found their way into the market of UAV remote sensing tools. Nonetheless, these tools are still a relatively expensive solution that, in some cases, lacks certain flexibility for further development. Popular multispectral cameras that are UAV compatible like the Sentek Systems GEMS Multispectral Sensor [14], the Sentera QUAD [15], and the Parrot Sequoia [16] offer a small, lightweight, and highly integrated solution. Conversely, fixed optical and functioning properties affect negatively the flexibility and potential of these solutions.

This work aims to introduce the design and development, as well as demonstrate the use and performance of two main systems. First, a comprehensive UAV system board with redundant power supply that integrates most UAV functions and components. Second, a custom made multispectral imaging system based on USB camera modules. The imaging system is a flexible hardware and software platform that can be used to develop custom UAV compatible multispectral imaging solutions.

1.1 Objective of the Thesis

This thesis attempts to demonstrate the feasibility of a small scale, lightweight, low cost UAV platform for multispectral imaging applications. The work presented here contributes a practical design and implementation methodology for developing UAV systems, focused on an integrated UAV system board and a multi-camera imaging systems for aerial remote sensing. At first, a basic conceptual

3-band multispectral imaging system is developed. The presented system introduces the use of multiple USB 2.0 camera modules and different optical filters for capturing simultaneous images in different spectral bands. Commercial solutions of UAV compatible multispectral cameras are analyzed and compared to the proposed system. To test and validate the system a fixed-wing UAV was designed and built, based on a semi-custom airframe, UAV system board hardware with a novel redundant power supply system, and a single board computer (SBC) for payload. The UAV is used to evaluate the effectiveness and performance of the system in real field multispectral imaging applications. A second and more complex revision of the multispectral imaging system is developed with a higher number of cameras and more advanced features. This second evolution serves as a development platform for UAV compatible multispectral imaging applications.

1.2 Organization of the Thesis

Following this introduction is a literature review in Chapter 2, where a basic overview of imaging systems, remote sensing, and UAV-based multispectral applications is presented, together with previous work pertaining to this thesis. Chapter 3 covers the development of the UAV platform, from the avionics to the airframe, including the development of a UAV system board with redundant power supply. Chapters 4 and 5 elaborate on the design, development, and testing of the basic 3-band multispectral imaging system and the more advanced 12-band multispectral imaging system respectively. Finally, Chapter 6 summarizes the conclusions of this work for future development and application.

Chapter 2

Literature Review

This chapter presents a review of literature previously published relevant to the major topics covered in this work including: imaging systems, image sensors, USB camera modules, spectral imaging, remote sensing, and the integration of unmanned aerial vehicles (UAVs) into aerial imaging remote sensing solutions with applications in multiple areas. Previous system solutions and their achievements and limitations are discussed.

2.1 Imaging Systems and Cameras

An imaging system is an arrangement or setup of component that allow capturing images and handling them. Part of an imaging system can be to optically modify the capture, alter, store, process, and/or transmit the images. The most essential stage of any imaging system is the capturing device, which is the camera. Cameras are optical devices that capture images, either as individual still photographs or as a sequence of images constituting videos. Technically speaking, cameras are remote sensing instruments as they sense subjects without any contact.

A camera consists of a combination of optical, mechanical, and in the case of digital cameras, electronic components. Traditional cameras worked based on capturing light onto a photographic plate or photographic film. Digital cameras use an electronic image sensor to capture images, and additional electronics to transfer those images to some storage media. The present work is focused on the use of digital cameras.

2.1.1 Fundamentals of Optics and Imaging Systems

The design and understanding of an imaging system involves a lot of optical properties, dimensions and calculations, but there are some basic fundamental parameters and concepts (Figure 2.1) that

must be understood prior to any further study.

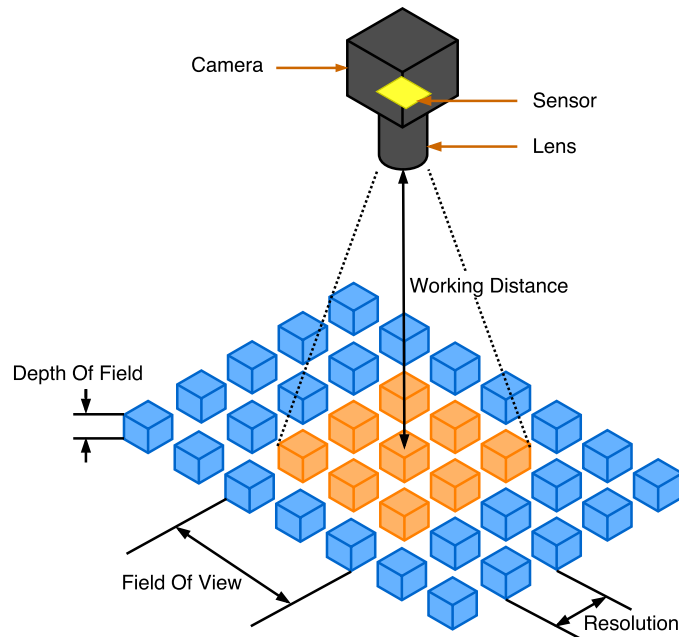


Figure 2.1: Illustration of the fundamental parameters of an imaging system.

The two main components of any camera are the image sensor and the lens. All calculations related to optics are based on the dimensions and characteristics of these two elements. The thin-lens model [17] is used here for the purpose of covering basic optics and imaging concepts. The thin-lens model simplifies ray tracing calculations by ignoring the optical effects due to the thickness of the lens. While it is an approximation, this model (Figure 2.1) illustrates lens and optics principles and introduces the fundamental terms with which to discuss imaging systems.

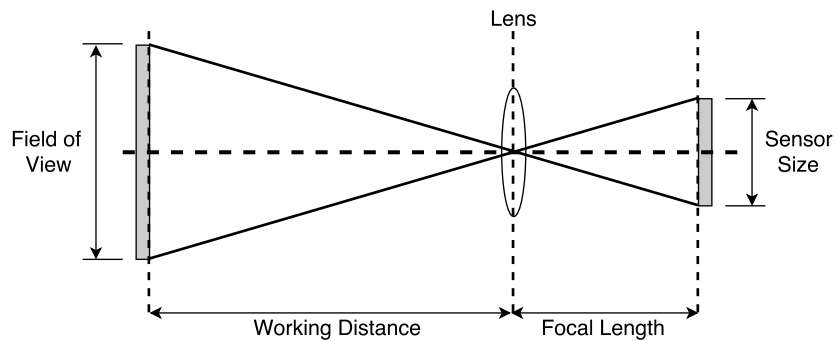


Figure 2.2: Geometry of a basic optics system using the thin-lens model.

Sensor Size The dimensions of the camera sensor's active area. This parameter is typically specified as horizontal and vertical physical dimensions. The sensor size can be calculated by knowing number of horizontal and vertical pixels in the sensor and the size of a pixel. Sensor size is an important parameter in determining the characteristics of a lens for a desired field of view.

Focal Length (f) The distance from the lens's optical center to the image sensor plane when the lens is focused at infinity (Figure 2.2). Focal Length, usually stated in millimeters, is the principal metric of a lens, and gives a measure of how strongly light converges in the optics system, assuming a positive (convex) lens.

Aperture The size of the opening through which light enters the camera. Together with focal length, it defines the cone angle of light that come to a focus in the sensor plane.

Working Distance (WD) The distance from the front of the lens to the object. For a fixed Focal Length, changing the Working Distance proportionally changes the Field of View.

Field of View (FOV) The total viewable area of the object that is imaged by the lens onto the image sensor. This is the portion of a given scene that is captured by the camera's sensor. It can be expressed in terms of total area or by its horizontal, vertical, or diagonal components. FOV is sometimes expressed as the angular size of the view cone, and it is called angle of view. The angle of view can also be measured horizontally, vertically, or diagonally (Figure 2.3).

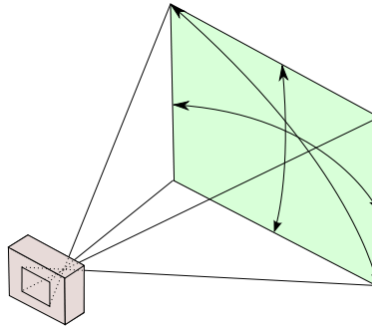


Figure 2.3: Angle of view and its horizontal, vertical and diagonal components [18].

The horizontal and vertical components of the angle of view can be calculated in degrees by:

$$\theta_{H,V} = 2 \arctan \left(\frac{s_{H,V}}{2f} \right) \frac{180}{\pi} \quad (2.1)$$

where $s_{H,V}$ is the horizontal or vertical size of the sensor and f is the Focal Length. Similarly, the relationship between Focal Length, Sensor Size, Working Distance, and Field of View is defined by:

$$FOV_{H,V} = \frac{s_{H,V}WD}{f} \quad (2.2)$$

It can be seen from (2.2) that a greater Focal Length leads to a smaller Field of View as the angle becomes smaller. Figure 2.4 illustrates examples of different Focal Lengths, and how the angle of view and Field of View change accordingly.

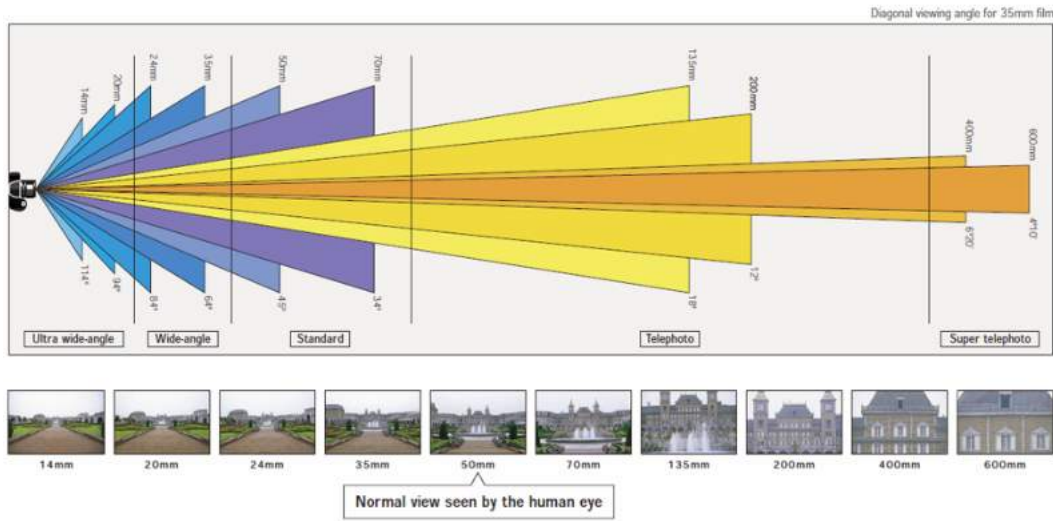


Figure 2.4: Focal length and angle of view of a “full frame” (35mm) image sensor [19].

Resolution The smallest feature size of the object that can be visibly resolved in the image. Resolution quantifies how close lines can be to each other and still be distinguished in the final image. This is a simplified definition for a concept that is very important and widely misunderstood. A broader and more detailed explanation of resolution will be covered later on. Concepts like sensor resolution, Modulation Transfer Function (MTF), and effective resolution of an imaging system will be introduced.

Depth of Field (DOF) The range between the maximum and minimum working distances where it is possible to maintain acceptable focus. Depth of Field is also the total amount of object movement in the optical axis allowable while maintaining focus.

Primary Magnification (PMAG) The Primary Magnification is defined as the ratio between the Sensor Size and the Field of View:

$$PMAG = \frac{S_{H,V}}{FOV_{H,V}} \quad (2.3)$$

2.1.2 Image Sensor

As previously mentioned, the image sensor is the principal element of a camera, in charge of capturing light and transferring the information that constitutes an image. Image sensors have a sensitive cell array that converts light waves into electrical signals that are measured and interpreted in order to produce a matrix of values that form the image.

2.1.2.1 CCD vs. CMOS Technologies

Most modern image sensors use one of two types of technologies: semiconductor charge-coupled devices (CCD) or active pixel sensors in complementary metal–oxide–semiconductor (CMOS).

Regardless of the technology used, image sensors must first convert light into electrons that are accumulated as charge, and then read the value of each cell. In CCD sensors, the charge is transferred from one pixel to another across the chip until it ends up at the periphery of the array, where it is converted into voltage. Then, an analog-to-digital (ADC) converter turns each pixel's voltage into a digital value. In CMOS image sensors, there are several transistors integrated into each pixel that amplify and transfer the charge using traditional wires. CMOS sensors are more flexible because pixels can be read individually. Figure 2.5 shows a visual comparison of the working principle between CCD and CMOS sensors.

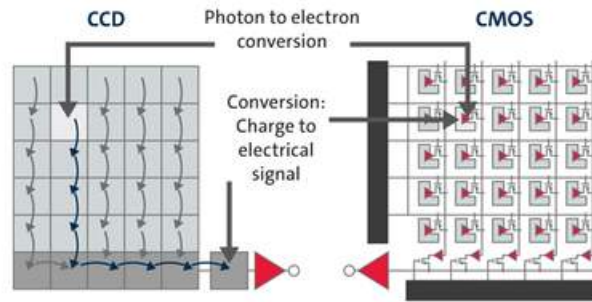


Figure 2.5: Conversion and charge transferring principles between CCD and CMOS technologies [20].

There is a number of features where CCD and CMOS image sensor are very different. CCD sensors create a higher-quality, low-noise image, whereas CMOS sensors are more susceptible to noise. Due to each pixel on a CMOS sensor having several transistors next to it, many of the photons will inevitably hit these transistors and the overall light sensitivity will be lower. CCD sensors use a special manufacturing process that guarantees the transportation of charge across the chip

without distortion, leading to sensors with high fidelity. The downside is that this process consumes considerably more power. CCD sensors can consume up to 100 times more power than an equivalent CMOS sensor. Contrarily, CMOS chips use traditional manufacturing processes, so they can be fabricated on just about any standard silicon production line. Therefore, CMOS sensors tend to be inexpensive compared to CCD sensors. Table 2.1 summarizes the comparison of some of the most important features between CCD and CMOS image sensors.

Table 2.1: Features comparison between CCD and CMOS image sensors.

| Feature | CCD | CMOS |
|-------------------|------------|-----------------|
| System Noise | Low | Moderate |
| Responsivity | Moderate | Slightly Better |
| Power Consumption | High | Low |
| Sensitivity (*) | High | Moderate |
| Resolution | High | High |
| Cost | High | Low |

(*) Visible and infrared bands up to approximately 1100 nm.

2.1.2.2 Rolling vs. Global Shutter

The shutter is the mechanism for exposing the sensor to light. There are two types of shutter, rolling and global, where the difference is how each controls the scanning of the image. In a rolling shutter mechanism, the image is scanned sequentially, where the pixels of the sensor are exposed to light line by line. It usually starts from top to bottom and is more commonly found in CMOS sensors. While each pixel line collects light during the same period of time, the light collection start and end times for each line differ.

In a global shutter mechanism, on the other hand, all the pixels are exposed at the exact same time and during the same time. Since light collection happens simultaneously for all pixels, the scene is “frozen” in time, provided that the time window for light collection is short enough and that no motion occurs during this window. If this is the case, there will be no motion blur in the resulting image. Motion blur is likely to be present in images captured with a rolling shutter if there is any movement occurring between the start of the first line and the end of the last line. Figure 2.6 shows a comparison of a moving object being captured by a rolling shutter sensor and a global shutter sensor.

2.1.2.3 Performance Metrics of Image Sensors

Essentially, the function of an image sensor is the conversion of light to a digital image. There are some common metrics used for comparing how well image sensors can perform their task. This

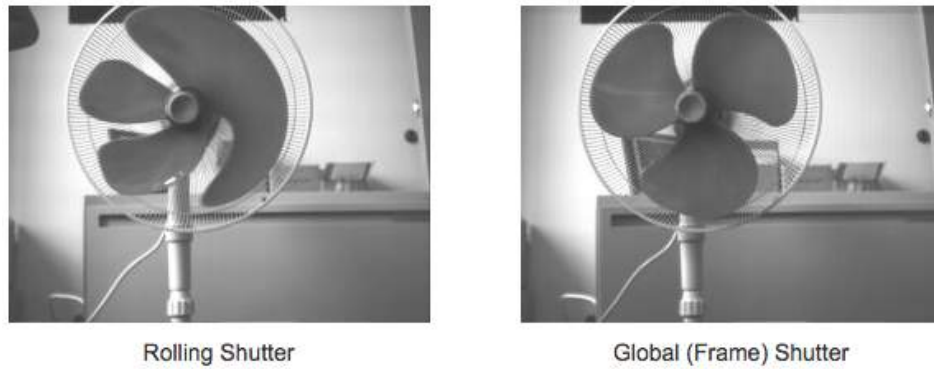


Figure 2.6: Comparison between rolling shutter and global shutter captures on moving target [21].

section elaborates on some of these metrics and presents them in three categories: metrics related to the pixel layout, metrics related to the pixel physics, and metrics related to the pixel readout [22].

Metrics Related to Pixel Layout The most common metric used for comparing image sensors is the **pixel count**, usually expressed in megapixels. The number of pixels in a sensor depends on the overall size of the chip and the area the designer has available for the pixels versus the area used for the rest of the circuitry. When it comes to pixel count, the higher the better.

Another metric that also relates to pixel count is the **pixel pitch**, usually expressed in micrometers. This metric defines how much area each pixel occupies in the array. Generally, a smaller pitch means more pixels can be fitted. However, smaller pixels will not collect as much light, and thus might not be suitable for fast exposure captures or low illumination applications.

Finally, one more highly used metric is the **fill factor**, which deals with how pixels are physically laid out. The fill factor is the percentage of the pixel area that is occupied by the actual photodiode. A 100% fill factor would be ideal as all the pixel area would be used for light collection. Most sensors don't have a 100% fill factor, and designers need to decide how much area is used for photodiodes. Nonetheless, some chips can achieve 100% fill factor by using a backside illuminated design, where readout circuitry is placed below the photodiode, allowing it to occupy all the pixel area [23, 24].

Metrics Related to Pixel Physics Another set of metrics by which image sensors are compared is related to the physics of how photons are converted into charges. When photons hit the silicon with enough energy an electron-hole pair is formed. But this does not happen for every single photon and the effect also differs depending on the wavelength. **Quantum efficiency** is a percentage measure of how many photons are converted into electron-hole pairs.

Another important metric is the **dynamic range**, given in decibels, which measures how accurate a sensor can capture a signal under low light conditions all the way up until full capacity. A higher

dynamic range is desired as it will allow the sensor to operate in a wider range of light conditions.

Metrics Related to Pixel Readout A third set of metrics that is useful for image sensor comparison has to do with the features and performance of the readout process and circuitry. One of the most important metrics here is the **Signal-to-Noise** (SNR) ratio, measured in decibels. This is a ratio of how much of the original signal is captured and present in the output, versus how much noise is present. The higher the SNR means there is more of the original signal present in the output compared to the noise level. SNR varies with light intensity, as it is typically lower for dim light and higher for bright light.

Other important metrics are the **percentage of linearity**, which is how linear the pixel output is with respect to the captured photovoltage, and the **frame rate**, which is a measure of how many times per second the full pixel array can be exposed and read. **Power consumption** is also important. The choice of power supply, operating frequency and capacitance affect power consumption. Typically, a higher frequency allows a higher frame rate at the cost of higher power consumption.

Finally, the output **bit-depth** is another important feature. The photodiode signal that is later converted into voltage and read, will eventually be sampled by an analog-to-digital converter to output a digital value. The bit-depth defines the number of bits used for representing this number. The higher the number of bit, the higher the value resolution and the more distinct values can be represented.

2.1.3 Lenses

Lenses are optical transmission devices used for focusing or dispersing light by means of refraction. Lenses are made out of transparent glass or plastic, usually with a circular shape. The two sides of the lens are polished surfaces, either or both of which have a concave or convex curve.

A lens can achieve its focusing effect thanks to light changing direction as it passes through the lens, crossing the interfaces between air and the lens material. This effect is called refraction, and it occurs both where light enters the lens and where it emerges from the lens into the air.

Lenses are important because they have the valuable property of forming images of objects situated in front of it, and are an indispensable component of any camera or imaging system. Lenses also have drawbacks such as non-linear distortion (which can be measured and corrected with image processing) and limits to optical resolution.

2.1.4 Modulation Transfer Function

The Modulation Transfer Function (MTF) is an important and common metric for evaluating the performance of imaging systems. MTF measures the ability of the imaging system to transfer con-

trast at a particular resolution from the object to the image. In order to understand the importance and significance of the MTF, the concepts of resolution and contrast must be defined.

2.1.4.1 Resolution

A simplified definition of resolution was given in a previous subsection. A more detailed and thorough explanation of this concept is presented here. Resolution is a measurement of how well an imaging system can reproduce object detail. It is often expressed in line-pairs per millimeter (lp/mm), which is a unit of frequency that originates from the testing method to measure resolution. A line-pair is a sequence of two lines with opposing contrast, that is one black and one white. A basic target with a sequence of alternating, equally spaced black and white stripes is usually used for performing MTF testing. This target presents line-pairs with increasing frequency in order to test the imaging system resolving capabilities. When an imaging system captures this pattern, with perfectly clear edges, lines will have a degree of blurriness in the final image due to imaging system limitations (Figure 2.7). Increasing the frequency will also increase the blur. High resolution images have a high level of detail and minimal blur whereas low resolution images lack fine detail and exhibit higher blur.

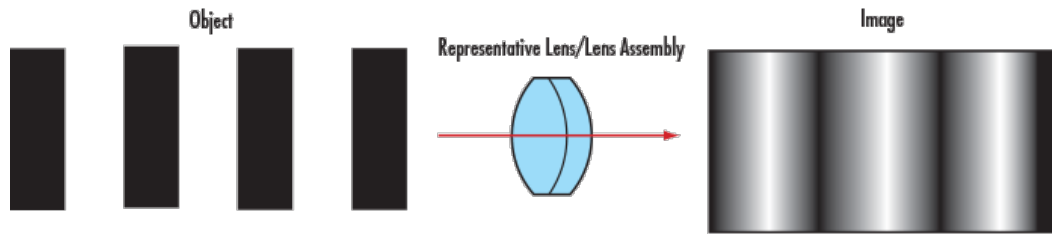


Figure 2.7: Perfectly clear pattern before (left) and after (right) passing through a low resolution lens [25].

As the frequency in the target increases the line-pairs become thinner and less number of pixels are required for imaging each line-pair. If the stripes are imaged onto neighboring pixels, then they will appear to be one single long stripe in the image (Figure 2.8a) rather than two separate stripes (Figure 2.8b). Therefore, there is a minimum line-pair width for which the image sensor is capable of resolving the black and white stripes. At least the distance equivalent to one pixel must be between two black stripes. Following this reasoning, a minimum of 2 pixels is required for imaging a line-pair, one pixel for the black stripe and one for the white stripe.

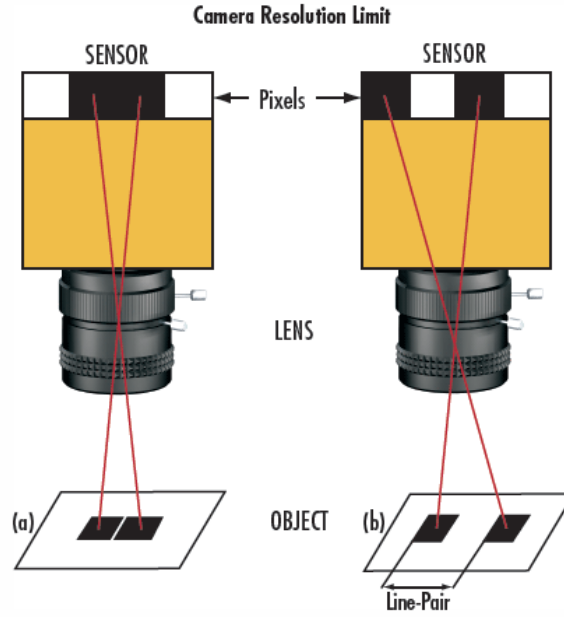


Figure 2.8: Resolving two black stripes. If the space between the stripes is too small (a) the camera sensor will not be able to resolve them as separate stripes [25].

Correspondingly, this limitation is defined by the size of the pixel in the image sensor. The sensor resolution can be calculated with (2.4).

$$\text{Sensor Resolution (lp/mm)} = \frac{1000}{2(\text{pixel size (um)})} \quad (2.4)$$

This is also known as the Nyquist limit. It can be seen that as pixel sizes get smaller the corresponding sensor resolution or Nyquist limit in lp/mm increases proportionally. Additionally, the object resolution is calculated using the sensor resolution and the primary magnification (PMAG) of the lens (equation 2.5). It is important to note that the equation for object resolution assumes the lens has no resolution loss. Object resolution can also be converted to μm using (2.6).

$$\text{Object Resolution (lp/mm)} = \text{PMAG} \times \text{Sensor Resolution (lp/mm)} \quad (2.5)$$

$$\text{Object Resolution (um)} = \frac{1000}{2(\text{Object Resolution (lp/mm)})} \quad (2.6)$$

2.1.4.2 Contrast

Contrast can be understood as the relation between low and high luminance in a scene or image. In a black and white bar stripe test target, minimum luminance will be black and maximum luminance will be white. Any value between these two limits will be a mix of black and white (gray) luminance values. A sample plot (Figure 2.9) of these value will produce a square wave with different amplitudes according to the luminance value.

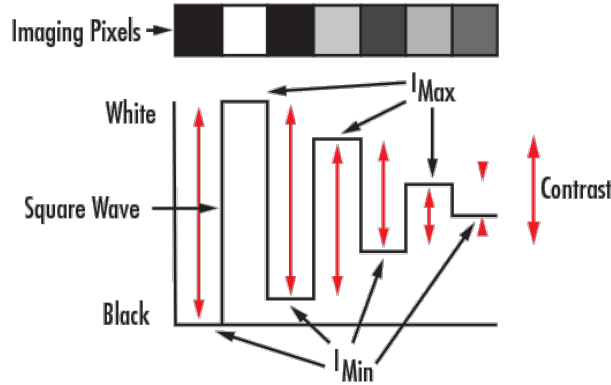


Figure 2.9: Different levels of contrast plotted as a square wave [25].

There are different way to calculate and measure contrast depending on the target used for testing. In this particular case the Michelson Contrast [26] is used. The Michelson Contrast, also known as visibility, peak-to-peak contrast, or modulation, measures the relation of luminance in periodic patterns where both bright and dark features are equivalent and take up similar fractions of the total area (e.g. sinusoidal gratings). The Michelson Contrast is defined as:

$$Contrast = \frac{I_{max} - I_{min}}{I_{max} + I_{min}} \quad (2.7)$$

where I_{max} and I_{min} are the maximum and minimum luminance values respectively. The denominator is the luminance difference while the denominator is twice the luminance average.

Considering the effect of a lens and the differences between the resulting image and the real object, as shown in Figure 2.7, the contrast plot of the resulting image will look more like a sinusoidal wave due to black and white transitions in the target not being resolved perfectly (Figure 2.10a). Moreover, as the line-pair frequency is increased, the contrast will decrease, which is seen in the amplitude of the resulting sinusoidal wave (Figure 2.10b). This effect is always present due to the limitations of the imaging lens. For the image to appear defined, black and white must be well defined with a minimal amount of grayscale in the transition.

With the concepts of resolution and contrast properly introduced, the MTF can be seen as the way to integrate these two metrics into a single specification. As the frequency of line pairs increases on the test target, it becomes more difficult for a lens to effectively transfer the corresponding decrease in contrast. In other words, the MTF describes the attenuation in contrast as a function of the spatial frequency. Figure 2.10c shows a the general shape of a MTF plot, where the modulation or contrast, expressed as a percentage, decreases as the spatial frequency (in lp/mm) increases.

Spatial Frequency Units This section briefly covers the different units that used for expressing spatial frequency. There is a total of six units commonly used:

- LW/PH = Line width per picture height
- LP/mm = Line pairs per millimeter
- L/mm = Lines per millimeter
- Cycles/mm = Cycles per millimeter
- Cycles/pixel = Cycles per pixel
- LP/PH = Line pairs per picture height

Table 2.2 show the conversion operations for spatial frequency units. To convert from left column units to top row units use the operation in the corresponding row/column intersection.

Table 2.2: Spatial frequency unit conversion chart.

| | LW/PH | LP/mm | L/mm | Cycles/mm | Cycles/pixel | LP/PH |
|--------------|-----------------------|------------------|------------------|------------------|------------------|------------------|
| LW/PH | $\times 1$ | $/ [2 \times h]$ | $/ h$ | $/ [2 \times h]$ | $/ [2 \times v]$ | $/ 2$ |
| LP/mm | $\times [2 \times h]$ | $\times 1$ | $\times 2$ | $\times 1$ | $\times p$ | $\times h$ |
| L/mm | $\times h$ | $\times 0.5$ | $\times 1$ | $\times 0.5$ | $\times [p / 2]$ | $\times [h / 2]$ |
| Cycles/mm | $\times [2 \times h]$ | $\times 1$ | $\times 2$ | $\times 1$ | $\times p$ | $\times h$ |
| Cycles/pixel | $\times [2 \times v]$ | $/ p$ | $\times [2 / p]$ | $/ p$ | $\times 1$ | $\times v$ |
| LP/PH | $\times 2$ | $/ h$ | $\times [2 / h]$ | $/ h$ | $/ v$ | $\times 1$ |

Where p is pixel pitch, h is picture height, and v is number of vertical pixels.

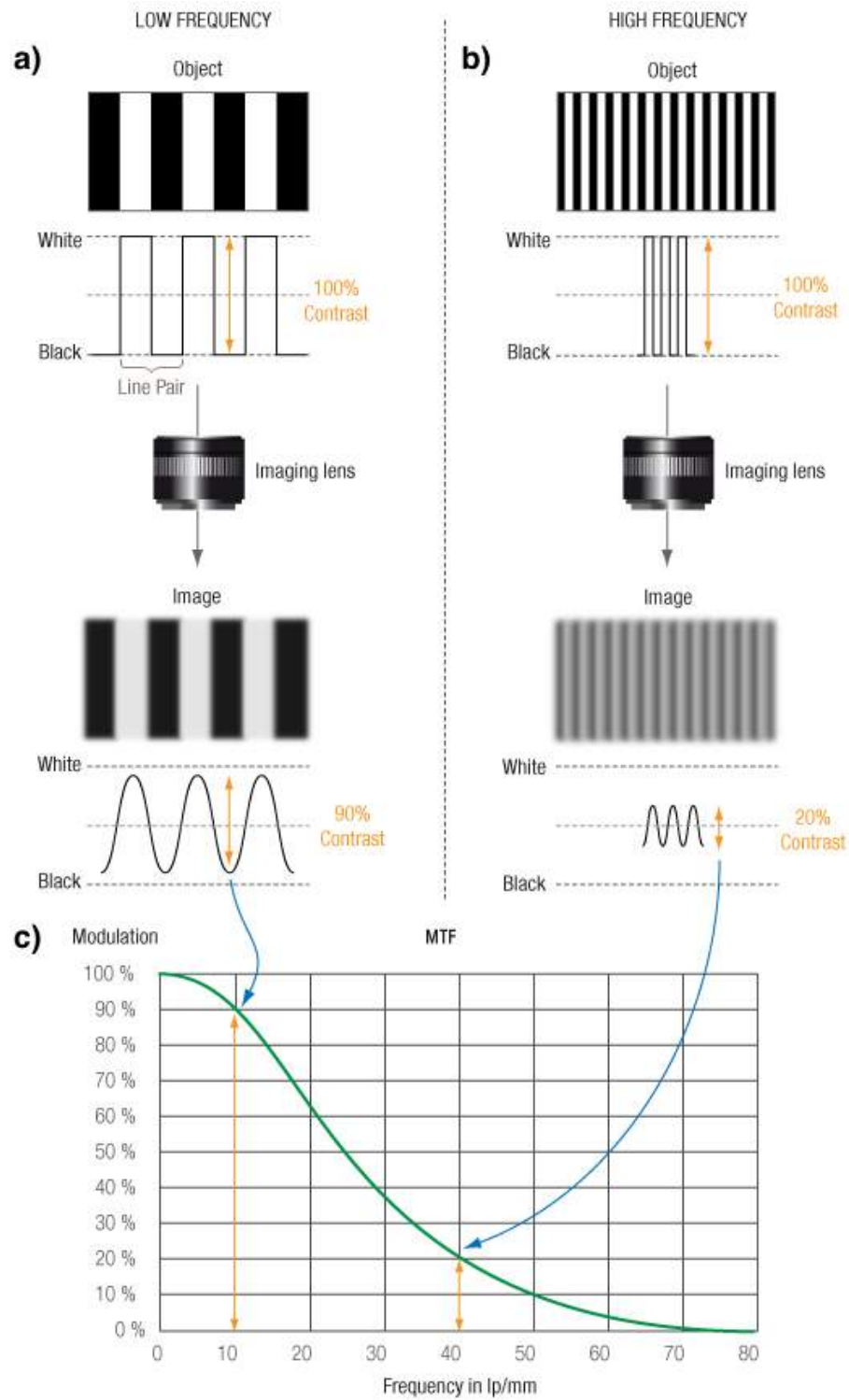


Figure 2.10: Contrast comparison in resulting images at low (a) and high (b) frequency, and MTF plot (c) [27].

2.1.4.3 Slanted-Edge MTF Measurement

The ISO 12233 standard (Photography -- Electronic still picture imaging -- Resolution and spatial frequency responses) [28] defines a method for measuring the Modulation Transfer Function (MTF), also known as Spatial Frequency Response (SFR), based on a slanted-edge target. The slanted-edge MTF method was developed by Burns in [29] as a modified version of traditional edge-gradient analysis methods that used scanning microdensitometers for digital image characterization [30]. Burn's method allows to use actual image data taken from the device, and consists of a slanted, or skewed edge target (Figure 2.11), in conjunction with data processing algorithms. This method reduces aliasing and is particularly useful for digital still cameras (DSC). This method has been widely and successfully applied to MTF measurements of not only digital still cameras, but also film and print scanners, and CRT displays.

Work done by Williams in [31] showed the evaluation of a software implementation of the ISO procedure and found it to provide a robust, accurate, and precise tool for quantifying MTF from a digital capture device. Williams reported the tool to be largely insensitive to edge angle variations, capable of delivering accurate MTF estimates for peak SNRs as low as 10:1, and capable of handling ill-behaved frequency morphologies caused by FIR sharpening. Refined practices in the use of this method have also been reported to improve performance by reducing and identifying conditions that can cause measurement errors [32].

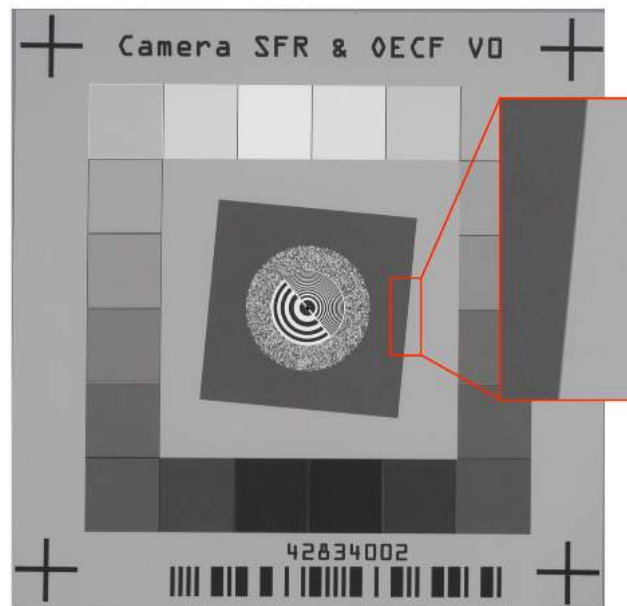


Figure 2.11: SFR target with horizontal and vertical (highlighted) slanted edges.

The slanted-edge MTF method consists of three basic operations: acquiring an edge profile from the (image) data, computing the derivative in the direction of the edge, and computing the discrete Fourier transform of this derivative array (Figure 2.12). The edge profile is also referred to as the region of interest (ROI), and it can have different sizes and orientations (horizontal or vertical edge). The result is a data set that represents the MTF. A typical graph of a balanced MTF can be seen in Figure 2.10c.

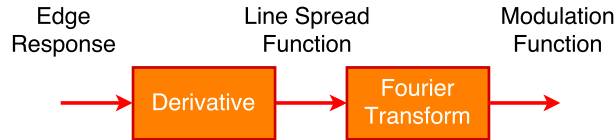


Figure 2.12: Flowchart of the operations in the edge gradient analysis.

A MTF graph can have different shapes (Figure 2.13) that indicate characteristics of the imaging system, environment, and conditions[33]. However, for the purposes of direct performance comparison between cameras and imaging systems, a single value that resumes MTF results has been defined. Burns and Williams in [34] introduced the concept of sampling efficiency, which was later added to the ISO 12233 standard. Sampling efficiency is a measure of limiting resolution, defined as the normalized frequency at which the MTF falls to 10%.

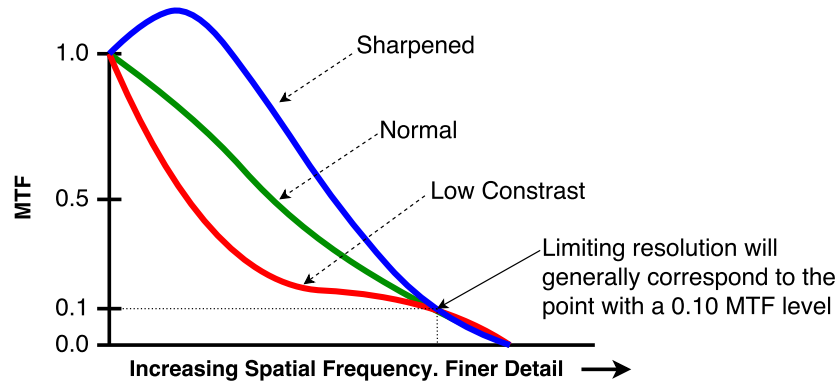


Figure 2.13: Different MTF shapes and their meaning.

The sampling efficiency is used to calculate the resolution efficiency and the effective resolution of an imaging system. The process starts by determining the frequency of the first 10% MTF occurrence for both vertical and horizontal components, clipping at 0.5 cycles/pixel. Each of these values is normalized against the digital limit (Nyquist criteria) of 0.5 cycles/pixel to obtain the sampling efficiency of each direction (equation 2.8).

$$SamplingEfficiency_{H,V}(\%) = \frac{Frequency(0.1MTF)_{H,V} (cycles/pixel)}{0.5 (cycles/pixel)} \quad (2.8)$$

The resolution efficiency is calculated as the product of the horizontal and vertical sampling efficiencies (equation 2.9).

$$ResolutionEfficiency(\%) = SamplingEfficiency_H(\%) \times SamplingEfficiency_V(\%) \quad (2.9)$$

Finally, the effective resolution of the imaging system can be found multiplying the delivered resolution (usually the image sensor resolution) with the resolution efficiency (equation 2.10).

$$EffectiveResolution(Mpx) = ResolutionEfficiency(\%) \times DeliveredResolution(Mpx) \quad (2.10)$$

2.1.5 USB Camera Modules

USB camera board modules are based on an image sensor, a processor that controls and reads the sensor, and an interchangeable lens. The onboard processor has a USB interface to communicate to an external computer using the USB Video Class (UVC) standard driver. These type of cameras can be compared to webcams in terms of components, settings, and interface. Given the relatively small number of components, USB camera board modules can achieve a small form factor, making them a lightweight alternative to higher-end professional cameras.

The segment of board-level cameras that are of interest in this project carry image sensors with a 1/4" - 1/2" optical format and S-Mount (M12) lenses. These lenses are small and available with a wide variety of characteristics (focal length, resolution, etc.). Interchangeable lenses increase the overall flexibility of the camera system.

2.1.5.1 USB Video Class (UVC)

The USB Video Class (UVC) is a standard that groups certain devices into a special class of USB device. UVC encloses devices capable of streaming video like webcams, digital camcorders, transcoders, analog video converters and still-image cameras. The advantage of UVC is that it provides native "universal" and cross-platform drivers to interface with devices without depending on manufacturer specific drivers.

2.1.5.2 Video for Linux Two (V4L2) API

Video for Linux Two (V4L2) API is a kernel interface that includes a collection of device drivers and an API for analog radio and video capture on Linux systems [35]. V4L2 was developed by Bill Dirks as an improved version of its predecessor Video for Linux (V4L). V4L2 provides higher flexibility, a new structure, and the possibility of interfacing with multiple applications/processes/devices at the same time [36].

V4L2 is a high-level driver that interfaces with the lower-level UVC driver, therefore acting as a middle layer between applications and the UVC driver.

2.1.5.3 GStreamer

GStreamer¹ [37] is an open source, cross-platform, pipeline-based multimedia framework capable of linking multiple media processing systems to complete complex workflows. GStreamer provides a lot of flexibility for constructing related series of multimedia elements arranged in parallel flows called pipelines. These pipelines are assembled with automatic negotiation between its elements, making the construction of the workflow easy and robust.

Pipelines in GStreamer consist of a set of connected elements that can be divided in three major groups: data producers (sources), processing steps (e.g. formats, filters, codecs), and data consumers (sinks). The framework is based on plugins that provide codecs and functionalities.

GStreamer is written in the C programming language, but it has written bindings for various languages such as Python, Vala, C++, Perl, GNU Guile, C# and Ruby. It also provides a command line tool option.

¹<https://gstreamer.freedesktop.org/>

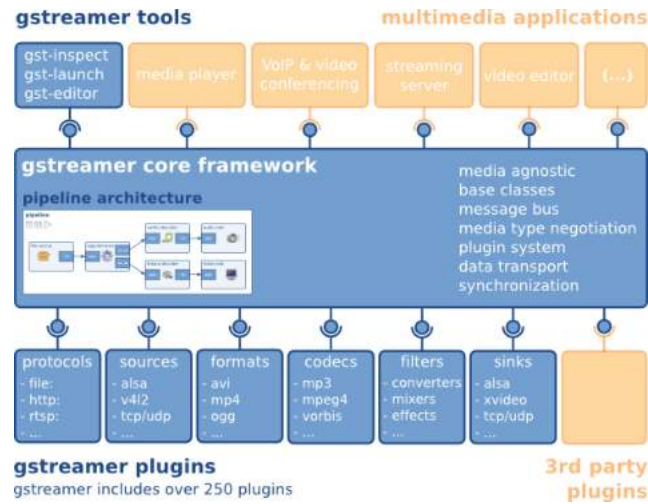


Figure 2.14: Diagram of GStreamer components [38].

2.2 Spectral Imaging

Spectral imaging is a common technique in the field of spectroscopy that studies the level of light that is emitted by or reflected from materials and its energy fluctuations with wavelengths. The measurements obtained using this technique produce simultaneous image data in multiple bands.

Two major distinctions among this technique are hyperspectral imaging and multispectral imaging. The main difference between the two is the number of bands and how narrow the bands are. Hyperspectral imaging consists of hundreds or thousands of narrow (10-20 nm), adjacent spectral bands. This comprehensive image data set make it possible to derive a continuous spectrum of the image cell (Figure 2.15) that can be used to identify materials.

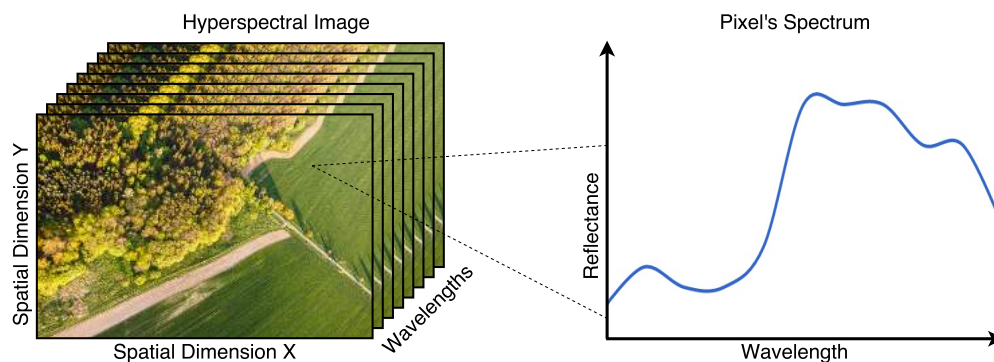


Figure 2.15: Illustration of hyperspectral imaging. Each pixel in the image forms the spectrum trough imaged wavebands.

Conversely, multispectral imaging uses a smaller number of bands, usually 3 to 10 bands, that are not necessarily adjacent and tend to be wider (30-40 nm). These bands are usually selected for a specific application by knowing the type of materials that will be studied and their spectral response.

Figure 2.16 shows a graphical comparison between hyperspectral and multispectral imaging examples.

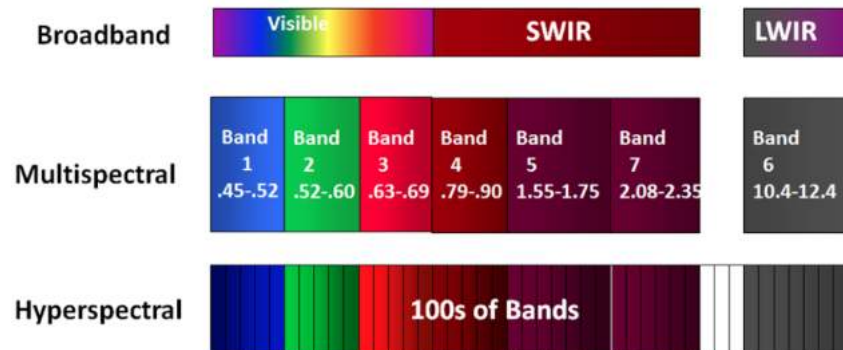


Figure 2.16: Comparison of band classifications in multispectral (few wide bands) and hyperspectral (several narrow bands) models. Units are in micrometers for the multispectral ranges.

2.2.1 Vegetation, Soil and Water Reflectance

Three of the major natural materials of interest when looking at landscapes are vegetation, soil and water. Figure 2.17 shows the reflectance spectrum of each of these materials. It can be seen that the three reflectance curves are fairly close in the visible spectrum (390 - 700 nm). Therefore, differentiation of these materials must be done at longer wavelengths.

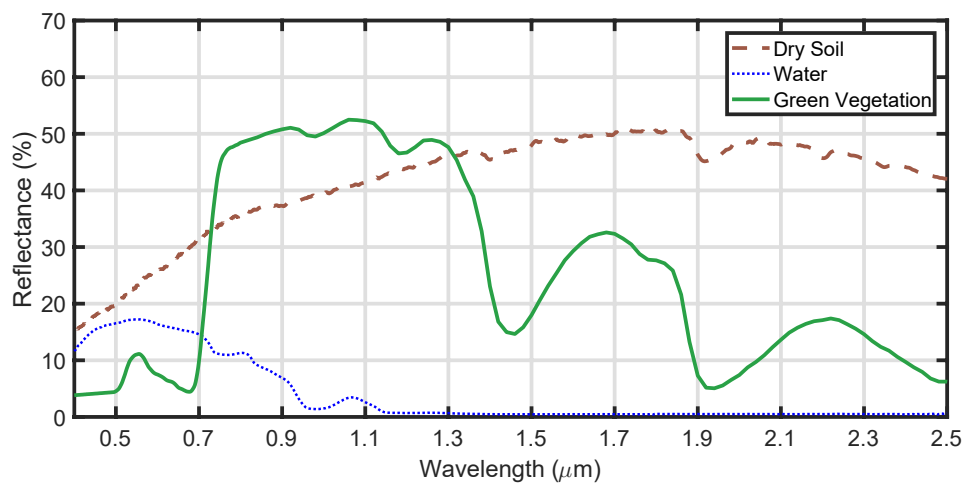


Figure 2.17: Reflectance spectrum of water, soil and vegetation.

Generally, water only reflects light in the visible range of the spectrum, making very distinct from soil and vegetation in the infrared region. The reflection of soil increases from the visible range to the infrared range. There are different types of soil that have slightly different reflectance characteristics depending on its composition and the content of water and minerals. The graph above shows the average curve for bare ground soil. Finally, the spectral reflectance of green vegetation is very characteristic. Visible light is greatly absorbed by plants, specially blue and red light as they are used during photosynthesis. The curve increase abruptly in the red-edge region and then infrared light is greatly reflected.

2.2.2 Landsat Thematic Mapper

The Thematic Mapper (TM) [1] is an advanced, multispectral scanning sensor that is part of the NASA Landsat program. It is designed for higher image resolution, sharper spectral separation, improved geometric fidelity and greater radiometric accuracy and resolution. It features a total of 7 spectral bands, 3 in the visible spectrum and 4 in the infrared spectrum. Band 6 senses thermal (heat) infrared radiation in the 10.41-12.5 μm [2]. Figure 2.18 shows the graph from Figure 2.17 with the addition of the Landsat TM bands up to 2.5 μm (band 6 is not shown in the graph).

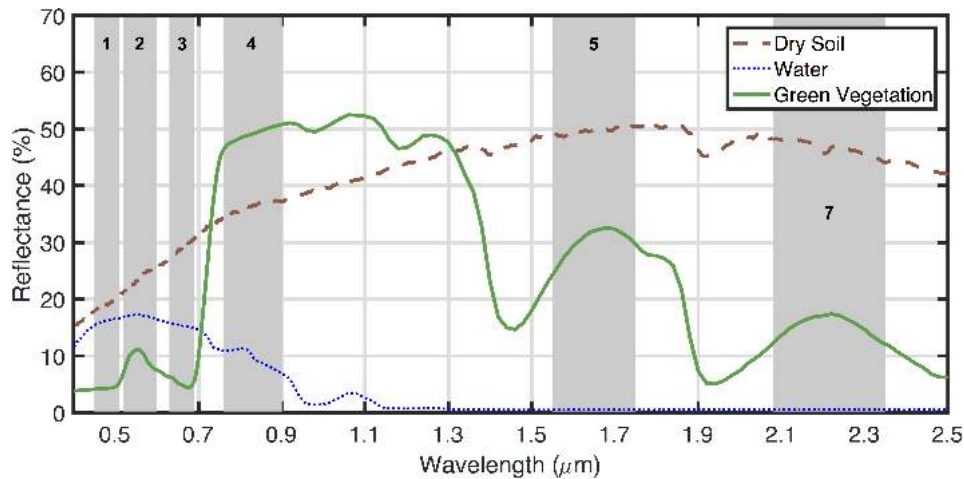


Figure 2.18: Reflectance spectrum of water, soil and vegetation together with the Landsat TM bands in the 0-2.5 μm range.

TM is a whisk broom scanner which takes multi-spectral images across its ground track. Most bands have a 30 m spatial resolution, with the exception of band 6 which has a 120 m spatial resolution. Table 2.3 shows the wavelength ranges and brief description of the Landsat TM bands.

Table 2.3: Landsat Thematic Mapper Bands for Vegetation Monitoring.

| Band | Wavelength Range (nm) | Description |
|------|-----------------------|---|
| TM1 | 450 - 520 | [blue-green] - maximum chlorophyll absorption. Used for monitoring aquatic ecosystems. Noisy, susceptible to scatter. |
| TM2 | 520 - 600 | [green] - green vegetation reflection peak. Slight sensitivity to plant chlorophyll concentration. |
| TM3 | 630 - 690 | [red] - strong chlorophyll absorption. Useful for distinguishing between vegetation and soil and in monitoring vegetation health. |
| TM4 | 760 - 900 | [NIR] - strong water absorption. Bright reflectance for soil and vegetation. Good for defining the water/land interface. |
| TM5 | 1550 - 1750 | [short-IR] - very sensitive to moisture. Used to monitor vegetation and soil moisture. |
| TM7 | 2080 - 2350 | [mid-IR] - This band is also used for vegetation moisture although generally band 5 is preferred for that application. |
| TM6 | 10410 - 12500 | [long-IR] - thermal (heat) infrared radiation. |

2.2.3 Lightweight UAV-Compatible Multispectral Imaging Systems

With the increasing number of applications using multispectral remote sensing a number of multispectral imaging systems have been developed and introduced in the market. This section presents a brief overview of some popular multispectral imaging systems available in the market.

The Tetracam ADC Micro [39] is a single sensor camera with an Aptina CMOS rolling shutter sensor. The camera captures the red, green and near infrared (NIR) bands using a single wide bandpass filter that covers the 520-920 nm range. The camera has fixed optical parameters of 8.43 mm focal length and optical aperture of f/3.2. Tetracam also has the Mini MCA4 [40], which is a camera array system. It features four cameras, 1.2 megapixels each, covering the blue, green, red, and NIR bands. There are versions of this system with 6 and 12 cameras.

The Sentek Systems GEMS Multispectral Sensor [14] is a dual camera system. It features an RGB camera and a NIR camera, both with 1.2 megapixel sensors and a global shutter. Both cameras have a fixed focal length of 7.7 mm. This system can be acquired as an OEM PCB module or as a final product with enclosure.

The Sentera QUAD [15] is a compact multispectral imaging system with four 1.2 megapixel global shutter cameras. It features one RGB camera and three monochromatic single-band cameras covering red, red-edge, and NIR bands. This unit integrates all four sensors into a small package.



Figure 2.19: (a) Tetracam Mini MCA6. (b) Sentek GEMS. (c) Sentera QUAD. (d) Parrot Sequoia.

Finally, the Parrot Sequoia [16] is a very popular and small unit, somewhat similar to the Sentera QUAD. It has four 1.2 megapixels global shutter single-band sensors covering the green, red, red-edge, and NIR, in addition to a 16 megapixels rolling shutter RGB camera.

Table 2.4 presents a detailed comparison of the features of each camera. At this point, it is important to introduce a term that is used to compare the level of detail present in an image. In remote sensing, ground sampling distance (GSD) of the ground from the air or space is the distance between the center of two adjacent pixels measured on the ground. This measure gives a sense of how much distance and area are covered by pixel in the image. This measure is better as the number is lower as it relates to higher resolution. The GSD values presented in the table below correspond to a working distance, or altitude above ground level (AGL), of 400 ft (~122 m).

Table 2.4: Comparison of common multispectral imaging systems.

| Camera | Tetracam ADC Micro | Tetracam Mini- MCA4 | Sentek GEMS | Sentera QUAD | Parrot Sequoia |
|------------------------------|--------------------------|---------------------------|----------------|-----------------|-------------------|
| Dimensions (mm) | 75 x 59 x 33 | 131 x 78 x 87 | 127 x 89 | 76 x 62 x 48 | 59 x 41 x 28 |
| Weight (g) | 90 | 600 | 320 | 170 | 72 |
| Number of Bands | 4 | 4 | 4 | 4 | 4 |
| Focal Length (mm) | 8.43 | 9.6 | 7.7 | 5.0 | 3.98 |
| FOV (H° x V°) | 37.6 x 28.7 | 38.2 x 30.9 | 34.6 x 26.3 | 51.2 x 39.6 | 61.9 x 48.5 |
| Sensor size (mm) | 6.55 x 4.92 | 6.66 x 5.32 | 4.8 x 3.6 | 4.8 x 3.6 | 4.8 x 3.6 |
| Resolution (pixels) | 2048 x 1536 | 1280 x 1024 | 1280 x 960 | 1280 x 960 | 1280 x 960 |
| Pixel size (μm) | 3.12 | 5.2 | 3.75 | 3.75 | 3.75 |
| GSD (cm) @120m | 4.6 | 6.6 | 5.1 | 9.1 | 11.0 |
| Price (USD) | 2,995.00 | 9,995.00 | 3,500.00 | 4,599.00 | 3,500.00 |

Figure 2.20 shows a comparison of the bands used in each camera. It is important to note that the Tetracam Mini MCA and the Sentera QUAD offer the possibility of changing the optical filters upon request when ordering. Nonetheless, the comparison is done based on the default configuration of the cameras.

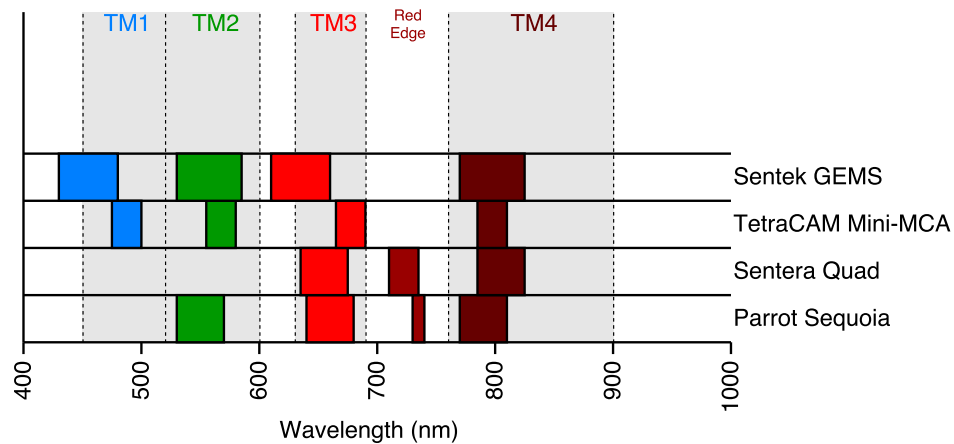


Figure 2.20: Comparison of spectral bands used in each camera.

2.3 UAV-Based Spectral Remote Sensing

Remote sensing is the science of collecting data about an object or phenomenon from a distance, without making physical contact with the object. In the spectral scope, remote sensing refers to the collection of data by detecting the energy that is reflected from the Earth's surface, with instruments and sensors usually mounted on large scale satellites and aircrafts.

A major area in remote sensing is the field of spectroscopy, in both hyperspectral and multispectral remote sensing, which measures the energy reflectance and absorption properties of vegetation, soils, rocks, and water bodies in the natural environment, generally under solar illumination. As mentioned before, the “traditional” approach has been to use large scale satellites and aircrafts to collect data. But the increasing use of UAV systems, and the miniaturization and cost reduction of spectroscopy electronics, has opened the door to UAV-mounted spectrometers, which are currently being used to quickly and easily obtain spectral data of a target area.

Spectral data obtained with light-weight and compact spectrometers mounted in UAVs can achieve significant match and a high correlation with the data obtained from similar ground-level equipment [41, 8, 42]. While ground-level measurements can generally achieve higher sensitivity and accuracy, UAV-based measurements have shown a lower standard deviation due to the larger field of view [41]. Therefore, it is possible to obtain reliable and accurate spectral data from UAV-mounted spectrometers without considerable losses, making this technique a faster and lower-cost alternative to “traditional” methods of spectral data collection. The following sub-sections cover some major applications in spectral measurements and remote sensing, with a larger focus on UAV-based hyperspectral and multispectral imaging systems.

2.3.1 Crop Inspection and Precision Agriculture

A critical element in agriculture is the inspection of crops to determine its health and quality. This information is crucial for farmers as a way to maximize crop growth, increase yields and reduce crop damage. Precision agriculture is the use of measured characteristics of soil, and the factors that affect it, in farming and the management of crop fields. In this regard, the most important parameters related with crop growth are nutrient status, weed infestation, disease affectation and water management [43].

Healthy vegetation, and more specifically their leaves, exhibit optical characteristics such as (a) low spectral reflectance at visible light (from 400 to 700 nm) due to strong absorption of these wavelengths by the chlorophyll (pigment found in plant leaves); (b) high spectral reflectance at near-infrared light (from 700 to 1100 nm) due to multiple scattering at the air-cell interfaces in the leaf internal tissue [44]; and (c) low spectral reflectance in the short-wave infra-red (SWIR) band due to strong absorption by leaf constituents such as water, proteins, and carbon components [45].

For remote sensing purposes, spectral images can be used to extract important information on vegetation parameters, such as canopy density, height, and clumping [46], nitrogen content [47], leaf area index [48], foliar water content, and soil properties, such as soil surface roughness [49] and soil moisture content [50].

In evaluating and interpreting remote sensing measurements of vegetation, several indices are used as graphical indicators of the existence of live green vegetation. The first one is the Normalized Difference Vegetation Index (NDVI), calculated by

$$NDVI = \frac{NIR - R}{NIR + R} \quad (2.11)$$

where R and NIR are the spectral reflectance measurements acquired in the visible (red) and near-infrared regions, respectively. Other indices like the Green Normalized Difference Vegetation Index (GNDVI) and the Normalized Difference Red Edge Index (NDRE) are also used for the same purpose while providing different levels of information. In the GNDVI (2.12), the red part of the standard NDVI is replaced with a very specific band of light in the green range (G).

$$GNDVI = \frac{NIR - G}{NIR + G} \quad (2.12)$$

Similarly, in the NDRE (2.13), the red part of the standard NDVI is replaced with a red edge (RE) spectrum centered around 715 nm.

$$NDRE = \frac{NIR - RE}{NIR + RE} \quad (2.13)$$

There is a large number of additional indices that have been designed to extract specific information. It is important to note that crops spectral measurements and therefore vegetation indices in field conditions are affected by interference factors such as mixture of vegetation, soil-brightness, environmental effects, shadow, soil color and moisture [51].

Hyperspectral imaging systems have been successfully used in the past to study crops using vegetation indices (VI). Part of Nebiker et al. [8] experiments included plant vitality assessment using a high-end spectrometer and a low-cost consumer-grade NIR camera mounted on a UAV. In this work, a first study found a correlation between rape yield crops and NDVI values of 0.78 for treated plots and 0.35 for untreated plots. Moreover, vitality differences among all the crops were identified and it was found that the use of fungicides prolonged plant activity up to harvest time. A second part of the vitality assessment study was done using different species of barley crops. In this study, correlations varied considerably depending on the index used (NDVI, GNDVI and NDRE) and the barley specie. Some species showed a low correlation with one or even two of the three indices, while other species showed a high correlation with all three indices. These results indicated that indices and species under study must be correctly matched in order to get the most accurate measurement.

Vegetation indices extracted from multispectral and hyperspectral images can be used with a high level of accuracy in estimating vegetation vitality and density [10] and by performing successive measurements over a period of time it is possible to estimate the growth rate of crops [52, 9].

Previous works have also demonstrated it is possible to measure the level of nitrogen in crops using hyperspectral imaging systems. Most nitrogen levels in plant leaves is found in chlorophyll molecules, therefore, there is a strong relationship between leaf nitrogen content and leaf chlorophyll content [53]. An increase in visual reflectance of plants is related to the decrease in chlorophyll content as a result of low nitrogen supply, whereas an increase in near-infrared (NIR) reflectance is associated to an increase in leaf area and green biomass. Therefore, by measuring leaf reflectance it is possible to predict crop nitrogen levels and therefore estimate the level of vegetation, health and crop growth.

In experiments done by Zheng et al. [54] and Agüera et al. [43], UAV-mounted spectrometers were used to collect data from rice and sunflower crop fields, finding strong relationships between vegetation indices values and the levels of nitrogen in the crop fields. Pölönen et al. [55] were also able to estimate biomass and nitrogen content of wheat and barley fields using a UAV-mounted hyperspectral camera. In this study, four vegetation indices were tested, with FVA (linear) giving the best correlation of 0.814 and 0.72 for biomass and nitrogen content respectively.

It is also possible to use hyperspectral images and vegetation indices to analyze, detect and track plant stress levels. One of the most common sources of plant stress is diseases and infestations. At early stages, plants react to the presence of a pathogen with some physiological mechanism such as a decrease in the photosynthesis rate, which leads to an increase of fluorescence and heat emission [44]. At a later stage, pathogens cause a reduction of chlorophyll content in leaves due to necrotic or chlorotic lesions [56]. A decrease in chlorophyll increases reflectance in the visible light band and causes a shift of the red-edge position in the spectrum. At the canopy scale, infections can change canopy density and leaf area. While these effects do not provide unambiguous indication of a specific stress, they can provide information for early detection and anticipation of non-normal conditions.

Nebiker et al. [8] captured spectral images of an onion crop field using a UAV on two different dates and found a substantial difference in NDVI values that were used to identify an infestation of thrips. Similarly, an infestation of blight was also detected by analyzing the changes in NDVI values from two flights over a field of potato crops. Näsi et al. [57] developed a processing approach based on UAV-based hyperspectral imagery that was used to identify spruce trees suffering from an infestation of bark beetle, and achieved a accuracy of 90% in separation between healthy and dead trees. Similarly, Garcia-Ruiz et. al. [58] achieved an accuracy of 85% in the detection and classification of Huanglongbing-infected citrus trees using high resolution hyperspectral images taken from a UAV. It was also found that the early stage branch-level disease could be detected by performing low altitude flights.

Another commonly found form of plant stress is due to lack of water, which directly affects photosynthesis and chlorophyll content in leaves [59, 60], and therefore affects the spectral reflectance signature of plants. Zarco-Tejada et al. [61] were able to track stress levels in a citrus crop using thermal and hyperspectral imagery obtained with a UAV, identifying areas where water was deficient.

The successful deployment of UAV-mounted hyperspectral cameras and the extraction of accurate information for the assessment of plants vitality and growth and the detection of plant stress conditions make it possible to use these systems for advanced precision agriculture and remote sensing of vegetation and crops.

2.3.2 Surface and Soil Study

Hyperspectral images taken from UAVs have also been successfully used for surface and terrain studies, detecting soil and vegetation marks, and surface modeling. Themistocleous et al. [11] combined UAV and ground hyperspectral data to study the formation of crop and soil marks for archaeological applications, while Honkavaara et al. [62] were able to measure the 3-D surface model and surface moisture of a peat production area using light-weight hyperspectral frame format cameras from a UAV. Turner et al. [12] also used a multispectral camera together with a visible camera and a thermal infrared camera to study the physiological state of Antarctic moss ecosystems.

Dry soil presents a higher albedo due to the high reflectance of its constituents. Moist soil will exhibit a low albedo due to water absorbing light. Bryant et al. [63] evaluated hyperspectral measurements for monitoring surface soil moisture, and found a strong correlation between reflectance and soil moisture within 3 cm of depth. Similarly, Finn et al. [64] compared soil moisture measurements between airborne hyperspectral data and equivalent ground readings. A strong correlation (R^2 greater than 0.7) was found in the 1000-1600 nm band for a 5.08 cm (2 inches) depth. Multispectral tests from a UAV were reported by Hassan-Esfahani et al. [13] in successful estimation of surface soil moisture over a large field irrigated by a center pivot sprinkler system. The multispectral data combined with an artificial neural network developed to quantify effectiveness of the method reported a high correlation (R^2) of 0.77.

2.3.3 Surface Hydrocarbon Detection

The use of hyperspectral and multispectral imaging for the detection of hydrocarbons in the surface, thus being able to identify such hydrocarbons, can be a considerable improvement for environmental and industry monitoring. Just the petroleum industry is responsible for a large amount of leaks and spills that commonly occur during transportation, storage, and manipulation of, not just petroleum, but also its related products. Therefore, it is of great interest to be able to detect and prevent these

events. Allen and Krekeler [65] performed a series of experiments with light, intermediate and heavy crude, and also some common refined products (E85 fuel, gasoline, diesel, and motor oil) over a range of substrates that include concrete, asphalt, gravel, grass, sands, and clays. They were able to detect and identify these hydrocarbons from each other and water using an ASD FieldSpec Pro-FR2 spectrometer. Airborne hyperspectral data has also been collected and used for the detection of hydrocarbons. Hörig et al. [66] flew a HyMap hyperspectral sensor and detected hydrocarbons on the ground surface. It was shown that hydrocarbons are characterized by a typical absorption maxima at 1730 nm and 2310 nm.

Analysis of data collected using the Airborne Visible Infrared Imaging Spectrometer (AVIRIS) during the Deepwater Horizon spill provided a quantitative way of estimating oil thickness and oil-water ratio [67]. Oil thickness and emulsion ratio maps were generated by Clark et al. [68] using the oil absorption bands, which later were used to estimate oil volume.

Work has also been done in detecting and estimating the bitumen content of oil sands using infrared spectra. Rivard et al. [69] demonstrated that hydrocarbons in Athabasca oil sands have distinct features in the infrared spectra region. In another experiment, they were able to estimate the bitumen content of oil sand ore samples using hyperspectral reflectance spectra in the 300-2500 nm range [70].

2.3.4 Environmental Monitoring

The general study of environmental phenomena and the effect of human activity in the environment can also be assessed using spectral imagery techniques. Hausamann et al. [71] performed studies oriented towards the detection of gas leaks from pipeline installations using UAV spectral remote sensors. This type of monitoring is of relevant importance in order to detect problems early and prevent negative environmental impacts. Tuominen et al. [72] reported using hyperspectral remote sensing techniques for monitoring nuclear fuel repository sites in search for environmental changes.

Experiments have also been performed using UAV spectral measurements in volcanology. McGonigle et al. [73] used a UAV mounted spectrometer to study a volcano in Italy and were able to successfully measure carbon dioxide flux in the volcanic gas.

2.3.5 Archaeology

Spectral imaging is also an important data collection method used in archaeology. Studies have been done in ways to extract archaeological information using vegetation indices and crop marks [74, 75]. Furthermore, the increasing use of UAVs for archaeological remote sensing provides a quick documentation, monitoring, and visualization tool that is easy, quick, and comes at a low cost. Cowley et al. [76] put together a comprehensive list of UAV based surveying methods for archaeological

studies and highlights the usefulness and beneficial impacts of this technology in the field. A study case in this publication was done by Moriarty [77], in which a UAV based multispectral camera was used for identifying and monitoring crop marks matched with archaeological regions of interest. The tracking of changes in the crop marks allowed the classification of all the regions across the area of study. Similarly, Themistocleous et al. [11] acquired spectral data from a UAV and were able to identify the formation of crop and soil marks tied to archaeological remains. With this method, it was possible to attain a greater level of accuracy in delimiting the areas of interest.

Chapter 3

UAV Development

This chapter presents the development of a fixed-wing UAV as part of the setup stage for testing UAV payloads. The intention was to develop a reliable UAV that could serve as a testing platform for long term research applications. While off-the-shelf airframes provide certain level of flexibility, in most cases it is not enough and modifications or adaptations are usually needed. The decision to redesign an existent off-the-shelf UAV platform comes from the need to have a high level of modularity so that it is flexible enough to be used in different applications. The goal was to study, modify, and improve the fixed-wing UAV platform used by the University of Alberta Aerial Robotics Group (UAARG). Making this the starting point helped leveraging the existent knowledge and experience, thus reducing the development time. The airframe is complemented with a customized UAV system board that integrates all UAV essential navigation and control functions, together with a redundant power supply board that provides main and backup power regulation.

The following sections describe the design and development of the airframe of a fixed-wing UAV and a fully integrated UAV system board with redundant power supply. The UAV platform described in this chapter, both airframe and electronics, is used for testing the payload systems developed in the subsequent chapters, and is part of the complete UAV solution presented in this thesis.

3.1 UAV Electronic System

A fundamental feature of many UAVs is the autonomous navigation system, which is based on an onboard autopilot computer that controls and guides the UAV in flight without assistance from human operators. Increasing efforts have been made in both hardware and software in order to produce reliable and robust autopilot platform solutions. Currently, there are a large number of hardware development boards available that can be used with a wide range of fixed-wing and rotary-wing airframes. Besides a hardware platform, these solutions bring a full software package for tasks

like programming, calibration, tuning, simulation, and monitoring. Chao et al. [78] made a survey on existing autopilot platforms at the moment, comparing the main features of both proprietary and open-source solutions. More recently, Lim et al. [79] and Ebeid et al. [80] made an extensive comparison of available open-source autopilot hardware and software platforms. These complete solutions can make the task of building and flying a UAV relatively easy and fast.

Some hardware platforms are designed to be a minimal solution, relying on additional dedicated boards or modules that are wired together, giving some flexibility to the user for assembling a customized final system [81]. Other approaches are focused on full integration of components into a single board, aiming for simplicity and reduction of wiring [82, 83]. A minimal autopilot system includes an onboard processor and attitude sensors (accelerometer, gyroscope and magnetometer). Additional standard components that are usually needed (depending on the airframe and application) and connected to the autopilot base board are: motor(s), servo(s), Global Positioning System (GPS) unit, pressure sensor, RF telemetry transceiver, and remote control (RC) receiver for manual flight control.

Another feature that is not commonly found in a UAVs electronic system is a redundant power supply that allows the UAV to recover from a main power loss. This feature has been explored in some concept development designs [83] and is found in some high-end proprietary solutions [84].

This section presents a comprehensive autopilot system board for UAVs [85] that integrates all essential sensors and components. The features and parts of the board are described in detail, emphasizing the high level of integration that simplifies the assembly, reduces wiring and weight, and increases reliability.

A secondary fully compatible, detachable, and novel board is also presented, that provides power regulation and redundancy. The architecture of this module is presented in detail, highlighting the parallel power supply approach used, which results in minimal power loss and instant switching from main to backup power supply.

3.1.1 UAV System Board

The first module is the system board which incorporates all common UAV electronics, including basic sensors, Microcontroller Unit (MCU) and communication ports. Additionally, the board features an on-board data logger with a microSD card port, gates to enable/disable Pulse Width Modulation (PWM) control outputs (typically wired to an enable switch), and an expansion port that gives access to most MCU pins. Important features are described in more detail in the following sections. A detailed user guide for this board can be found in Appendix A.

The UAV system board was designed to be fully compatible with the existing Lisa MX v2.1 class autopilot board designed by 1BitSquared, which is similar to the Lisa M autopilot board [86] with

an upgraded MCU. This boards are supported in the Paparazzi-UAV project [87, 86, 88], which is an open-source ground and airborne software architecture UAS platform. This compatibility saves any need to develop custom software and gives the possibility to reuse the existing firmware files designed for the Lisa MX board. The Lisa MX was selected mainly because of its powerful MCU. Figure 3.1 shows the block diagram of the autopilot board hardware.

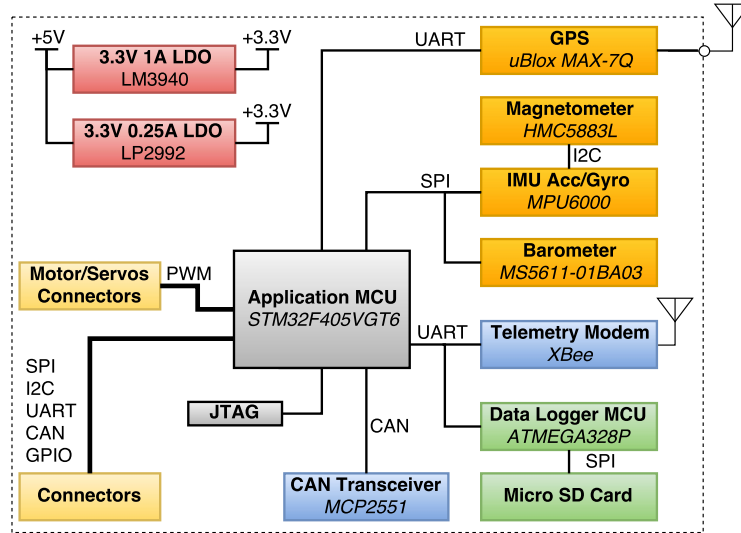


Figure 3.1: Block diagram of the UAV system board hardware.

3.1.1.1 Microcontroller Unit (MCU)

The UAV system board is built around the STMicroelectronics STM32F405VGT6, a 32-bit ARM® Cortex® M4 MCU running at 168MHz with 192KB RAM, 1024KB Flash, and Floating Point Unit (FPU). The MCU includes 82 I/O, 10 Timers, and CAN, I2C, I2S, SPI and UART communication interfaces in a LQFP-100 package.

3.1.1.2 Inertial Measurement Unit (IMU)

The 10 Degrees-of-Freedom (DOF) or 10 Degrees-of-Measurement (DOM) Inertial Measurement Unit (IMU) is comprised by an integrated 3-axis accelerometer and gyroscope (Invensense MPU6000), a 3-axis magnetometer (Honeywell HMC5883L) and a barometer (Measurement Specialties MS5611-01BA03). The accelerometer/gyroscope and barometer are connected via SPI interface to the MCU, and the magnetometer is connected to the accelerometer/gyroscope via I2C interface. The accelerometer/gyroscope acts as a master with the magnetometer, pulling the data and saving it locally, allowing the MCU to extract data from these three sensors directly from the MPU6000 via SPI.

3.1.1.3 GPS

The system includes a uBlox MAX-7Q GPS module with a super-capacitor for hot start and corresponding antenna matching circuitry. The GPS works in the 1575.42Mhz band and the antenna circuitry includes a SAW filter and optional Low Noise Amplifier (LNA) that can be bypassed if used with an active antenna. The board supports antennas with either uFL or SMA connectors. The connectors can be selected using zero ohm jumper resistors. When power is off, the super-capacitor is capable of keeping the GPS module in backup battery mode for approximately 20 minutes to allow for hot start [81]. The GPS is connected to the MCU via a UART communication interface. Optionally, when an external GPS unit is used, the on-board GPS can be powered off and disconnected from the MCU by means of on-board jumpers. The external GPS can then be powered and connected to the MCU UART port using the corresponding connector.

3.1.1.4 XBee and Data-logger

A socket is included for connecting an XBee RF transceiver module for telemetry. The XBee is connected to the MCU via UART communication interface. A secondary MCU based on an Atmel AVR 8-bits 16Mhz ATMEGA328P logs the telemetry data from the serial port to a micro-SD card. This data-logger uses a modified version of the open-source “OpenLog” firmware that was adapted for Paparazzi by the Paparazzi team. The data-logger starts running and saving data automatically after power up. The board includes a jumper for powering on/off the data-logger.

3.1.1.5 PWM Outputs

There are eight PWM outputs that can be used to control motors and servos. Output signals run through gates and each signal can be enabled/disabled by connecting a switch or a jumper to one of two user control inputs that can be accessed from an on-board connector. This functionality provides an easy way to have kill-switches for turning off PWM signals to the motors and servos independently. This feature is useful for debugging, programming and tuning output signals while keeping the motors off. This also serves as a safety feature that can prevent human injury, damage to servos while programming, accidental motor spinning and fly-away incidents. PWM outputs can be assigned to either the motor or the servo group by using solder jumpers (one for each output).

3.1.1.6 Power Regulation

The on-board power supply is split into two 3.3V Low Drop-Out (LDO) linear voltage regulators with +5V input. The first voltage regulator (Texas Instruments LP2992AIM5-3.3) powers the accelerometer, gyroscope, magnetometer and barometer sensors, so as to reduce noise in the measure-

ments, while the second voltage regulator (Texas Instruments LM3940IMPX-3.3) powers to the rest of the board. The latter is capable of delivering up to 1A of power.

3.1.1.7 Additional Features

Finally, the UAV system board has additional I2C, SPI, CAN, and UART ports for external communications, analog inputs, GPIOs, bind button, status LEDs, and connection for two radio control (RC) receivers. Some communication ports have dedicated connectors and most MCU pins are accessible through a 48-pin expansion header. The expansion header provides the opportunity for the design and use of daughter boards and “shields”, increasing flexibility and expanding functionalities. The features of the UAV system board are summarized in table 3.1.

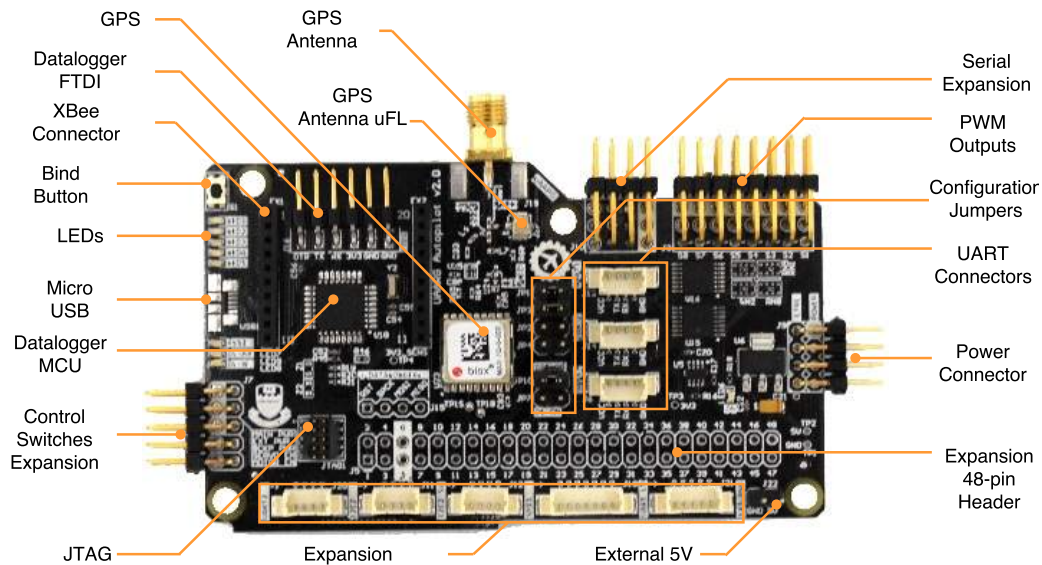


Figure 3.2: UAV system board. 90x52mm 4-layers PCB with a weight of 29 grams. A detailed manual and user guide for the board can be found in Appendix A.

Table 3.1: UAV System Board Features

| Characteristic | Specifications |
|-----------------|--|
| Microcontroller | STM32F405VGT6 |
| 10 DOF IMU | 3 axis accelerometer 3 axis gyroscope 3 axis magnetometer barometer |
| Remote Control | Two UART ports for remote control receivers |
| GPS | One uBlox MAX-7Q GPS unit The GPS on-board circuitry includes: - SAW filter - Optional LNA - Selectable uFL or SMA connector for GPS antenna |
| Connectivity | 8 PWM, 1 JTAG, 1 SPI, 2 I2C, 1 CAN, 3 GPIO, 3 ADC, 1 UART |
| Data-logger | Secondary MCU and micro-SD card socket for telemetry data-logging |
| Power | 3.3V@1A voltage regulator |
| User Interface | Bind button Eight status LEDs |
| Size and weight | 90x52 mm, 29 grams, 4 layers PCB |

3.1.2 Redundant Power Supply Board

The second module is a redundant power supply board comprised of main and backup voltage regulators, shown in Figure 3.3. This module was designed as a secondary and optional board that provides main power for regular operation and backup power for emergency operation. Both main and backup run on separate battery packs. The purpose of the backup power supply is to provide power to the UAV system and servos in case the main battery or main power supply fails, so that a controlled emergency landing of a fixed-wing UAV can be performed. If the backup power is not required the board can be easily replaced by any 5V power supply with enough current to power the UAV system board.

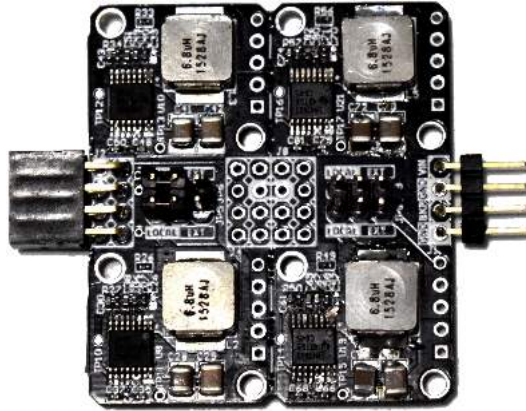


Figure 3.3: Redundant Power supply module. 41x46mm 4-layers PCB with a weight of 14 grams. There are four voltage regulators, from bottom left and clockwise: autopilot main, payload, servo backup, and autopilot backup.

Each voltage regulator is based on the Texas Instruments LM43603PWPT synchronous step-down DC-DC buck converter, which is capable of delivering up to 3 A from an input voltage that can go up to 36 V, suitable for up to an 8 series cell lithium polymer battery. Furthermore, each voltage regulator has over-temperature thermal shutdown protection, output short circuit protection, and adjustable switching frequency. There is also a low battery voltage protection feature that shuts down the regulator if the input voltage goes under a certain threshold, thus protecting the battery from over-discharge damage. This threshold is adjustable by means of an on-board voltage divider. The output voltage is also variable and can be adjusted by replacing a single resistor. This design uses backup voltage regulators placed in parallel with the main voltage supply, taking advantage of the high impedance of the output of the LM43603PWPT when it is off. A small difference in regulator set point (e.g. 100mV) keeps the backup power supply in standby as described below.

Figure 3.4 shows the connection diagram of the main and backup power system with the rest of the airplane electronics in the two possible operation modes. Under normal power operation (Figure 3.4a) only the main battery is used, all systems are on and the two backup regulators (autopilot and servo) are inactive.

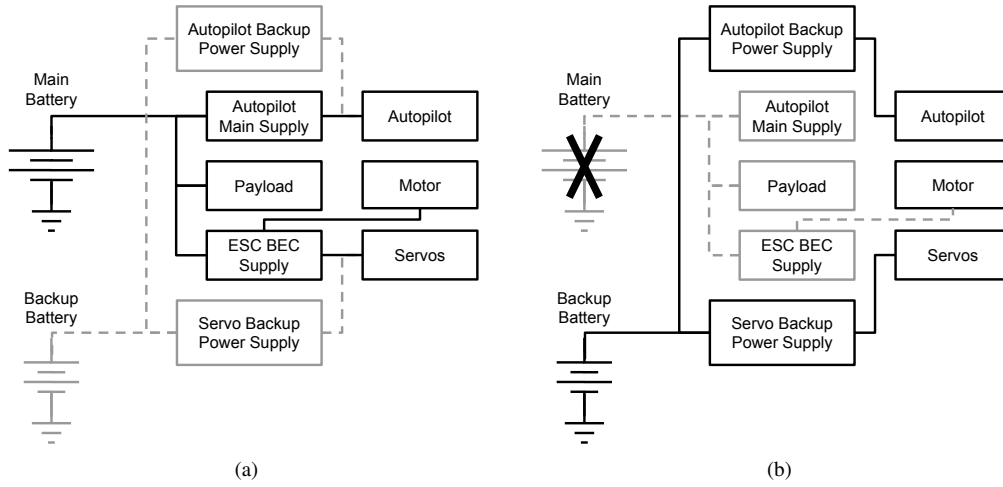


Figure 3.4: Redundant Power supply module block diagram. Greyed blocks and dashed lines are inactive. (a) Normal power operation mode: all systems are on and powered from main battery. (b) Backup power operation mode: autopilot and servos are powered from backup battery; motor, payload and Electronic Speed Controller (ESC) / Battery Eliminator Circuit (BEC) are off.

In the event of main battery or main power supply failure, the system enters in backup power operation (Figure 3.4b), where the backup battery is used. System board and servos are powered by the backup regulators. The payload, ESC and motor(s) remain off in this mode. When running on backup power for the system board (including telemetry radio and RC radio receiver) and servos, an emergency glide landing for a fixed-wing UAV can be performed without motor power. For the case of a main power supply failure in a rotary aircraft, telemetry, including situational awareness and GPS location for recovery would be maintained.

3.1.2.1 Principle of Operation

The operation of the redundant power supply is based on the the use of two voltage regulators connected in parallel (Figure 3.5), with the main regulator having a slightly higher voltage (V_{MAIN}) than the backup regulator (V_{BACKUP}), making the latter stay inactive while the former sources all the current. In the case when the main regulator shuts down, its output goes to high impedance and the backup regulator starts to source the current. V_{OUT} will always be the higher of the two supplies' voltages.

When both voltage regulators are on (normal operation mode), meaning the backup regulator is inactive due to the main regulator having a higher output voltage, there is a current flowing from the main regulator to the backup regulator. There is also a current drawn from the backup battery. Let us define these two currents as i_s , the current sunk by the backup voltage regulator while inactive,

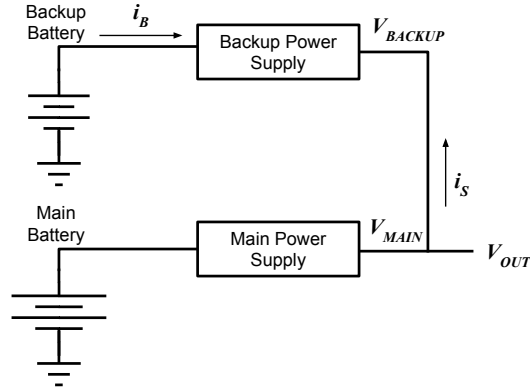


Figure 3.5: Main and backup power supplies connection diagram. Both power supplies are connected in parallel and there is a voltage difference between the two, where V_{MAIN} is slightly higher than V_{BACKUP} when in normal operation mode.

and i_B , the current drawn by the inactive backup voltage regulator from the backup battery (battery drain current). It is desired for these two currents to be as small as possible so that neither the main nor the backup batteries capacity is affected in a considerable way.

Current i_B is the result of the constant current drawn by the LM43603PWPT circuit when it is inactive (approx. $65\mu A$) plus the current dissipated in the voltage divider, which depends on the value of the resistors and the battery voltage. The value of the resistors should be in the range of $0.1-1M\Omega$, in order to keep i_B under $100\mu A$. Current i_S varies depending on the voltage difference $\Delta V = V_{MAIN} - V_{BACKUP}$. As shown in Figure 3.6, there is a threshold in the values of ΔV under which i_S becomes negative, meaning that the backup voltage regulator is active and starts sourcing current together with the main voltage regulator. It is desired to keep ΔV above such threshold in order to keep the backup voltage regulator inactive and i_S positive.

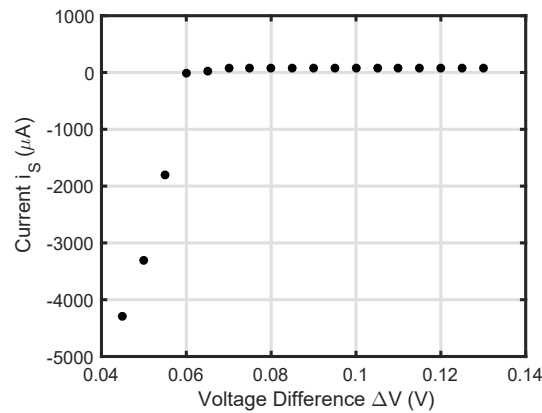


Figure 3.6: Variation of the current sank by the backup voltage regulator circuit (i_S) with the voltage difference $\Delta V = V_{MAIN} - V_{BACKUP}$, including the point of current inversion for a low ΔV in which i_S becomes negative.

Therefore, for any voltage difference $V_{MAIN} - V_{BACKUP} > 70\text{mV}$ the backup voltage regulator will remain inactive and the main voltage regulator will source all the current. Figure 3.7 shows that for a wide range of voltage differences ΔV , from 75mV to 130mV, the value of i_S varies slightly with a linear behavior from $72.6\mu\text{A}$ to $73.2\mu\text{A}$.

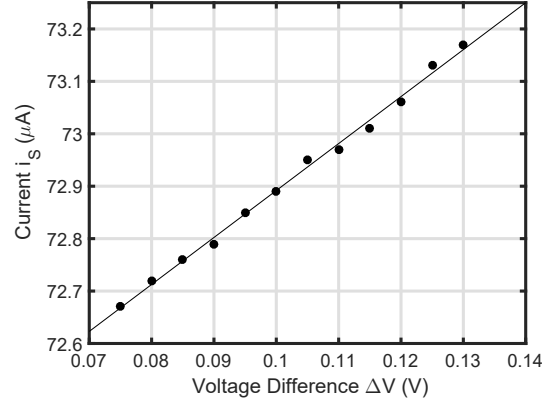


Figure 3.7: Variation of the current sank by the backup voltage regulator circuit (i_S) with the voltage difference ΔV when both voltage regulators are on ($\Delta V = V_{MAIN} - V_{BACKUP}$).

In the case of the backup voltage regulator being off (battery depleted or disconnected, or regulator forced off), its output goes to high impedance and the current i_S drops while still varying depending on the voltage seen at the output. Note that this scenario is the same as when the main battery is depleted and the main voltage regulator shuts down, enabling the backup voltage regulator (in this case i_S would be negative according to the direction defined in Figure 3.5). Figure 3.8 shows the relation between i_S and the output voltage V_{OUT} .

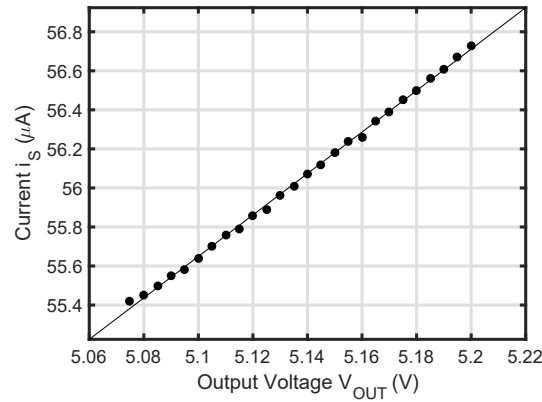


Figure 3.8: Variation of the current sank by the backup voltage regulator (i_S) circuit with the output voltage level (V_{OUT}) when the backup voltage regulator is off (output in high impedance).

3.1.3 Firmware and Ground Control Station (GCS)

As mentioned before, the UAV system board is compatible with the Paparazzi-UAV platform, and the same drivers, configuration files and code used for the Lisa MX can be used with this board. Flashing of the MCU can be done using any ARM Cortex MCU programmer, although the Black Magic Probe is supported by the software. The Black Magic Probe is a JTAG and SWD adapter designed by 1BitSquared and Black Sphere Technologies for programming and debugging ARM Cortex MCUs.

The *Paparazzi-UAV* software platform offers Ground Control Station (GCS), airborne code, flight plans, mission control, and communications [88] segments integrated in an open-source fully customizable distribution. The GCS (Figure 3.9) is an essential development, debugging, and visualization tool that allows interfacing easily with the UAV, both on the ground and during flight. It allows continuous and real time monitoring and logging of all variables including raw sensor readings, remote commands, and control outputs.

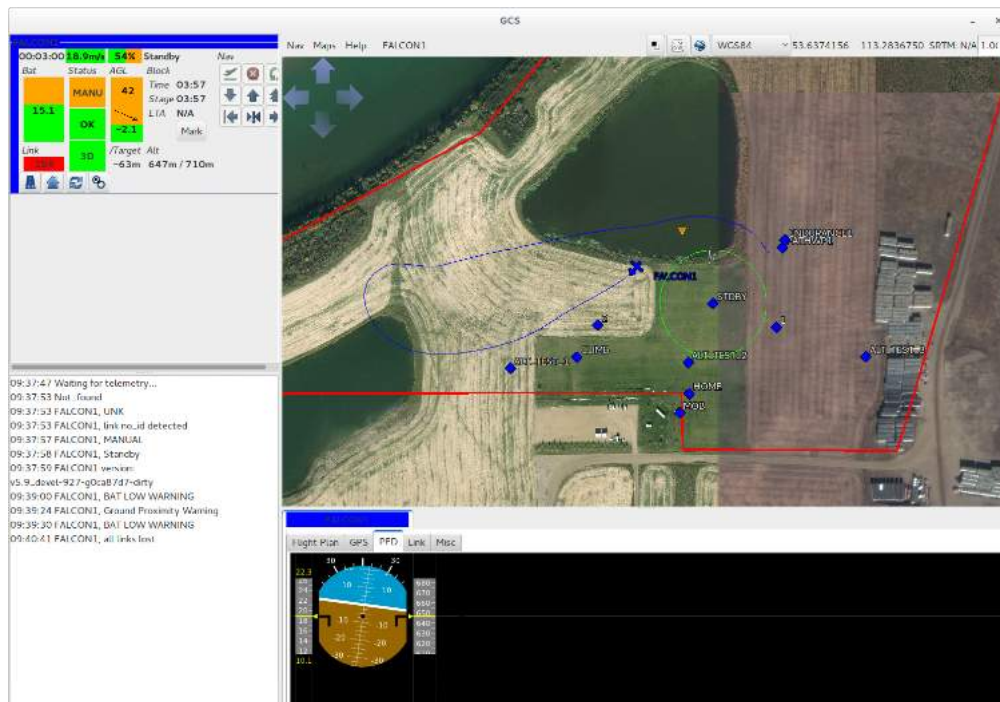


Figure 3.9: Paparazzi-UAV Ground Control Station (GCS) interface during a flight.

3.2 Payload Computer

The UAV is equipped with a single board computer (SBC) used for interfacing with payload and process real-time payload data. The ODROID-C2 was chosen for this task. The ODROID-C2 from South Korean manufacturer Hardkernel is a small and lightweight 64-bit quad-core SBC.



Figure 3.10: Hardkernel ODROID-C2.

The ODROID-C2 was loaded with Ubuntu 16.04. USB ports were used for interfacing with USB camera modules. A UART port accessible from the side male header was connected to the telemetry output of the system board for internal logging of data. The ODROID-C2 provides access to the terminal console via a UART link. This link was used to control the ODROID via command line from an external computer. Table 3.2 summarizes the technical specifications of the ODROID-C2.

Table 3.2: Technical Specifications of the ODROID-C2

| |
|--|
| - Amlogic ARM® Cortex®-A53(ARMv8) 1.5Ghz quad core CPUs |
| - Mali™-450 GPU (3 Pixel-processors + 2 Vertex shader processors) |
| - 2 Gbyte DDR3 SDRAM |
| - Gigabit Ethernet |
| - HDMI 2.0 4K/60Hz display |
| - H.265 4K/60FPS and H.264 4K/30FPS capable VPU |
| - 40pin GPIOs + 7pin I2S |
| - eMMC5.0 HS400 Flash Storage slot / UHS-1 SDR50 MicroSD Card slot |
| - USB 2.0 Host x 4, USB OTG x 1 (power + data capable) |
| - Infrared(IR) Receiver |
| - Ubuntu 16.04 or Android 6.0 Marshmallow based on Kernel 3.14LTS |

3.3 UAV Avionics Module

The final avionics module for the Falcon I airframe (covered in the next section) is a single assembly that can easily slide in and out of the plane (Figure 3.11). It contains all the main electronics including the UAV system board with the redundant power supply, a control switches board used to power on/off the boards and enable/disable the motor and servos, and the payload computer (ODROID). A minimal wiring is necessary for connections between the ODROID and the UAV system board, and USB cables from the ODROID are used for payload connection.

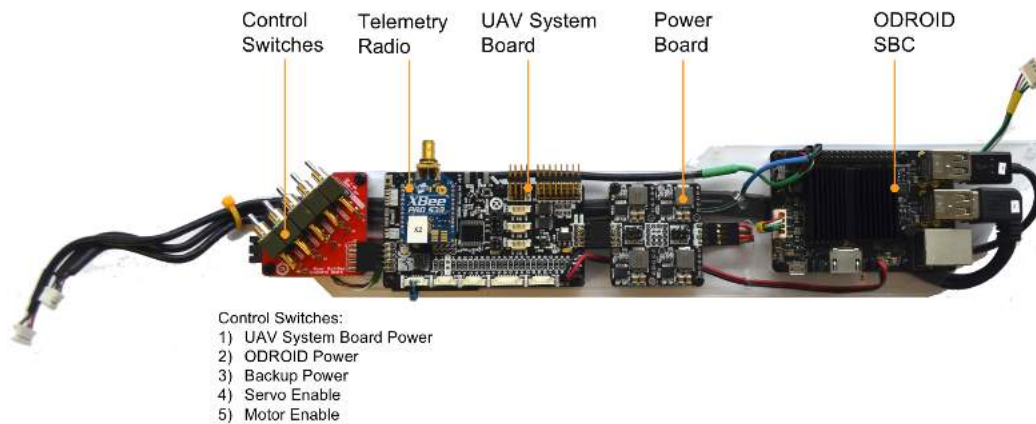


Figure 3.11: UAV avionics module fully assembled with all its components.

3.4 Airframe

The starting point for the airframe design was set based on the work done by the University of Alberta Aerial Robotics Group (UAARG). UAARG is a student vehicle project in the Faculty of Engineering of the University of Alberta. Their project is to design, build, test, and take to competition a fully autonomous UAV.

At the time, UAARG was using the HobbyKing EPP FPV airframe for their planes (Figure 3.12). The EPP FPV is a lightweight fixed-wing airframe made out of mostly expanded polypropylene (EPP). The fully assembled airframe has a total length of 1320mm, a wingspan of 1800mm, and weighs approximately 1000 grams just the airframe (no electronics, batteries, motors, etc).

UAARG would build the airframe, and then install all the avionics (autonomous navigation and control electronics) and payload systems. The first step was analyzing the system design, construction, setup and deployment procedures. This analysis, together with experience information provided by the team members, produced a list of problems and potential improvements.



Figure 3.12: HobbyKing EPP FPV airframe.

One of the major issues that was noted was inherent to the airframe design. The assembly process involves putting together the left and right wings, then placing the wings on top of the fuselage, align visually, and finally secure them with rubber bands. This setup is not reliable since the alignment of the wings with respect to the fuselage is done visually. It is almost impossible to do the placement the exact same way every time. While this might not represent a major problem during manual flight, where the pilot can compensate these inconsistencies by trimming the plane and adjusting to it, it does represent a considerable problem when it comes to autonomous navigation. One of the first steps in setting up the autonomous navigation system is to tune it according to the behavior and response of the plane. Once it has been tuned, the autonomous navigation system will be able to accurately control the plane. Tuning parameters are specific for each system. Therefore, if the assembly of the plane is not constant and repeatable, the tuning would have to be performed every time, otherwise the autonomous navigation system would underperform. Tuning involves time and effort, and it should be a one-time only step for as long as the plane is kept the same.

Another problem found in the airframe was the accessibility of the space inside the fuselage. With only two access points, top and front, installation and handling of the electronics is limited.

Considering that UAARG had been using the EPP FPV for 3 years at that time and that it has proven to be stable and easy to control, the plan was to keep using this airframe and take advantage of the existent knowledge and experience. With the aforementioned issues in mind a redesign of the plane was done. The aim was to solve the problems and produce a customized version of the airframe with a reliable and repeatable assembly, and optimize the space inside the fuselage for better use.

3.4.1 Falcon I

The Falcon I is the first iteration of the EPP FPV modified airframe. Measurements were taken from the original airframe and drawn in SolidWorks. Then, modifications were introduced on top of the base model. While the EPP material is very forgiving when it comes to hard landings and minor crashes, as it absorbs impacts very well, a more rigid material is needed for some parts like joints, attachments, etc. Therefore, some parts of the plane were replaced with plastic parts so as to strengthen and reinforce key structural points. Some of the plastic parts were designed to allow extra space were to put electronics, wiring, etc.

One of the most important aspects of the redesign was to split the fuselage in two, giving access to the inside space. This way, it was possible to work, modify, and optimize the inside of the fuselage to allocate the electronics efficiently (Figure 3.13). Some cuts were done in the inside of the fuselage to allocate more space (Figure 3.14), without affecting the overall structural strength of the body.

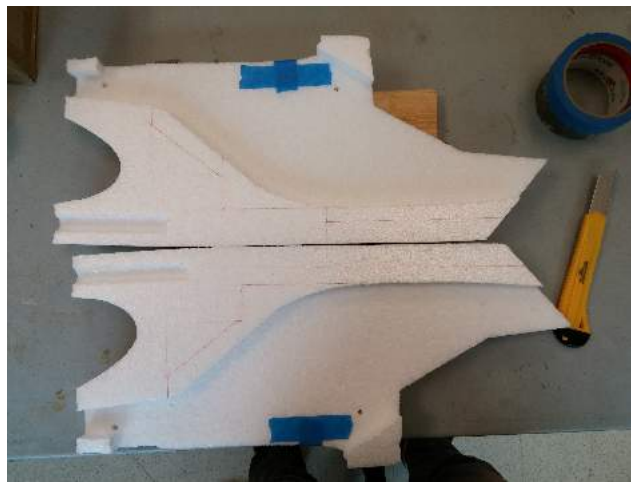


Figure 3.13: Inside of the HobbyKing EPP FPV fuselage after splitting. Inside cuts are marked and nose was removed.

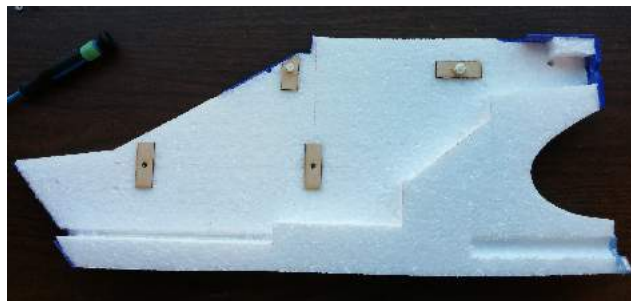


Figure 3.14: Side of the fuselage with cuts and some plastic parts glued already (right).

Figure 3.15 shows a comparison of the unmodified EPP FPV fuselage with the redesigned version. The parts shown in blue in the redesigns are made out of plastic. All plastic parts were designed to be 3D printed using polylactic acid (PLA) as the printing material. PLA is a biodegradable and bioactive thermoplastic aliphatic polyester commonly used in 3D printers. 3D printer settings used for these parts can be found in Appendix D.

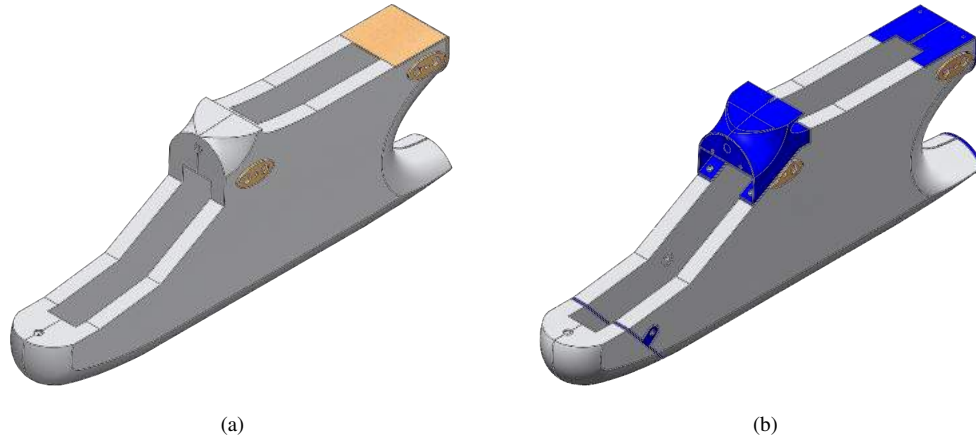


Figure 3.15: (a) Original EPP FPV fuselage. (b) Modified fuselage (Falcon I design).

A top fuselage module (Figure 3.16) was designed to fit the wings centre module and also be able to use the space inside of it to fit the GPS/GPS antenna and external magnetometer. The wings centre module (Figure 3.16) is a middle structure that goes between the wings and holds them together using rods for alignment and an attachment piece that is glued to the wings. It attaches to the top of the fuselage by means of the top fuselage module and two bolts at the back. The wings centre module is one of the major and most important additions to the design. It firmly holds the wings in place, keeps them aligned, and secures them to the fuselage. It is a repeatable and reliable assembly. This setup extends the wingspan from 1800mm to 1910mm, which increases the lift force. Moreover, the interior of the wings centre module provides additional space and still gives access to the interior of the fuselage.

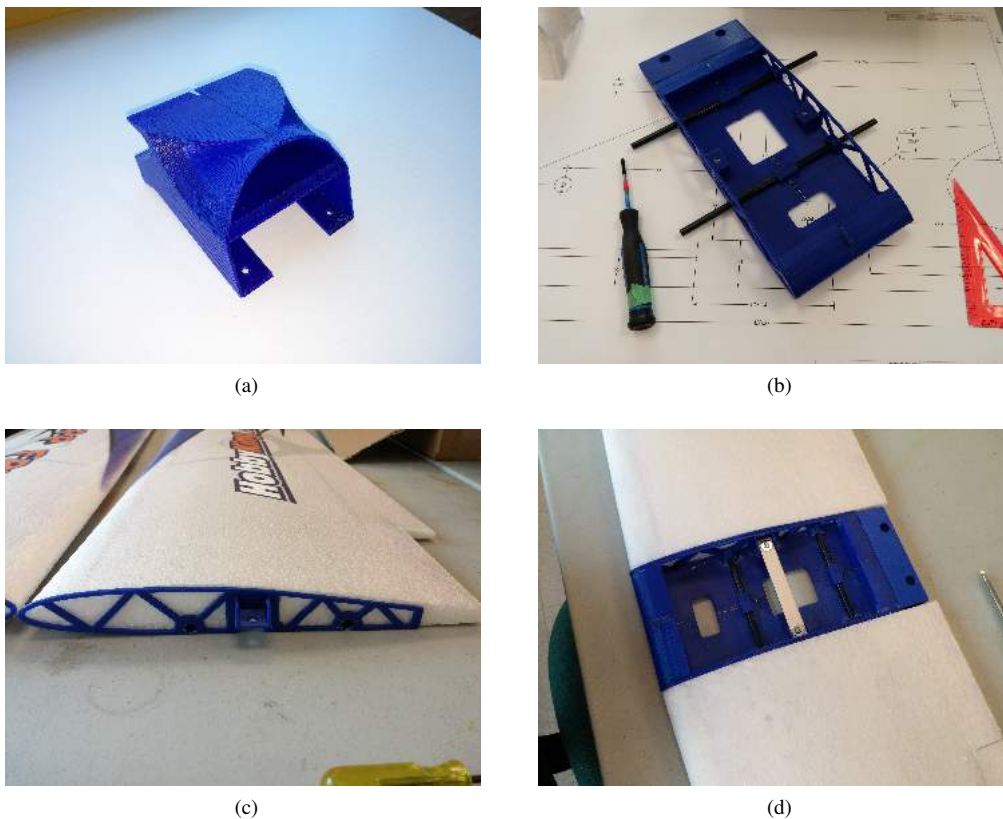


Figure 3.16: (a) Top fuselage module. (b) Assembled wing centre module. (c) Assembly attachment glued to the wings. (d) Wings assembly.

The tail was also redesigned (Figure 3.17). The default tail has wooden supports in the bottom that considerably increase drag. This structure was replaced with a tail centre module that connects to the tail boom and clears the way under the horizontal stabilizer. The vertical stabilizer is supposed to be glued to the horizontal stabilizer, but the new design allows the vertical stabilizer to be bolted onto the tail centre module, thus allowing disassembly for easy storage and transportation. The default design has elevator and rudder servos mounted on the tail boom close to the fuselage, with external wires and long rods. The new design incorporates servos embedded into the foam in both stabilizers. This reduces the length of the rods that connect to the rudder and elevator. Moreover, the servo wires travel inside the tail boom instead of outside. This new design has a cleaner setup that helps reduce drag, improves aerodynamics, allows for easy disassembly, and is more reliable with protected wires and short rods.

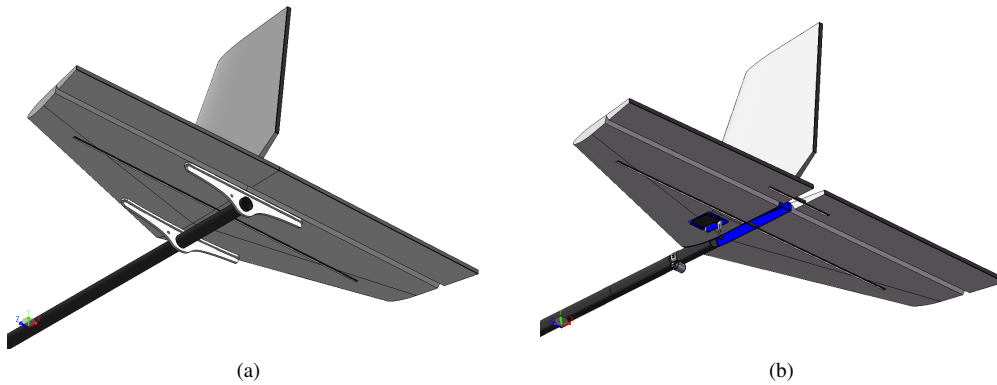


Figure 3.17: (a) Original EPP FPV tail. (b) Modified tail (Falcon I design).

The wiring inside the fuselage is more efficient in the new design as cables are embedded and secured into the foam (Figure 3.18a). For ease of assembly, wires are kept in just one side of the fuselage.

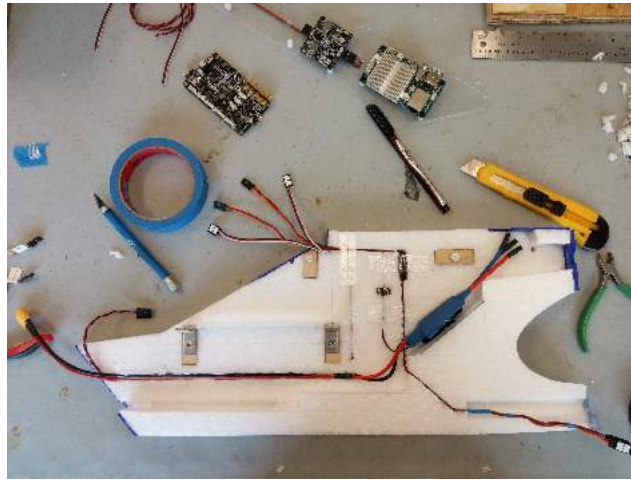


Figure 3.18: Internal wiring of the fuselage.

The new design uses the volume available in the nose of the plane for payload. A plastic nose (Figure 3.19b) was designed for integrating any payload that could fit in such volume. With this approach, it is possible to have multiple noses, one for each type of payload, depending on the needs. The base design of the plastic nose can be modified to carry any piece of payload, provided volume and weight permits. The nose attaches to the fuselage via six alignment pins and two screws. This system provides a solid and reliable attachment while making it easy to install and uninstall the nose. The default foam nose (Figure 3.19a) can be used when no payload is needed. Additionally, the new

design has the battery sliding into the fuselage from the front, thus the nose has to be taken out for inserting and removing the battery. Figure 3.20 shows a rendering cut of the interior of the fuselage with the electronics installed.

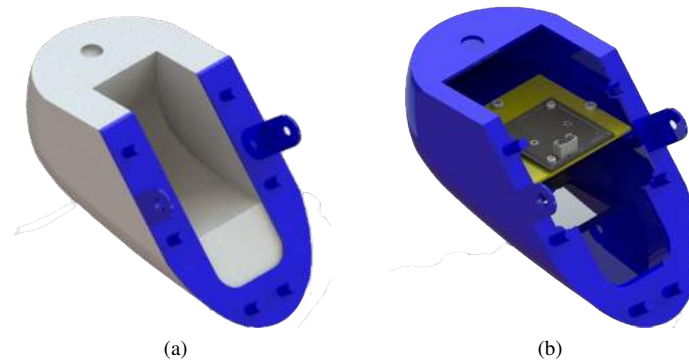


Figure 3.19: (a) Default foam nose. (b) Custom plastic nose for installing a USB camera board.

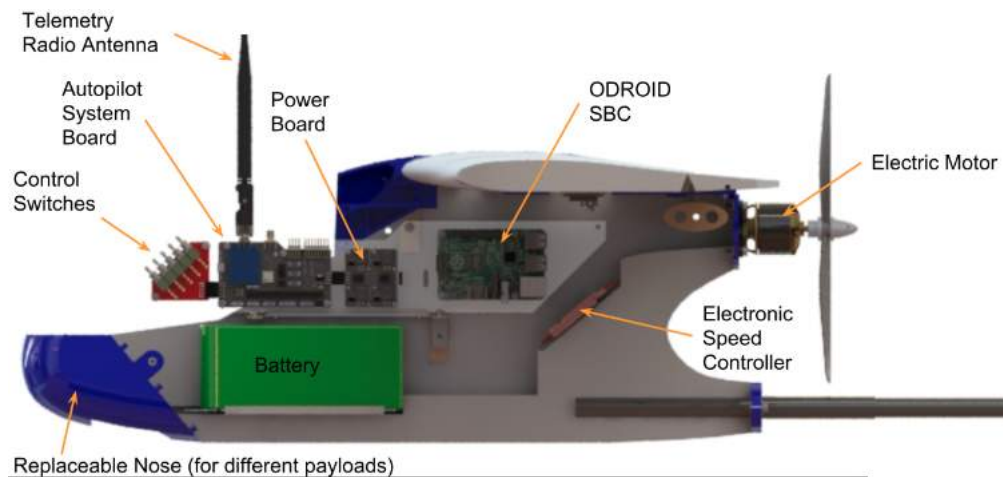


Figure 3.20: Rendering cut of the fuselage with internal components.

The main electronics (system board, power board, switches board, ODROID single board computer) was installed on a base board that slides into the upper half of the fuselage, while the battery pack slides into the bottom half. Switches in the front allow easy access to the user, and connections to the UAV system board from the top contribute to keeping a clean and organized wiring. The centre of gravity of the redesigned airframe was kept within the same range of the original.

The redesign of the airframe provides a more efficient use of volume in the fuselage, that allows for better allocation and organization of the components inside. Even though plastic parts are heavier

than foam, thanks to the reduction in weight in the electronics assembly and imaging payload, the overall weight of the fully assembled plane was reduced compared to the previous design. All plastic parts were design aiming for light-weight and high structural strength.

Previous designs had payload mounted on the the wings, while wings are kept intact in this redesign, with no holes or modification except for the attachment piece on the inside face, thus preserving their aerodynamic capabilities. All the electronics was moved inside the fuselage, bringing all heavy components closer to the centre of gravity and making easier to balance the plane.

The result is a lighter plane with an efficient use of space inside the fuselage. The balance between the original foam and the added plastic parts makes up for a reliable plane that achieves repeatability and can be assembled in a short time. The clean wiring and reduced size electronics make it easier to understand, learn, and handle by the user. The plane has been tested in multiple successful missions, and the University of Alberta Aerial Robotics Group (UAARG) adopted this redesigned version for their 2017 competition, and plan to continue working on top of this model. Figures 3.21 and 3.22 show the final assembly of the plane.

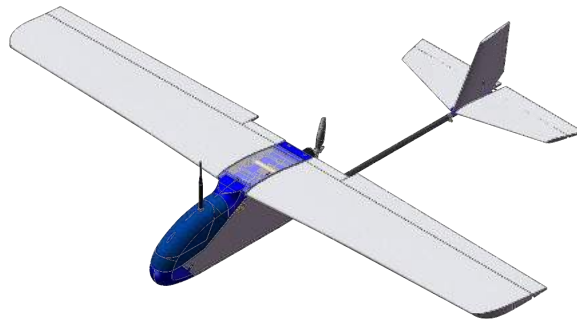


Figure 3.21: 3D model of the Falcon I full assembly.



(a)



(b)

Figure 3.22: Falcon I full assembly on the ground (a) and during flight (b).

Chapter 4

Proof of Concept Multispectral Imaging System

This chapter covers the development and experiments carried out with the initial prototype of a multispectral imaging system. The approach used in the development of the multispectral imaging system follows a sequence of incremental steps based on prototyping and validation before the subsequent step. Several iterations of the system were produced throughout the project and are detailed in this chapter and the next. The first section of this chapter describes the initial work done with USB camera modules, which led to the use of these cameras in the development of subsequent multi-camera imaging systems. The second section of this chapter details the development of a 3-band multispectral imaging system based on USB camera modules.

4.1 USB Camera Modules

There is a large variety of USB camera modules in the market targeted to areas that range from research to industrial use. The first steps in the process of working with USB cameras was doing the necessary research about this technology and becoming familiar with its features and capabilities. The main features, as well as the advantages and disadvantages of this type of cameras are covered in 2.1.5. In this same section it is stated that the interest is focused on USB2.0 cameras compatible with the UVC driver.

4.1.1 Selection and Evaluation

The first step was to acquire a prototyping camera that could be used to validate the information found in the literature, as well as test the camera and evaluate its performance. With this in mind a first selection was made. Camera ELP-USB500W02M from China based manufacturer *ELP Ailipu Technology Co.*¹ was selected as the first prototyping device. Table 4.1 shows the main features of this camera module.

Table 4.1: Features of the ELP-USB500W02M camera.

| | |
|--------------------|---------------------------|
| Manufacturer | ELP Ailipu Technology Co. |
| Part Number | ELP-USB500W02M |
| Sensor | Omnivision OV5640 |
| Sensor Type | CMOS |
| Maximum Resolution | 2,592x1,944 pixels |
| Pixel Size | 1.4 μm |
| Image Area | 3,629 x 2,722 μm |
| Shutter | Rolling |
| Power Consumption | ~ 200 mA @ 5 VDC |
| Module Size | 38 x 38 mm |

This camera was selected mainly because it provides a variety of settings that can be used to test multiple configurations. It provides 10 different resolution configurations, both raw (YUYV) and compressed (MJPG) output formats, and a variety of settings like brightness, contrast, hue, saturation, gamma, exposure, etc. In addition to its low cost, it is an excellent choice for performing all the initial testing and evaluation. Figure 4.1 shows a picture of the ELP-USB500W02M.



Figure 4.1: USB camera module ELP-USB500W02M from ELP Ailipu Technology Co.

¹<http://www.elpcctv.com/>

4.1.2 Software Development

Software development with this camera was done in a Linux environment and based on the use of the native UVC driver (section 2.1.5.1) through the Video for Linux Two (V4L2) API (section 2.1.5.2). This type of camera can be compared to webcams in so much as components and interface. Thanks to the UVC driver the camera works as a plug-and-play device. It is possible to connect the camera to a computer via USB and open it using a video capture program (e.g. Cheese, Gvvcview, VLC). For example, Gvvcview² will provide a Graphical User Interface (GUI) with a first window showing live streaming video captured from the camera, and a second window with the settings accessible in the camera.

Further interest was in finding a way to programmatically control the settings of the camera without having to open a GUI. v4l2-ctl is a tool to access V4L2 drivers from the command line. This tool is part of the v4l-utils library, which is a bundle of packages for handling media devices. Using v4l2-ctl is possible to obtain information from a connected camera and control its settings. Information such as a list of all the settings with details of the type of field (e.g. int, bool), the range of accepted values, and the default value can be read from the camera. It is also possible to obtain a list of the possible video output formats supported by the camera, as well as the combination of resolution and frame rate options for each. Tables 4.2 and 4.3 list the camera settings and output formats respectively for the ELP-USB500W02M.

Table 4.2: Settings of the ELP-USB500W02M camera.

| Setting | Type | Min | Max | Step | Default |
|--------------------------------|---------|-------|-------|------|---------|
| Brightness | integer | 0 | 15 | 1 | 8 |
| Contrast | integer | 0 | 15 | 1 | 8 |
| Hue | integer | -10 | 10 | 1 | 0 |
| Saturation | integer | 0 | 15 | 1 | 7 |
| Sharpness | integer | 0 | 15 | 1 | 6 |
| Gamma | integer | 1 | 10 | 1 | 7 |
| White Balance Temperature | integer | 2,800 | 6,500 | 1 | 2,800 |
| Backlight Compensation | integer | 0 | 1 | 1 | 0 |
| PowerLine Freq. (Anti Flicker) | menu | 0 | 2 | - | 2 |
| Focus | integer | 0 | 21 | 1 | 16 |
| Exposure Auto | menu | 0 | 3 | - | 3 |
| Exposure | integer | 4 | 5,000 | 1 | 625 |

An useful feature of camera is the automatic exposure setting (Exposure Auto), where the camera

²<http://gvvcview.sourceforge.net/>

takes care of adjusting the exposure and some internal gain setting in order to keep frames with the right amount of light.

Table 4.3: Frame Rates for the ELP-USB500W02M camera based on output video format and resolution.

| Resolution | Frame Rate @ MJPG | Frame Rate @ YUYV |
|-------------------|------------------------------|------------------------------|
| 2592 x 1944 | 15 | 3 |
| 2048 x 1536 | 15 | 3 |
| 1920 x 1080 | 15 | 3 |
| 1600 x 1200 | 15 | 3 |
| 1280 x 1024 | 30 | 7.5 |
| 1280 x 720 | 30 | 7.5 |
| 1024 x 768 | 30 | 15 |
| 800 x 600 | 30 | 30 |
| 640 x 480 | 30 | 30 |
| 320 x 240 | 30 | 30 |

A second software tool was needed for capturing and saving frames from the camera. Several programs were tested, including FFmpeg³, fswebcam⁴, Gvvcview, uvccapture, VLC⁵, and GStreamer⁶ as command line tools. OpenCV⁷ was also tested as it is a popular library of programming functions mainly aimed at real-time computer vision. Initial development was done using OpenCV, but some problems were encountered when trying to configure the camera and synchronize processes.

With all of the command line tools being able to select an output format and resolution from the camera, capture frames, and save them as image files at a certain rate, the decisive factor for a final selection was performance.

GStreamer was selected as the best software tool because of its speed, low processing load, ease of use, and flexibility. But more importantly, as covered in section 2.1.5.3, GStreamer has the ability to interface with multiple cameras simultaneously, which was a feature of interest for further development along this project.

A series of shell scripts were assembled using v4l2-ctl for configuring the camera and GStreamer for capturing frames.

³<https://www.ffmpeg.org/>

⁴<http://www.sanslogic.co.uk/fswebcam/>

⁵<https://www.videolan.org/vlc/index.html>

⁶<https://gstreamer.freedesktop.org/>

⁷<https://opencv.org/>

4.1.3 Lens Testing - Modulation Transfer Function

A group of lenses with different focal lengths were tested to find the resolution efficiency for each. Due to the lack of a part number to identify them, an easy ID number was assigned to each. A first set of lenses (Lens ID 1-5) was acquired from the same China based manufacturer *ELP Ailipu Technology Co.* Lenses 1-4 did not have any pixel count specification whereas lens 5 was advertised as a megapixel lens rated for 5MP. Finally, one more lens (Lens ID 6) was acquired from the Germany based manufacturer *The Imaging Source*⁸. Lens 6 was also advertised as a megapixel lens rated for 5MP.

Lenses were tested following the ISO 12233 slanted-edge MTF method covered in section 2.1.4.3. The target shown in the same section (Figure 2.11) was printed with dimensions of 60x60 cm on a matte white sheet with 300ppi quality using a laser printer. The ELP-USB500W02M camera running at full resolution (2592x1944 pixels) with RAW (YUYV) output was used for taking the pictures. The camera was focused manually to the best focus possible. Pictures were taken, visually checked for focus, and processed using a software implementation of the ISO 12233 slanted-edge MTF method. The software was developed by Burns in the form of a MATLAB source code package called *sfrmat3: SFR analysis for digital cameras and scanners* [89]. Each image was processed at least twice and using different regions of interest in order to validate the results. As expected, the method is robust and stable, giving consistent results through repeated processing.

The distance from the camera to the target was set so that the target would fill the FOV. Table 4.4 shows the results of the tests. Lenses 1-4 showed a low resolution efficiency, with the lowest at 32% for lens 1, and the highest at 42% for lens 2. Lenses 5 and 6 showed a higher resolution efficiency, at 71% and 77% respectively.

Table 4.4: Results of different M12 lenses tested using the slanted-edge MTF method.

| Lens ID | Focal Length (mm) | Distance (cm) | Sampling Efficiency Vert. (%) | Sampling Efficiency Horiz. (%) | Resolution Efficiency (%) | Effective Resolution (MP) |
|---------|-------------------|---------------|-------------------------------|--------------------------------|---------------------------|---------------------------|
| 1 | 3.6 | 77 | 59 | 54 | 32 | 1.59 |
| 2 | 6.0 | 115 | 64 | 66 | 42 | 2.11 |
| 3 | 8.0 | 158 | 63 | 58 | 37 | 1.83 |
| 4 | 12.0 | 261 | 61 | 60 | 37 | 1.83 |
| 5 | 6.0 | 120 | 71 | 100 | 71 | 3.49 |
| 6 | 6.0 | 120 | 79 | 97 | 77 | 3.83 |

⁸<https://www.theimagingsource.com/>

Figure 4.2 shows the resulting MTF plots of lens 5 for the horizontal and vertical components. In both cases it can be seen that plots present an increase in sharpness, evidenced by the positive bump that takes the MTF above 1.0 before dropping. This effect is more evident in the horizontal component.

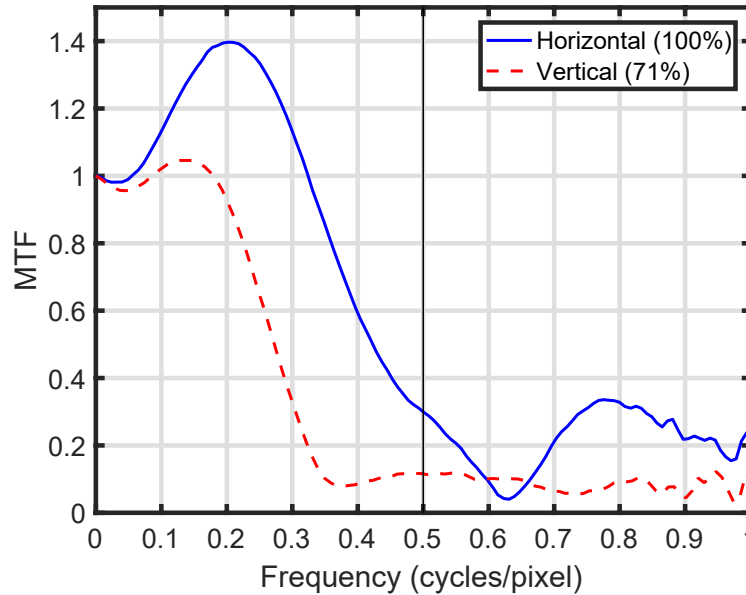


Figure 4.2: MTF plot for lens 5 (6mm focal length).

4.2 3-Band Multispectral Imaging System

A multispectral imaging system was developed using USB camera modules. Most basic multispectral imaging systems for vegetation and terrain analysis use 3-4 monochromatic cameras covering the Landsat Thematic Mapper bands TM2 (green), TM3 (red), and TM4 (NIR) as the most important bands, and adding the TM1 (blue-green) or the narrow red-edge bands as complementary.

Due to space constraints, a 3-band multispectral imaging system was designed, developed, installed on the Falcon I UAV (section 3.4) and flown. The system is based on three USB camera modules and optical filters. The cameras are connected to an ODROID SBC (section 3.2) via USB which takes care of controlling the cameras and saving frames into its local memory. The ODROID was also connected to the telemetry output of the autopilot board (section 3.1) to record avionics data stamps relevant for the images. Figure 4.3 shows the block diagrams of a camera subsystem and the complete imaging system.

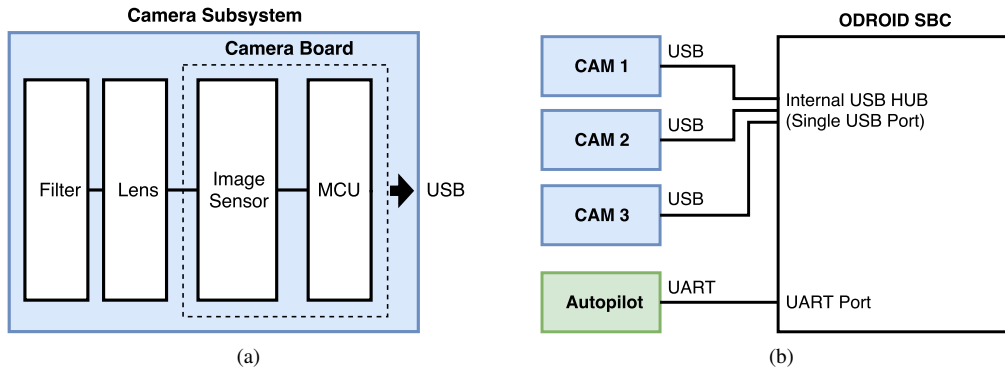


Figure 4.3: Simple block diagrams of a single camera (a), and the 3-band multispectral imaging system (b).

4.2.1 Cameras and Lenses

In section 2.2.3 a list of popular lightweight multispectral imaging systems currently in the market was presented. Based on an analysis of these systems, it was concluded that a resolution of 1.2 MP (1280x960 pixels) was appropriate and reasonable for achieving a good balance between image detail, directly translated into GSD, and amount of data. It is important to keep in mind that USB 2.0 has a theoretical maximum bandwidth of 480 Mbit/s or 60 MByte/s, and the more pixels a camera has, the more data will travel via the USB connection. The system must be able to capture images from all cameras simultaneously, therefore care must be taken in making sure not to exceed the USB 2.0 capacity. Camera ELP-USB130W01MT-B/W from *ELP Ailipu Technology Co.* was selected. Tables 4.5, 4.6, and 4.7 present the detailed features, settings, and output formats of this camera.

Table 4.5: Features of the ELP-USB130W01MT-B/W camera.

| | |
|--------------------|---------------------------|
| Manufacturer | ELP Ailipu Technology Co. |
| Part Number | ELP-USB130W01MT-B/W |
| Sensor | ON Semiconductor AR0130CS |
| Sensor Type | CMOS |
| Maximum Resolution | 1,280x960 pixels |
| Pixel Size | 3.75 μm |
| Image Area | 4,800 x 3,600 μm |
| Shutter | Rolling |
| Power Consumption | ~ 160 mA @ 5 VDC |
| Module Size | 38 x 38 mm |

Table 4.6: Settings of the ELP-USB130W01MT-B/W camera.

| Setting | Type | Min | Max | Step | Default |
|--------------------------------|---------|--------|-------|------|---------|
| Brightness | integer | -64 | 64 | 1 | 0 |
| Contrast | integer | 0 | 95 | 1 | 32 |
| Hue | integer | -2,000 | 2,000 | 1 | 0 |
| Saturation | integer | 0 | 128 | 1 | 0 |
| Sharpness | integer | 1 | 7 | 1 | 2 |
| Gamma | integer | 100 | 300 | 1 | 0 |
| White Balance Temperature Auto | bool | 0 | 1 | - | 1 |
| White Balance Temperature | integer | 2,800 | 6,500 | 1 | 4,600 |
| Backlight Compensation | integer | 0 | 3 | 1 | 1 |
| Gain | integer | 0 | 100 | 1 | 0 |
| PowerLine Freq. (Anti Flicker) | menu | 0 | 2 | - | 1 |
| Exposure Auto | menu | 0 | 3 | - | 3 |
| Exposure | integer | 1 | 5,000 | 1 | 625 |
| Exposure Priority | bool | 0 | 1 | - | 0 |

Table 4.7: Frame Rates for the ELP-USB130W01MT-B/W camera based on output video format and resolution.

| Resolution | Frame Rate @ MJPG | Frame Rate @ YUYV |
|------------|----------------------|----------------------|
| 1280 x 960 | 30/15 | 9 |
| 1280 x 720 | 30/15 | 10 |
| 800 x 600 | 30/15 | 20 |
| 640 x 480 | 30/15 | 30 |
| 320 x 240 | 30/15 | 30 |

With 1280x960 pixels and a pixel size of $3.75 \mu m$, the image sensor in this camera has the same resolution capabilities than the Sentek GEMS, Sentera QUAD, and Parrot Sequoia cameras (section 2.2.3). The major difference is that the ELP-USB130W01MT-B/W has a rolling shutter instead of a global shutter. This poses a challenge as imaging issues like skew or blur could be present in the final images under certain conditions. Another challenge is synchronizing multiple ELP-USB130W01MT-B/W cameras. Since there is no way of doing this via hardware, synchronization would have to be done through software.

It is important to take into consideration that this type of CMOS image sensor have a high quantum efficiency (measure of sensitivity of the photodiodes) in the visible wavelengths range (above 70%),

but it decays at higher wavelengths (Figure 4.4). Therefore, the NIR range will have a lower quantum efficiency that will have to be compensated with a longer exposure time or a higher gain.

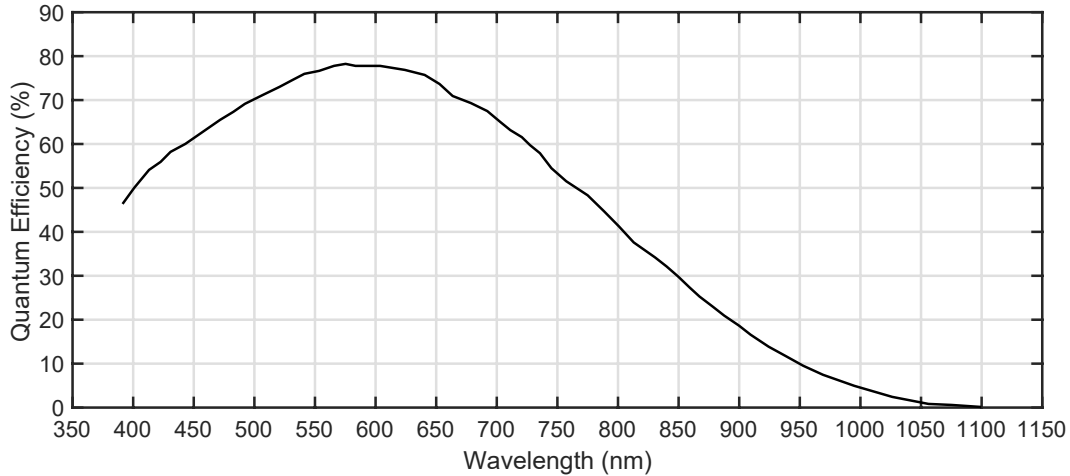


Figure 4.4: Quantum Efficiency of the Aptina / ON Semiconductor AR0130CS image sensor.

Lens 5 (6 mm focal length, 5 MP) was selected for the imaging system. The higher resolution efficiency (71%) gives better imaging performance. Going with 6 mm focal length results in a FOV of $43.60^\circ \times 33.39^\circ$ and a GSD of 7.5 cm @ 400 ft (~122m). Compared to values presented in table 2.4 (section 2.2.3) for commercial cameras, this configuration is close to the ones adopted by the Sentek GEMS, Sentera QUAD, and Parrot Sequoia cameras. The average between the focal lengths of these cameras gives 5.56 mm, close to the 6 mm focal length selected for our system. This selection offers a good balance between FOV and GSD.

4.2.2 Optical Filters

Filters for the imaging system were selected following the general convention of bands used in commercial multispectral cameras (section 2.2.3), which in turn is oriented towards the calculation of vegetation indices. Given that the system has three cameras, the green, red, and NIR bands were selected. Filters were acquired from Andover Corporation⁹. Table 4.8 and Figure 4.5 present the technical details and spectral response of the filters. Figure 4.6 shows a comparison of the bands chosen for this system and the bands used in other commercial multispectral imaging solutions.

⁹<https://www.andovercorp.com/>

Table 4.8: Technical details of the optical filters.

| Parameter | Green Band Filter | Red Band Filter | NIR Band Filter |
|------------------------|----------------------|--------------------|--------------------|
| Center Wavelength (nm) | 550 +10/-0 | 650 +10/-0 | 800 +10/-0 |
| Bandwidth (nm) | 40 +8/-8 | 40 +8/-8 | 40 +8/-8 |
| Transmission (%) | 50 | 50 | 50 |
| Size (mm) | 12.5 +0/- 0.25 | 12.5 +0/- 0.25 | 12.5 +0/- 0.25 |
| Thickness (mm) | 5.9 | 5.9 | 5.9 |
| Refractive Index | 2.05 | 2.05 | 2.05 |

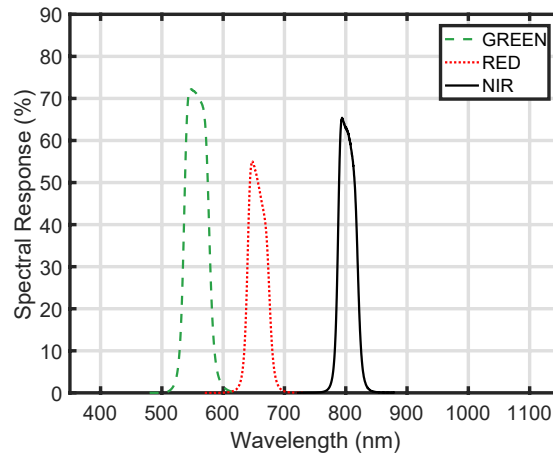


Figure 4.5: Spectral response or transmissivity of the green, red, and NIR band-pass filters chosen for the system.

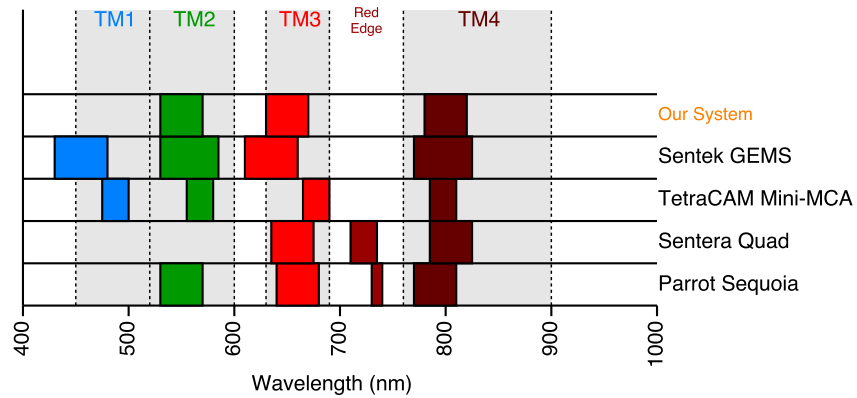


Figure 4.6: Comparison of chosen bands with bands used in other commercial multispectral cameras.

Filters came as discs of 12.5 mm of diameter. A small adapter was designed for holding the filter and fit on top of the lens as a cap (Figure 4.7). The adapter was 3D printed, the filter would fit tightly inside, and the whole cap would sit on top of the lens, secured by a screw.



Figure 4.7: From left to right; green, red, and NIR filters mounted on lens cap adapters.

Lens 5 comes with an IR cut filter glued to the back of the lens (Figure 4.8). This IR cut filter was removed from the lens where the NIR filter was installed, so as to be able to capture the desired band. The filter is a small glass disc with glue in three points. The filter was removed using a small sharp knife to cut through the points of glue.



Figure 4.8: Back of a lens with IR cut filter (left), and after IR cut filter removal (right).

4.2.3 Software Development

As previously mentioned in section 4.1.2, a series of shell scripts were created in order to interface with the camera. The scripts are based on v4l2-ctl for configuring the camera and Gstreamer for capturing frames. The v4l2-ctl configuration sets the values of the camera settings shown in table 4.6. Default settings were used with automatic exposure enabled.

After configuration, three identical pipelines were set up to run in parallel using Gstreamer. Each pipeline starts by opening a multimedia source, which in this case is a V4L2 source (camera). The

second step is to select the video output option. In this case, raw video (YUYV) with 1280x960 resolution and 9 fps frame rate was selected. The next step is to set the rate at which frames are going to be extracted from the source. A 1 fps frame rate was selected, which means that the source of 9 fps is downsampled to 1 fps. In other words, one frame is kept and 8 frames are skipped every second. The reason for selecting this frame rate depends on the conditions of the flights and is explained in more detailed in section 4.2.5. Final steps are to convert and encode the frame as a PNG file and save it in local memory. By using a *multifilesink* sink the pipeline will run in an endless loop. Figure 4.9 shows the diagram of the Gstreamer application.

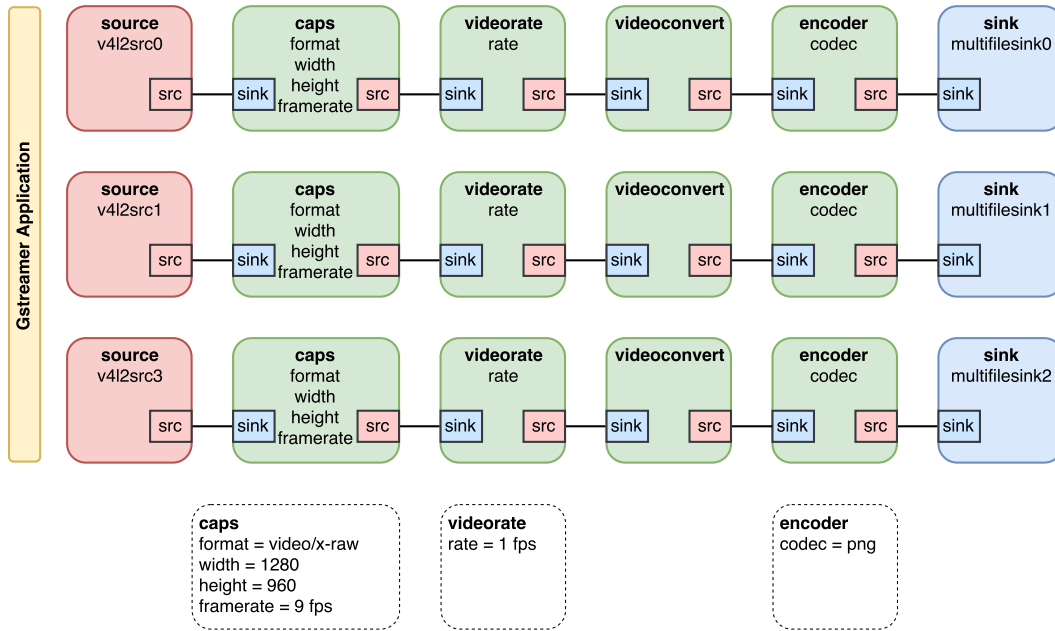


Figure 4.9: Diagram of the Gstreamer pipeline application for three ELP-USB130W01MT-B/W cameras.

While the above was the optimal configuration defined for the system, the software package was designed to keep settings in external configuration files that are given as input arguments to the main script. This way it is possible to define multiple configuration files with settings that are easy to change, thus making the overall software flexible.

Codecs JPEG, TIFF, and RAW were also tested for the encoder section. JPEG is a compressed format that leads to a faster processing and smaller file size, but by being compressed some information is lost. TIFF and RAW are complex lossless formats that keep all the information but take longer to process and lead to larger file sizes. PNG is a simple format that doesn't have most of the native features of TIFF or RAW while still being lossless and maintaining the image data. PNG was selected as the optimal format for being lossless and resulting in relatively small file sizes.

4.2.4 UAV Setup

In section 3.4.1 the interchangeable payload nose was introduced. This concept gives flexibility to the airframe design as multiple noses can be designed using the base model. The purpose of the noses is to hold the payload systems, which in this case is the cameras. A custom nose was designed to hold the three ELP-USB130W01MT-B/W cameras with filters attached. Given the space available in the nose base model, the cameras were arranged in three different levels (Figure 4.10). This arrangement introduces a distance difference of 13 mm between the sensor planes of each camera sensor, which is negligible given the intended range of working distances. The upside of this arrangement is that the optical centre of the cameras is closer to each other (29 mm), reducing the amount of misalignment between the cameras. Cameras are secured to the nose using screws and connected to the onboard ODROID SBC via USB cables. The figure shows how the location of the filters was assigned. The bottom part of the nose includes a transparent acrylic window that protects the cameras and preserves aerodynamics.

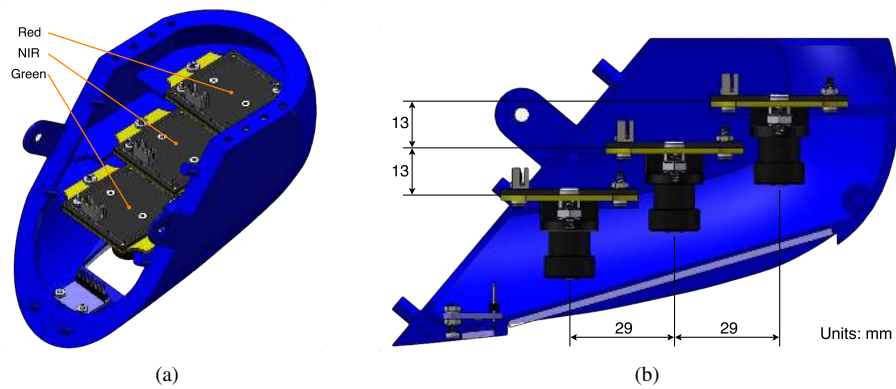


Figure 4.10: 3D model of custom plane nose with 3 cameras. (a) Isometric view. (b) Side cross-section view.

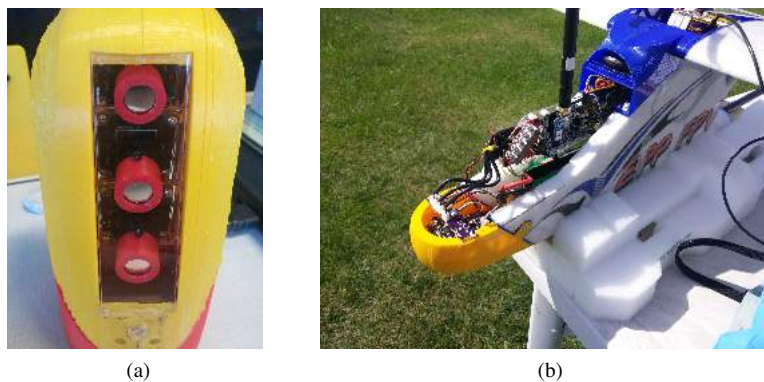


Figure 4.11: (a) Custom plane nose with 3 cameras and filters. (b) Nose installed in the plane.

The 3D printed custom nose with the 3 cameras, lenses, filters, and all the hardware has a total weight of 154 grams. This doesn't include the USB cables and ODROID computer that is necessary for interfacing with the cameras. Nonetheless, it is a relatively lightweight setup considering the use of 3 USB camera modules. The addition of this payload to the UAV does not increase the overall weight considerably and has a minor effect in the overall center of gravity.

4.2.5 Flight Campaigns

A series of flight campaigns were performed in order to test the system. Flights were performed at Bremner Field, a grass field in the North Saskatchewan River Valley, north of Sherwood Park, in Alberta, Canada. It is located in coordinates 53.6380961° , -113.2895888° , with an altitude of 610 m above sea level. This field offers north-south, east-west, and northwest-southeast runways with clear and unobstructed approaches from all directions. Bremner Field is managed by the Edmonton Radio Control Society (ERCS)¹⁰. Figure 4.12 shows a map of Bremner Field with the delimited area allowed for flight operations.



Figure 4.12: Map of Bremner Field indicating the delimited area for flight operations.

There was a total of four flights done with the 3-band multispectral imaging system on board of the Falcon I UAV. Table 4.9 presents the details of each flight. Flights 3 and 4 were divided in 2 and

¹⁰<https://www.ercs.ab.ca/>

3 segments respectively with different altitudes each. Actual speeds and altitudes are reported as averages in the table.

Table 4.9: Flight campaigns details.

| Flight | Date | Start Time | Duration (mm:ss) | Avg. Ground Speed (m/s) | Avg. Altitude (m) | Image Sets |
|---------------|-------------|-------------------|-------------------------|--------------------------------|--------------------------|-------------------|
| 1 | 2017-AUG-03 | 12:13:30 | 03:08 | 17 | 60 | 188 |
| 2 | 2017-AUG-03 | 12:32:20 | 08:13 | 17 | 100 | 493 |
| 3 | 2017-AUG-24 | 14:36:46 | 15:27 | 21 | 50 / 90 | 927 |
| 4 | 2017-SEP-15 | 12:34:13 | 19:49 | 18 | 60 / 80 / 100 | 1189 |

Flights involved manual take-off and landing, and a mix of assisted and autonomous flying. Assisted flying allows the pilot to control the direction and speed of the UAV but it limits the amount of roll, pitch, and yaw. Autonomous flight gives total control of the UAV to the onboard autopilot system, which executes a predefined flight plan. An operator in charge of the GCS monitors the behavior of the UAV at all times and manages the flight plan when in autonomous mode.

The imaging scripts were activated manually via terminal in the ODROID before taking off, and terminated in the same way after landing. Given the ground speed and altitude of the UAV, the image capture frequency was set to 1 frame per second. At this capture frequency there is a 33.33% overlap between two consecutive frames flying at 50 m AGL and 20 m/s ground speed, and a 66.67% overlap for 100 m AGL and the same speed. Cameras were used at maximum resolution (1280x960 pixels) and focus was set for a range of 50 - 100 meters, using the principle of hyperfocal distance, which is the the closest focusing distance that allows objects at infinity to be acceptably sharp. Under these conditions, images did not show any visible skew or blur during normal flight (take-off and landing excluded).

4.2.6 Image Alignment

Due to the use of multiple cameras and the fact that its optical centers are misaligned, the resulting images will also be misaligned. Alignment of the images is necessary in order to operate on them and obtain useful information like vegetation indices. In the UAV setup presented above the cameras are horizontally aligned (horizontal being the direction perpendicular to the direction of flight) but vertically misaligned (vertical being the direction of flight), with a distance between optical centers of 29 mm. This means that alignment of the images can be done operating only on one axis.

A MATLAB program was developed in order to run an alignment algorithm over the images. The algorithm takes the image from the middle camera (with the NIR filter) as the reference and aligns the other two (red and green) with respect to it. The algorithm is based on correlation between the images, where one image is the reference and the other is the subject.

The algorithm is based on the assumption that there is a single maxima in the pixel-by-pixel correlation between two misaligned images as one of the images is translated a certain amount of pixels in a certain direction. Since the images in this case are misaligned only in one axis, and the direction of misalignment is known, the problem is simplified as the algorithm runs only in one axis and one direction (1D translation). Figure 4.13 shows the correlation plot of two images as one them is kept fixed and the other is displaced. Displacement was done with 1 pixel increments with a range of 50 pixels. The maxima for this example occurs at 22 pixels, with a correlation of 0.84312. At this point, the two images have the highest correlation between them. If the pixel offset, 22 pixels in this case, is cropped from both images, one at the top and the other at the bottom, the result is two aligned images. The images used for this test were taken at approximately 60 meters away from the target. At larger working distances the misalignment is less and the offset in pixels will be less.

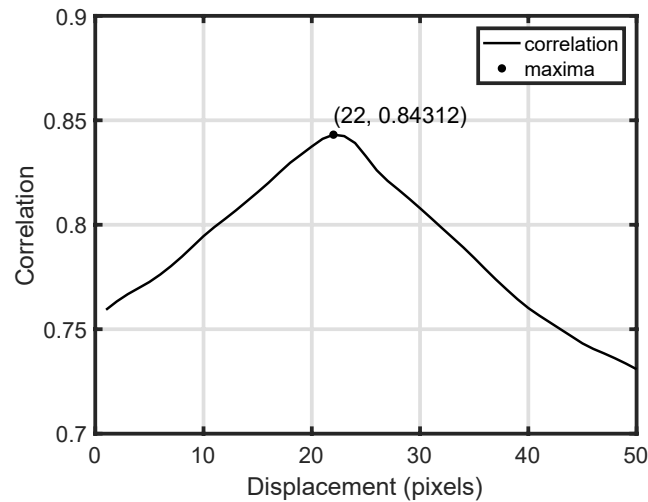


Figure 4.13: Correlation plot of alignment algorithm indicating maxima.

The process for aligning a set of three images uses the same principle. Two images are aligned first to produce a first aligned subset, then the third image is aligned with respect to this subset to produce the final set. In this case, the middle image and one of the side images is aligned first. After alignment and cropping, the new middle image is used as reference to align the other side image. Then, the offset from the first pair and the second pair is compared, taking the greater one and adjusting in order to make sure all three images have the same size. The final images will end up with a smaller height due to the cropping (Figure 4.14). The areas of the images, top and bottom, that are not present in all three images are discarded, leaving three images accurately aligned.

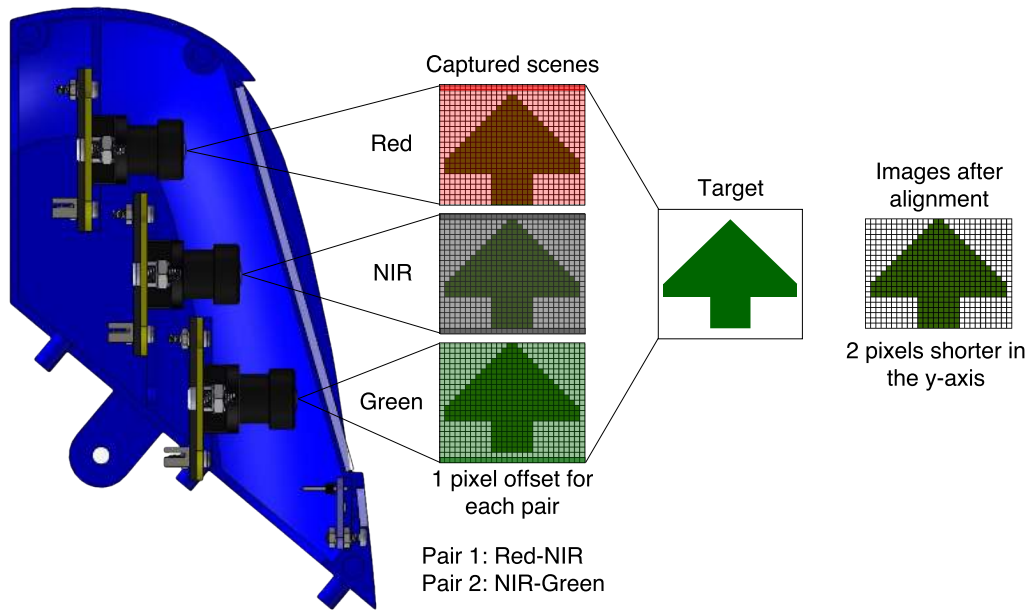


Figure 4.14: Example of pixel offset and cropping of images for alignment.

Figure 4.15 shows the example of three images (red, green, and NIR bands) superposed before and after alignment. In this example the misalignment between red and NIR band images was 19 pixel, and between NIR and green band images was 21 pixels.

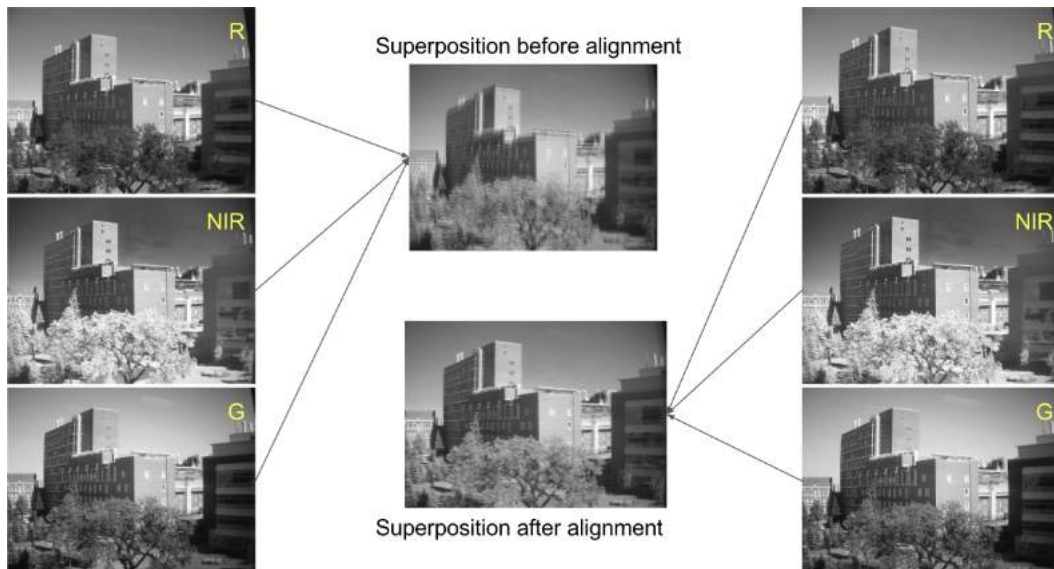


Figure 4.15: Superposition of red, green, and NIR band images before and after alignment.

Figure 4.16 shows a closer comparison of the superposed images before and after alignment.

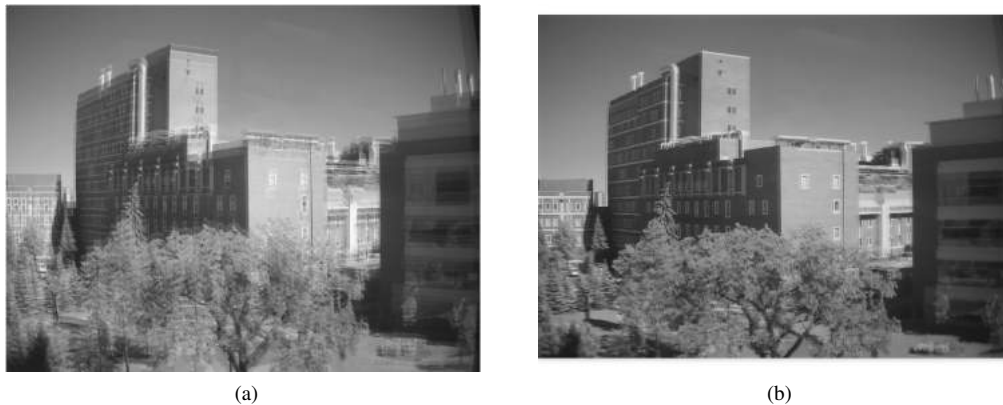


Figure 4.16: Result of image alignment algorithm. (a) Superposition before alignment. (b) Superposition after alignment.

While this method might seem simple compared to more advanced algorithms [90], it gives accurate results and takes less processing time. The algorithm was improved by making it exit the correlation comparison loop as soon as the maxima was found. It takes the algorithm an average of 1.79 seconds to align a set of three images taken at a working distance of 80 meters, where the misalignment is in average 19 pixels.

The resulting images after alignment end up being shorter in height as only common areas of the images are kept, the rest is removed. The final superposed image is clear and well defined. Since lens distortion was not corrected the alignment of pixels is not perfect, and some offset can be seen. The offset goes from zero at the center of the image and grows moving outwards. It is possible to see misaligned areas at the edges and corners of the superposed image. Nonetheless, the results are fast and accurate enough for basic pixel level operations in the images.

4.2.7 Vegetation Indices

After capturing images of the same scene using different spectral bands, and aligning the images, it was possible to operate over the images and calculate vegetation indices. Although there are several vegetation indices, the most widely used is the Normalized Difference Vegetation Index (NDVI), introduced in section 2.3.1. The NDVI is a simple numerical indicator used for analyzing remote sensing imagery and determine whether the target contains live green vegetation or not. NDVI images were calculated from NIR and red band images using equation 2.11 from section 2.3.1 on a pixel by pixel basis. Resulting images have a $[-1,1]$ range and are false colored in order to obtain a clear vegetation map.

Figure 4.17 shows a test performed with the 3-band multispectral imaging system presented in this work, using six leaves of the same family, each with different levels of stress, going from a perfectly healthy leaf to a dead leaf. The experiment was done using natural sunlight as the incident source.

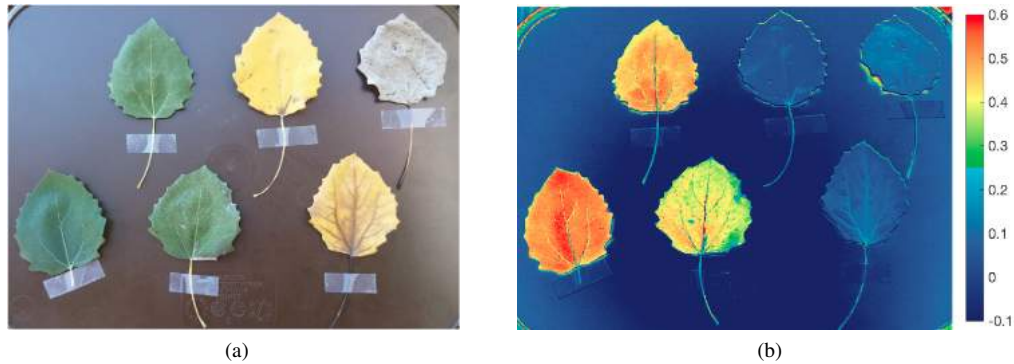


Figure 4.17: Example NDVI test of leaves with different levels of stress. (a) RGB image. (b) False colored NDVI image.

Classification within the range of NDVI values is important in order to correctly identify the areas of interest in the image. Barren areas of rock, sand, or snow have a low NDVI value (0.1 and below). Sparse vegetation like shrubs and grasslands show a moderate NDVI value (approximately 0.2 to 0.5). High NDVI values (approximately 0.6 to 0.9) correspond to dense vegetation commonly found in temperate and tropical forests or crops at their peak growth stage. Bare soil is represented with NDVI values that are closer to 0, and water bodies are represented with negative NDVI values [91]. Although these are general thresholds, in practice it is usually necessary to perform some real sample calibration to adjust the ranges for up to ± 0.1 .

In the experiment with the leaves, the color scale was adjusted for moderately healthy vegetation to start at an NDVI value of 0.25. It is evident in the image, as it is compared to the equivalent RGB image, that healthy leaves can be clearly differentiated from highly stressed (dry and dead) leaves. Furthermore, clear levels can be identified in the three healthy leaves on the NDVI image.

All the NDVI processing algorithm (calculation and false coloring) was done in MATLAB and packed in a single processing script. The same script was later used for processing the images of the flights after alignment. Figure 4.18 shows samples of NIR band, red band, and NDVI images of pictures captured from the UAV at Bremner Field. In this field, the main runways have live green grass that is regularly watered and in maintained conditions, whereas the surrounding sections of the runways have grass and bushes that live in natural conditions. The surrounding sections exhibit less green vegetation and higher levels of dryness to the eye. NDVI images show a clear differentiation between the maintained and apparently healthy live grass in one of the main runways and the surrounding not maintained grass.

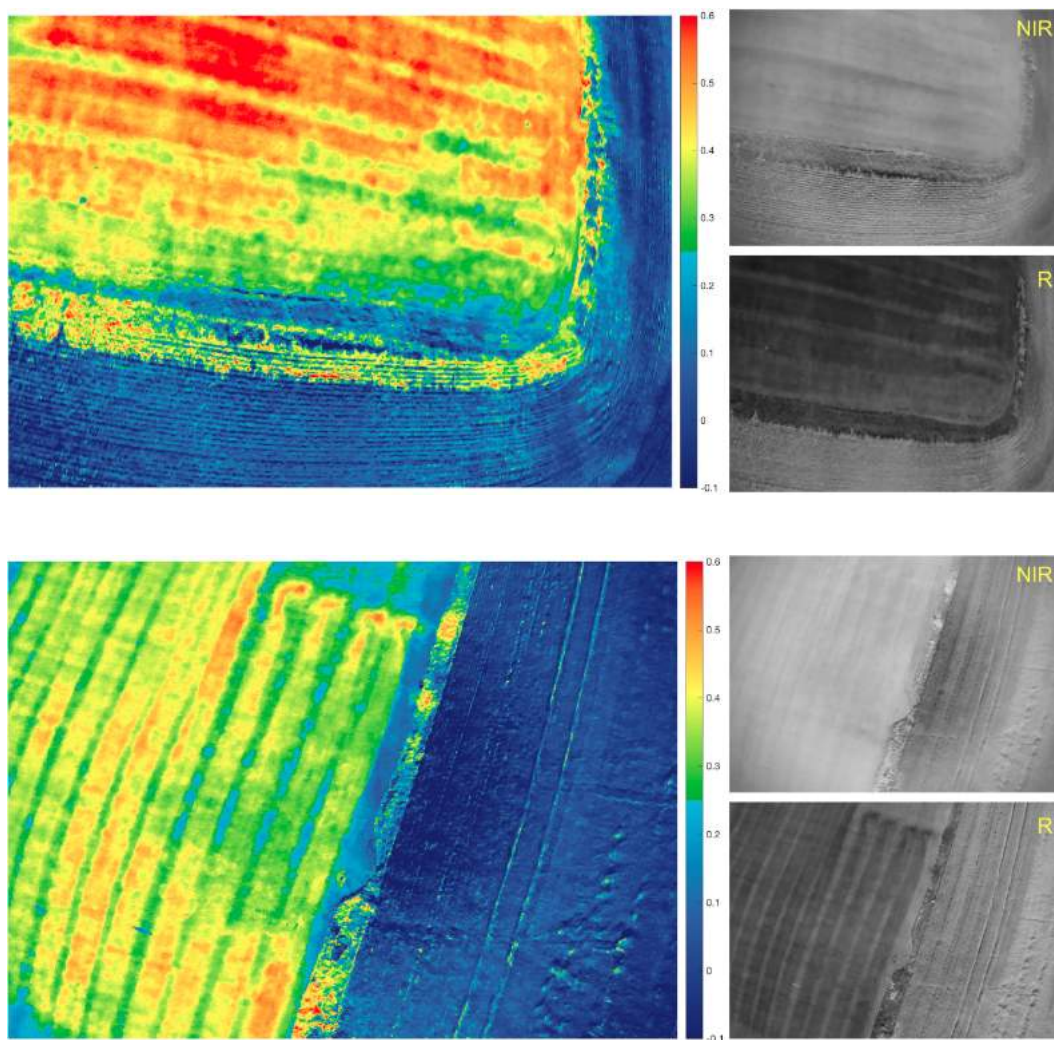


Figure 4.18: Sample pictures of a flights at Bremner Field showing the NIR and Red band images and the NDVI resulting image.

Chapter 5

12-Band Multispectral Imaging Platform

This chapter covers the design, development, and experiments carried out with the more advanced prototype of a 12-Band multispectral imaging system. The first section introduces the concept and key aspects of the system. The second section covers the USB camera modules chosen for the system, explaining the factors and reasons for its selection. Subsequently, the custom camera bridge board is introduced, covering the integrated and configurable USB HUB and automatic trigger circuits. Finally, results from testing are presented.

5.1 System Concept

The proposed system will follow the approach presented in the previous section. In this revision, the system is based on an array of up to 12 cameras with global shutter and synchronized trigger. The cameras continue to have a USB 2.0 interface, and will be connected to a custom designed PCB that will include USB HUBs to integrate USB routes and minimize cabling. The USB routes will be configurable to a degree to allow for grouping cameras depending on configuration and USB bandwidth requirements. The custom camera bridge board will also include a triggering circuit for the cameras based on a microcontroller unit (MCU).

The goal is to create and test an integrated multi-camera system based on USB camera modules that is flexible and configurable, so that it can be used with optical filters as a development platform for multispectral imaging applications.

5.2 USB Camera Modules

The imaging system was designed to work with the DMM 42BUC03-ML USB 2.0 board-level camera from the manufacturer The Imaging Source, LLC¹. Selection of this camera was made based on a balance between size, cost, and capabilities. The requirements were set for a camera with global shutter and trigger as the main specifications. The usual maximum resolution for global shutter sensors is 1.2 Megapixels. The use of S-Mount lenses and no packaging or enclosure reduces the costs, and the size was selected as the minimum possible to allow for miniaturization and light weight. The DMM 42BUC03-ML (Figure 5.1) is a small 30 mm x 30 mm monochromatic board-level camera module with S-Mount (M12) lens based on the ON Semiconductor AR0134CS CMOS image sensor. This sensor comes with a global shutter [92], which is ideal for imaging a target or scene in movement as it does not suffer from imaging issues associated with rolling shutter such as skew and wobble [93]. Table 5.1 summarizes the technical specifications of this camera.



Figure 5.1: DMM 42BUC03-ML camera module from The Imaging Source, including S-Mount lens holder and lens.

Table 5.1: Specifications of the DMM 42BUC03-ML camera.

| | |
|--------------------|-----------------------------|
| Manufacturer | The Imaging Source |
| Part Number | DMM 42BUC03-ML |
| Sensor | ON Semiconductor AR0134CS |
| Sensor Type | CMOS |
| Maximum Resolution | 1,280 x 960 pixels |
| Pixel Size | 3.75 μm |
| Image Area | 4,800 x 3,600 μm |
| Shutter | Global |
| Power Consumption | ~ 250 mA @ 5 VDC |
| Module Size | 30 x 30 mm |

¹<https://www.theimagingsource.com/>

The ON Semiconductor AR0134CS has 1.2 Megapixels (1,280 x 960 pixels) and a pixel size of $3.75 \mu\text{m}$, which makes it equivalent to the image sensors used in the Parrot Sequoia, MicaSense RedEdge-M, Sentera QUAD, and Sentek Systems GEMS Multispectral Sensor. The quantum efficiency (measure of the sensitivity of the photodiodes) of this sensor (Figure 5.2) is also very similar to the ones reported for the commercial cameras.

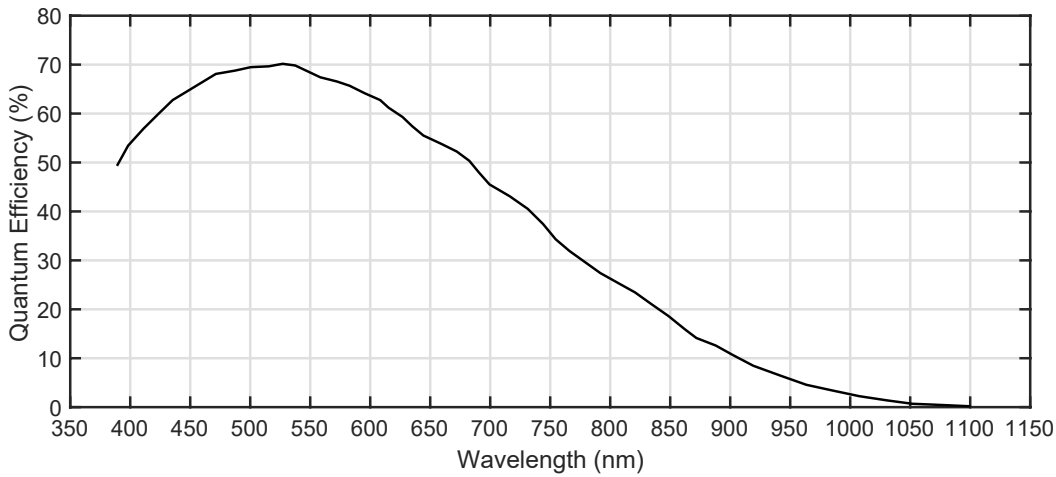


Figure 5.2: Quantum efficiency of the ON Semiconductor AR0134CS image sensor.

The DMM 42BUC03-ML camera also features a working mode based on an external trigger input. When a trigger signal, defined as a positive pulse of at least 10 microseconds, is received by the camera in the trigger input pin, the camera will start the exposure and readout process of a single frame (Figure 5.3). The length of the exposure can be set by software. The duration of the image readout is the reciprocal of the current frame rate. After image readout is finished, the camera is able to accept another trigger. It is possible use this feature to send the same trigger signal to multiple cameras and have them synchronized. The trigger input on the camera is opto-coupled and admits positive trigger pulses with any amplitude between 3.3V and 12V.

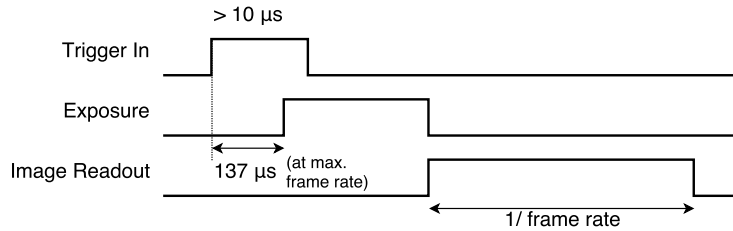


Figure 5.3: Timing diagram of the trigger, exposure, and image readout processes.

This camera has a monochromatic raw output video format (Y800) and can operate at three different

resolution options, with several frame rate options for each resolution (Table 5.2). When selecting a lower resolution, contrary to pixel binning [94], the DMM 42BUC03-ML will only read the corresponding amount of pixels referenced to the top left corner of the sensor. Therefore, lowering the resolution reduces image data and USB bandwidth requirements, which makes possible for more cameras to share the USB resource.

Table 5.2: Video formats and frame rates available in the DMM 42BUC03-ML camera.

| Resolution | Frame Rate @ GREY (Y800) |
|------------|-----------------------------|
| 1280 x 960 | 30 / 25 / 15 / 10 |
| 640 x 480 | 60 / 30 / 25 / 15 |
| 320 x 240 | 60 / 30 / 25 / 15 |

The USB interface in this camera is compatible with the USB Video Class (UVC) standard driver. This camera offers a range of settings that are accessible and configurable via software (Table 5.3). The “Privacy” value is the trigger enable/disable setting. When disabled the camera is in free running mode. When enabled the camera is in trigger mode.

Table 5.3: Settings of the DMM 42BUC03-ML camera.

| Setting | Type | Min | Max | Step | Default |
|------------|---------|-----|---------|------|---------|
| Brightness | integer | 0 | 255 | 1 | 12 |
| Gain | integer | 34 | 255 | 1 | 36 |
| Exposure | integer | 1 | 300,000 | 1 | 127 |
| Privacy | bool | 0 | 1 | - | 0 |

5.2.1 Optical Filters

The use of S-Mount (M12) lenses in these camera modules allow the use of optical filters with the same approach presented in section 4.2.2. The 12.5 mm of diameter filter discs are easily installed in the lenses using a small 3D printed adapter piece that holds the filter and fits in front of the lens, secured by a screw (Figure 5.4).

5.3 Camera Bridge Board

The camera bridge board (Figure 5.5) acts as a motherboard for the camera modules and is the main integration unit of the system. Cameras connect directly to the bridge board, which routes all

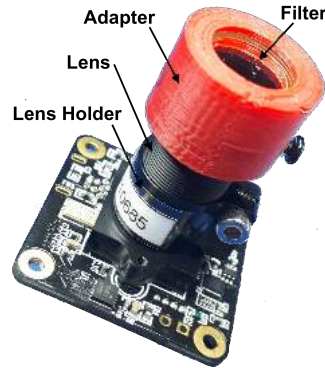


Figure 5.4: Camera board with S-Mount (M12) lens and optical filter installed using the 3D printed adapter.

USB communications via USB HUBs into selectable upstream USB ports. This board includes a step-down voltage regulator that provides power to all components including the cameras. It also integrates a microcontroller unit (MCU) that generates the pulses used for triggering the cameras.

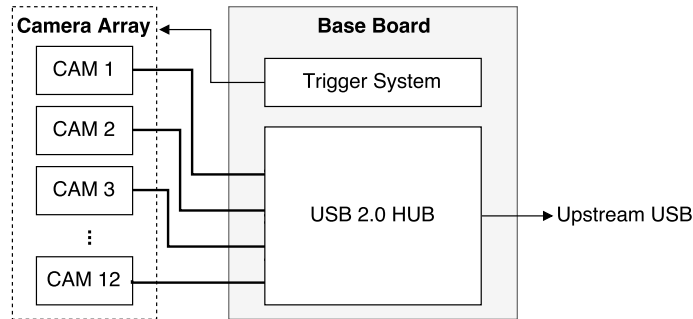


Figure 5.5: Diagram of the basic connections between the camera array and the bridge board. The bridge board routes all USB communications into selectable upstream ports and sends trigger signals to the cameras.

The goal was to design a compact system, and avoid the use of USB cables as they tend to be bulky and take up considerable space and mass. The bridge board was designed to have straight mini USB plug connectors that match the mini USB receptacle connectors found in the DMM 42BUC03-ML camera modules. The trigger input pins of the camera modules are found in a picoblade connector. The bridge board has cutouts underneath of each camera location, and individual trigger connectors on the other side of the board. Mounting holes are also included for securing the cameras to the bridge board using standoffs.

The bridge board Printed Circuit Board (PCB) was designed using the PCB CAD tool Altium Designer. Schematics and Bill-of-Materials of the camera bridge board can be found in Appendices B and C. Figure 5.6 shows a layout view of the board with the top and bottom layers.

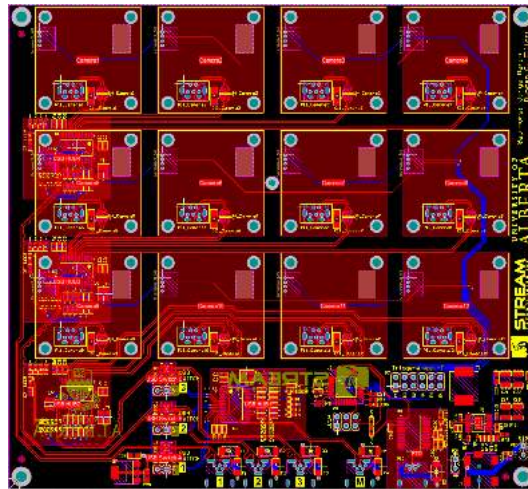


Figure 5.6: Altium Designer layout view of the bridge board with top layer (red), bottom layer (blue), and silkscreen (yellow).

The PCB is a 4-layer board. External layers are used for routing signals and internal layers are planes. Layer 1 (top) contains most of the components and USB routing. Layer 2 is a ground plane that provides reference for the USB differential pairs so as to keep the desired impedance. Layer 3 is a power plane, and layer 4 (bottom) contains the trigger connectors and additional routing. The bridge board alone weighs 95 grams, and is 150 mm long by 138 mm wide. Figure 5.7 shows a CAD 3D model of the bridge board.

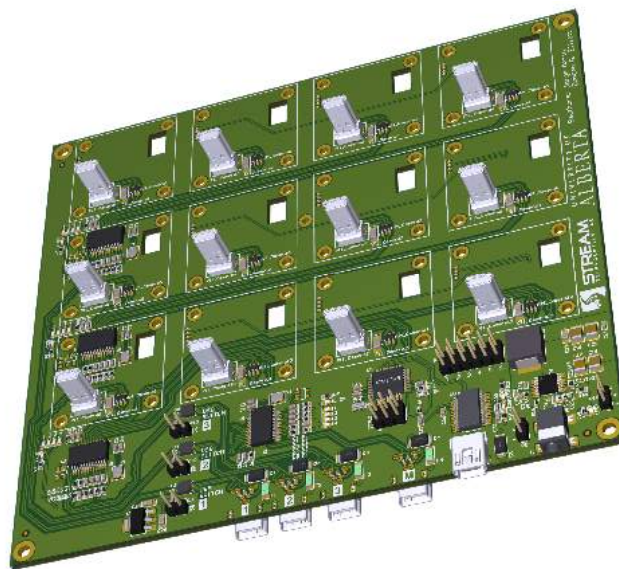


Figure 5.7: CAD 3D model of the bridge board.

It is important to note that the bridge board itself is a USB 2.0 multi-camera platform that can be modified and adapted to work with a wide range of cameras. While this board was designed for the use of the DMM 42BUC03-ML camera modules, it is perfectly possible to connect other cameras. The Imaging Source provides other USB 2.0 board-level camera modules with different features but keeping the same form factor. Therefore it is possible to replace the selected DMM 42BUC03-ML camera module with other cameras from the same manufacturer and still be able to utilize the direct connection to the mini USB connector, mounting holes, and trigger connection. Alternatively, it is also possible to use any other camera module as long as it communicates via USB 2.0. Additional cables might be needed to complete the USB and trigger connections between the cameras and the bridge board, and extra work might be required for attaching the cameras.

The bridge board provides all necessary electronics for the connection of multiple USB 2.0 cameras to different upstream USB ports via configurable USB HUBs. It also provides a configurable trigger system handled by a reprogrammable MCU. The following sections cover in detail specific features of the bridge board.

5.3.1 USB HUB

A configurable USB 2.0 HUB in the board allows for the connection of up to 12 USB 2.0 camera modules (Figure 5.8). The cameras are organized in groups of four, going through a first level of USB HUBs and then USB switches that offer two different routing options. The first option is a second level USB HUB that connects all cameras to a master USB upstream port. The second option is to route each group to its dedicated USB upstream port. The USB switches are controlled with user selectable jumpers. The flexibility of this approach allows the user to choose between isolating and merging USB communications depending on the USB bandwidth requirements.

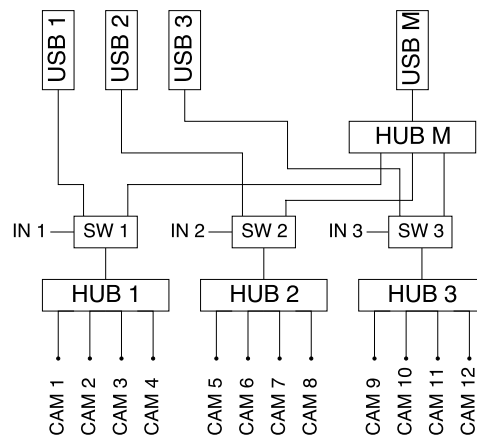


Figure 5.8: Diagram of the configurable USB HUB network. SW 1, SW 2, and SW 3 are 2-to-1 bidirectional USB 2.0 switches with inputs controlled by user selectable jumpers. USB 1, USB 2, USB 3, are the isolated upstream ports, and USB M is the master upstream USB port.

By isolating a first layer HUB we end up with an independent group of 4 cameras routed to an upstream mini USB port (USB 1, 2, 3). A lower number of cameras reduces the load and bandwidth requirements on a USB port. This setup is used for cameras that require a high USB bandwidth. Alternatively, when using cameras with a lower USB bandwidth requirement, it is possible to merge some or all USB communication in the bridge board into a single USB port (USB M). This approach simplifies the connection of the bridge board to an external computer.

5.3.2 Trigger

The bridge board includes a trigger system based on a microcontroller unit (MCU). The MCU is an 8-bit 16Mhz ATMEGA328P-AU compatible with the Arduino framework and development environment [95, 96]. The MCU uses general purpose input/output (GPIO) pins to generate the pulses that trigger the cameras. A total of 6 GPIO pins from the same MCU port are used, and each pin connects to a group of 2 cameras. By having 6 independent trigger pins it is possible to define custom triggering sequences for each pair of cameras. Conversely, by having the 6 pins from the same MCU port it is possible to trigger all of them at the same time, thus allowing accurate synchronization of all cameras. Trigger signals go through a jumper section in the board, allowing the user to break the connection between the MCU and the cameras. By means of this it is possible to connect the MCU pins to a different location, and/or connect trigger signals from an external system. This approach brings more flexibility to the design, making it easy to modify according to the requirements. Figure 5.9 shows a diagram of the trigger system.

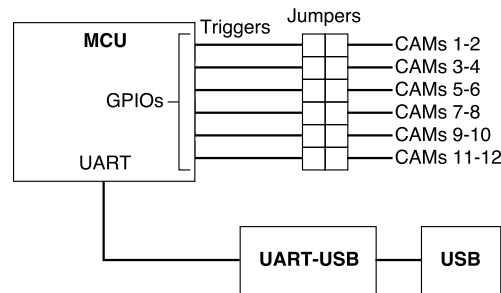


Figure 5.9: Diagram of the trigger system based on a microcontroller unit (MCU). Trigger signals are generated via GPIOs. A UART connection via USB is provided for interactively interfacing with the MCU via serial commands.

The MCU is also connected via UART to a UART-to-USB transceiver, which in turn connects to a USB connector. This addition provides an easy way to flash the MCU as long as the corresponding bootloader is on. More importantly, this connection provides a way to communicate interactively with the MCU via USB serial. A set of commands has been defined in the default MCU program to make it possible to change some settings of the trigger system on the go, without needing to modify

the program and re-flash it. Features like changing the period of the automatic trigger, start or stop the automatic trigger, send trigger signals based on a command, are included in the MCU program and can be controlled via serial commands. The ability to have multiple functions and modes of operation of the trigger system integrated in the same program makes it easy, flexible, and versatile.

5.4 Software

Similar to the previous imaging system (Chapter 4), a software package was developed for interfacing with the imaging system. The core of the software remained in the two elements: The Video for Linux Two (V4L2) API, used to interface with the lower-level UVC driver, and GStreamer, used for simultaneous interface with multiple cameras.

Similarly, the software package is based on a collection of shell scripts that take care of configuring the cameras and building the acquisition, processing, and storing pipelines for each camera. The script runs according to settings specified in a configuration file that is given to the script as an argument. A series of external configuration files keep different variants of the system and allow for customization of the program.

The trigger system MCU runs a program written in C++. The program sends simultaneous pulses to all cameras periodically. The triggering period is set to 1 second by default. This value is loaded from the MCU EEPROM. The program also has a serial terminal-like interface that accepts custom defined AT commands. The commands allow to stop and restart the periodic trigger, change the triggering period (any new value is saved in the EEPROM), and send a single trigger.

5.5 Testing

An experiment was designed to test the system in the lab with different configurations of the cameras, and determine the effect in the USB traffic load, as well as the maximum number of cameras that can work simultaneously for a given configuration. The platform was tested with DMM 42BUC03-ML camera modules synchronized using the trigger system. The system was connected using a single upstream USB port to an external computer running Linux. USB traffic was analyzed using a sniffing tool called Wireshark² [97]. Resolution, Frame rate, and the number of simultaneous cameras were the controlled variables. The total throughput in the USB 2.0 channel was monitored. Table 5.4 summarizes the scenarios that successfully worked with images captured simultaneously from all cameras and saved locally.

Images from the DMM 42BUC03-ML are transmitted over USB in chunks (packets) of 16,448 bytes. First, the host (computer) sends a packet request, and then the peripheral (camera) sends the

²<https://www.wireshark.org/>

Table 5.4: Test results of USB traffic with different configurations. Cameras were connected to a single USB upstream port and triggered simultaneously. Data transferred based on a single frame from each camera.

| Test # | Resolution | Frame Rate (fps) | # Cam | Data Transferred (Bytes) | Throughput (MB/s) |
|--------|------------|------------------------|----------|--------------------------------|----------------------|
| 1 | 1280 x 960 | 30 | 1 | 1,238,530 | 38.98 |
| 2 | 1280 x 960 | 10 | 1 | 1,238,530 | 12.93 |
| 3 | 1280 x 960 | 10 | 2 | 2,477,060 | 25.90 |
| 4 | 1280 x 960 | 10 | 3 | 3,715,590 | 38.95 |
| 5 | 640 x 480 | 30 | 2 | 619,268 | 20.87 |
| 6 | 640 x 480 | 15 | 2 | 619,268 | 10.43 |
| 7 | 640 x 480 | 15 | 4 | 1,238,536 | 20.87 |
| 8 | 640 x 480 | 15 | 8 | 2,477,072 | 41.61 |
| 9 | 320 x 240 | 15 | 8 | 619,280 | 10.32 |
| 10 | 320 x 240 | 15 | 12 | 928,920 | 15.51 |
| 11 | 320 x 240 | 30 | 12 | 928,920 | 29.44 |

response packet (includes overhead and payload). This process continues until the whole frame has been transferred. The total data transferred reported in Table 5.4 takes into accounts all traffic, which includes request packets and response data packets. As mentioned before, the maximum throughput in practice for USB 2.0 is around 40 MB/s. Tests 1, 4, and 8 have working configurations at the limit of the USB bandwidth capacity. Adding an additional camera to these configurations would exceed the USB 2.0 bandwidth and would result in dropped packets representing permanently lost fractions of camera frames.

It is evident that decreasing the resolution leads to less data being transferred, and lowering the frame rate gives more time for data to transfer. Both of these conditions cause the throughput to decrease and allow the connection of more cameras. The resolution and frame rate settings define the maximum number of cameras that can work at the same time.

Based on the results of these tests it is possible to estimate the maximum number of cameras that can work simultaneously with a certain configuration. The estimation uses the maximum practical USB bandwidth of the system and an estimate of the total throughput.

$$Max \# Cameras = \frac{USB \ BW}{Throughput} \quad (5.1)$$

The USB BW is set to 40×10^6 Bytes/s, and the Throughput is given by

$$Throughput = \frac{Data\ Frame}{Transfer\ Time} \quad (5.2)$$

$$Data\ Frame = SF \times (Width \times Height) \quad (5.3)$$

$$Transfer\ Time = \frac{1}{Frame\ rate} \quad (5.4)$$

Since the Y800 format used by the cameras assigns one byte per pixel, Data Frame is estimated as the total number of bytes required by the image, multiplied by a scaling factor ($SF = 1.01$) to account for the response packets overhead and request packets. This scaling factor was calculated from the size of the request packets, response packets, and response packets overhead. Each request packet is 64 bytes, and each response packet is 16,448 bytes out of which 100 bytes are overhead and the rest is payload. The scaling factor is the ratio of the total number of bytes exchanged via USB to the actual number of payload bytes ($16,512 / 16,348 = 1.01$). The transfer time is equivalent to the readout time, which is the reciprocal of the frame rate. After substituting (5.2), (5.3), and (5.4) in (5.1) we get

$$Max\ \# \quad Cameras = \frac{USB\ BW}{SF \times Width \times Height \times Frame\ rate} \quad (5.5)$$

The integer part of this number gives an accurate estimation of the maximum number of cameras that can work simultaneously for a certain resolution and frame rate.

The final system, shown in Figure 5.10, has been successfully tested with an ODROID C2 single board computer (SBC). Given the low CPU load of the software, it can run with no issues in many relatively cheap SBCs. The imaging board is 150 mm long by 138 mm wide, and 43 mm tall considering the camera modules and lenses. Although the size and focus point of the lenses will affect the overall height. The board weights 323 grams with 12 DMM 42BUC03-ML cameras, standoffs, and fasteners.

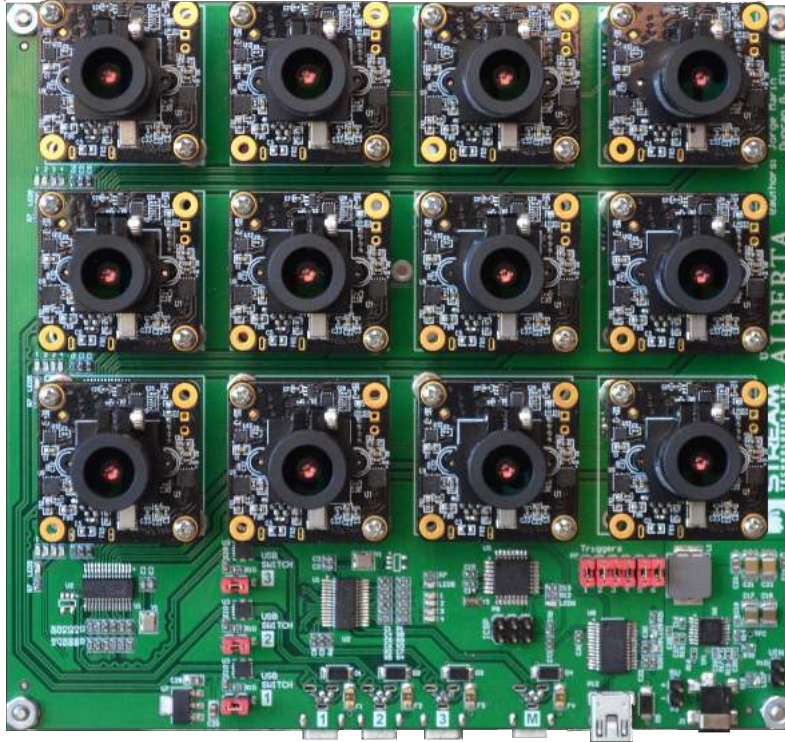


Figure 5.10: Multispectral imaging system hardware with 12 cameras installed.

Finally, table 5.5 shows an extension of table 2.4 presented previously in section 2.2.3, with the addition of the 12-band multispectral imaging system presented in this section for comparison.

Table 5.5: Comparison of common multispectral imaging systems with the system presented in this work.

| Camera | This Work | Tetracam ADC Micro | Tetracam Mini-MCA4 | Sentek GEMS | Sentera QUAD | Parrot Sequoia |
|------------------------------|----------------|-----------------------|-----------------------|----------------|-----------------|-------------------|
| Dimensions (mm) | 150 x 138 x 43 | 75 x 59 x 33 | 131 x 78 x 87 | 127 x 89 | 76 x 62 x 48 | 59 x 41 x 28 |
| Weight (g) | 323 | 90 | 600 | 320 | 170 | 72 |
| Number of Bands | 12 | 4 | 4 | 4 | 4 | 4 |
| Focal Length (mm) | 6.00 | 8.43 | 9.6 | 7.7 | 5.0 | 3.98 |
| FOV (H° x V°) | 43.6 x 33.4 | 37.6 x 28.7 | 38.2 x 30.9 | 34.6 x 26.3 | 51.2 x 39.6 | 61.9 x 48.5 |
| Sensor size (mm) | 4.8 x 3.6 | 6.55 x 4.92 | 6.66 x 5.32 | 4.8 x 3.6 | 4.8 x 3.6 | 4.8 x 3.6 |
| Resolution (pixels) | 1280 x 960 | 2048 x 1536 | 1280 x 1024 | 1280 x 960 | 1280 x 960 | 1280 x 960 |
| Pixel size (μm) | 3.75 | 3.12 | 5.2 | 3.75 | 3.75 | 3.75 |
| GSD (cm) @ 120m | 7.5 | 4.6 | 6.6 | 5.1 | 9.1 | 11.0 |
| Price (USD) | See Table 5.6 | 2,995.00 | 9,995.00 | 3,500.00 | 4,599.00 | 3,500.00 |

5.6 Costs

Tables 5.6 presents a list of general costs for different configurations of the multispectral imaging system hardware. Table 5.7 presents the costs per unit or set for the Bridge Board bare PCB and BOM based on order quantity. All prices are in US Dollars (USD).

Table 5.6: General costs of components for the multispectral imaging system hardware.

| Components | | 3 bands @ 1.2MP | | 8 bands @ 0.3 MP | | 9 bands @ 1.2MP | | 12 bands @ 0.3MP | |
|-----------------------|--------|--------------------|--------|---------------------|----------|--------------------|----------|---------------------|----------|
| Item | Cost | Qty. | Cost | Qty. | Cost | Qty. | Cost | Qty. | Cost |
| Bridge board bare PCB | 25.80 | 1 | 25.80 | 1 | 25.80 | 1 | 25.80 | 1 | 25.80 |
| Bridge board BOM | 47.94 | 1 | 47.94 | 1 | 47.94 | 1 | 47.94 | 1 | 47.94 |
| Camera | 289.00 | 3 | 867.00 | 8 | 2,312.00 | 9 | 2,601.00 | 12 | 3,468.00 |
| Lens holder | 16.80 | 3 | 50.40 | 8 | 134.40 | 9 | 151.20 | 12 | 201.60 |
| Lens | 6.00 | 3 | 18.00 | 8 | 24.00 | 9 | 27.00 | 12 | 72.00 |
| Optical filter | 56.00 | 3 | 168.00 | 8 | 448.00 | 9 | 504.00 | 12 | 672.00 |
| ODROID | 46.00 | 1 | 46.00 | 1 | 46.00 | 3 | 138.00 | 2 | 92.00 |
| Miscellaneous (*) | 10.00 | 3 | 30.00 | 8 | 80.00 | 9 | 90.00 | 12 | 80.00 |
| TOTAL | | 1,253.14 | | 3,118.14 | | 3,584.94 | | 4,659.34 | |

(*) fasteners, standoffs, connectors, cables, etc.

Table 5.7: Costs per set/unit based on order quantity for Bridge Board bare PCB and BOM.

| Item | Cost per set/unit @ Qty = 1 | Cost per set/unit @ Qty = 10 | Cost per set/unit @ Qty = 100 |
|-----------------------|--------------------------------|---------------------------------|----------------------------------|
| Bridge board bare PCB | 25.80 | 25.80 | 15.20 |
| Bridge board BOM | 47.94 | 39.71 | 31.35 |

The costs presented in the tables above does not account for full PCB assembly (PCBA). Nonetheless, compared to the prices of commercial cameras presented in table 5.5, a 3-band multispectral imaging system can be built using the approach and design presented in this thesis for a total costs that is less than half the price of the cheapest camera (2,995.00).

5.7 Focusing

A fundamental setting of this flexible imaging system is the possibility of changing lenses and focusing at different distances. But focusing at a certain distance can be a challenge when working with multiple cameras. Since each camera has to be manually focused individually, it is important to achieve the best possible focus for all the cameras. A custom software was developed for providing a live stream of the camera capture and quantify focus, so as to provide a metric that could be used for achieving the best possible focus for a given target.

Pertuz et al. [98] presented an analysis and comparison of focus measure operators. They concluded that the Laplacian-based operators presented the best overall performance for normal imaging conditions (i.e., without addition of noise, contrast reduction or image saturation). While all the operators present different strengths and weaknesses, and they can perform differently depending on the application, the Laplacian-based operators provide a good balance between speed and robustness.

The variance of Laplacian operator [99] was chosen for its mathematical simplicity, fast computational speed, and it gave consistent and precise results during testing with the image stream from the cameras. The variance of Laplacian is based on the use of a second derivative operator that allows the passing of high spatial frequencies which are associated with sharp edges. The second derivative operator used in this method is the Laplacian operator, which can be approximated using the mask

$$L = \begin{pmatrix} 0 & 1 & 0 \\ 1 & -4 & 1 \\ 0 & 1 & 0 \end{pmatrix} \quad (5.6)$$

The above is a positive Laplacian operator mask in which center element of the mask should be negative and corner elements of mask should be zero. This mask is used to take out outward edges in an image. The convolution of a grayscale image with this mask highlights gray level discontinuities in an image. The result of this operation is an image with grayish edge lines and other discontinuities on a dark background. Figure 5.11 shows a comparison of a sample image before and after applying the positive Laplacian operator.



Figure 5.11: Example of a sample gray scale image (left) after applying the positive Laplacian operator (right).

The focus metric calculates the variance of the absolute values, which leads to the focus measure given by

$$LAP_VAR(I) = \sum_m^M \sum_n^N (|\Delta I(m,n)| - \overline{\Delta I})^2 \quad (5.7)$$

where $\Delta I(m,n)$ is the convolution of the input image $I(m,n)$ with the mask L and $\overline{\Delta I}$ is the mean of absolute values given by

$$\overline{\Delta I} = \frac{1}{NM} \sum_m^M \sum_n^N |\Delta I(m,n)| \quad (5.8)$$

Figure 5.12 shows a graph of the focus measure of a camera as the focus distance is adjusted by bringing the lens closer, going from out of focus (too far) to out of focus (too close), passing through the point of best focus (in-focus). Three points are highlighted in the graph: two random points in the out of focus regions (too far and too close), and the in-focus point which is the maxima in the graph. Figure 5.13 shows the three reference images that correspond to the highlighted points in the graph.

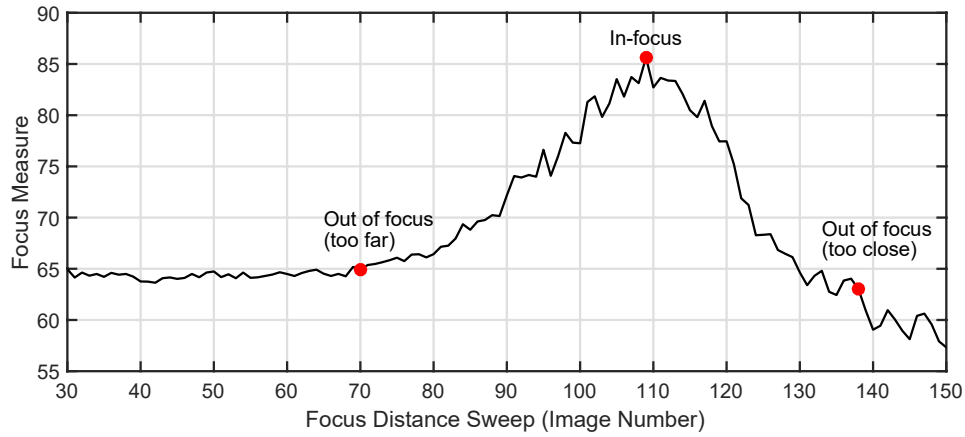


Figure 5.12: Graph of the focus measure calculated using the above algorithm as the focus is adjusted from out of focus (too far) to out of focus (too close), passing through the in-focus point. Any point outside the in-focus point is out of focus. The graph highlights two random out of focus points for reference, one too far and one too close.

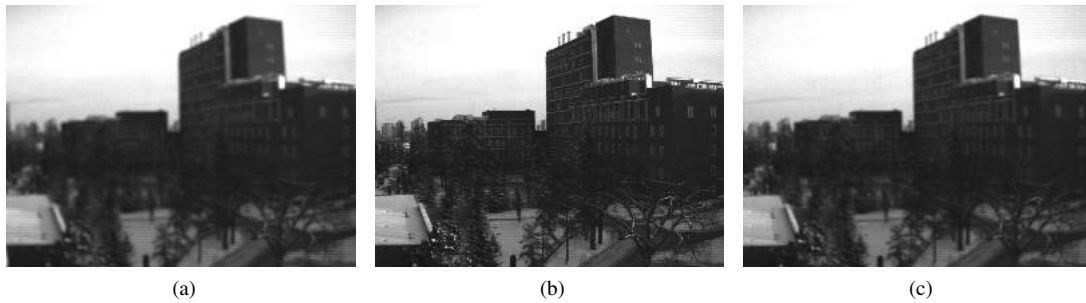


Figure 5.13: Sample images of the three highlighted points in the graph of Figure 5.12. (a) Out of focus (too far). (b) In-focus. (c) Out of focus (too close).

A test was also performed to find the standard deviation of the focus measurement with the lens with and without external vibrations. More than a 100 frames were captured for each case, and the focus metric was calculated. When leaving the lens fixed (no vibrations) a standard deviation for the focus measurement was 3.0302. For the lens under vibrations (lens held in place with the hand) the standard deviation for the focus measurement was 14.2966.

In practice, each camera was focused using the same target scene and the real-time focus measurement software. The reported real-time focus measure was used as an indicator to adjust the lenses to the best possible focus. An acceptable threshold for this scale was set at the maximum value (in-focus) minus 5. This means, for example, that in the case of the graph shown in Figure 5.12 where the maximum value (in-focus) is 85.63, a value above 80.63 will still produce an acceptable focused image.

5.8 Image Alignment

Alignment of the images for this system is more complex since cameras are organized in a 3x4 array, which means 2D translation is necessary. For this purpose, a subpixel registration algorithm based on intensity [100] was used. The algorithm minimizes the mean square intensity difference between a reference image and a test image. The transformation of the test image, in order to achieve alignment to the reference image, can be done by rigid-body motion (rotation and translation) only, or combined with isometric scaling.

The software platform ImageJ³, together with the image registration plugin StackReg⁴ were used for aligning the image sets. ImageJ [101] is a public Java-based image processing program developed at the National Institutes of Health. ImageJ offers multiple distributions with different features. The Fiji [102] distribution is the recommended updated general purpose option to this date, and it was the one used in this project. StackReg is a software implementation of the aforementioned algorithm [100], written as a java plugin for ImageJ by the Biomedical Imaging Group of the École Polytechnique Fédérale de Lausanne.

The algorithm uses each image of a stack (all the images or channel that belong to the same instant) as the template for aligning the next image. The first image of the stack is used as the anchor to begin the alignment process. The algorithm was implemented using rigid-body motion (rotation and translation) combined with isometric scaling. Scaling is used to account for any zooming effect that results from differences in focus. Performing these transformations in the images requires access to data outside the image frame. As such data is not available, it is replaced by zeroes in the output image. Figure 5.14 shows an example of two images being aligned. Transformations in the test image result in edges and empty spaces filled with zeroes, which translates to black borders framing the output image.

³<https://imagej.net>

⁴<http://www.epfl.ch/thevenaz/stackreg/>



Figure 5.14: Result of aligning two images. (a) Template or reference image. (b) Test image aligned to template image. It is possible to see the black borders filling the empty spaces after alignment.

ImageJ allows for the creation of scripts that help automate operations. A script was written in Java to run in ImageJ for taking a folder with multiples stacks of multiple images each and run a loop for aligning all the stacks. The program creates a folder where it saves all the aligned images using the same names. Figure 5.15 shows a comparison of a composite of 3 images superposed before and after alignment.

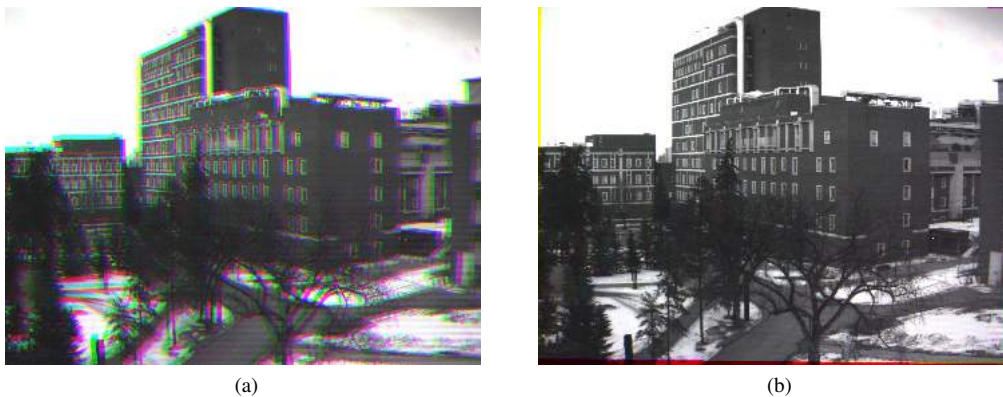


Figure 5.15: Result of image alignment algorithm. (a) Superposition before alignment. (b) Superposition after alignment.

A second version of the script was created where it is possible to export the transformation matrices of one stack and use it to align the rest of the stacks in the same folder. This implementation calculates the transformation matrix once and reuses it for the rest of the stacks, thus reducing processing time.

Chapter 6

Conclusions and Future Work

The work presented in this thesis introduces the development process of a UAV-compatible multi-spectral imaging system, detailing the design, construction, testing, and validation steps. The work covered the development of a customized fixed wing UAV, and later focuses on the development of the imaging system in all its revisions.

The UAV platform that was being used by the University of Alberta Aerial Robotics Group (UAARG) served as the starting point. The airframe was redesigned so as to improve construction, installation, maintenance, and more importantly, repeatability and reliability. The onboard autonomous navigation system hardware was redesigned to integrate all necessary components in a compact package, and a novel redundant power supply board was added. This UAV system board solution was designed to be fully compatible with the Paparazzi platform, and it can be used with any fixed-wing or rotary-wing airframe. The integration on all necessary components saves time during assembly, debugging, and deployment. Additionally, the system board gives access to expansion ports for further development. Overall, better wiring management inside the plane, more efficient use of internal volume, and the adoption of modularity, allowed the new version of the fixed wing UAV (Falcon I) to be a robust and reliable platform for research and development.

Imaging testing started with the evaluation of a small USB 2.0 CMOS camera module, with features that are similar to those found in webcams. USB 2.0 was chosen for its popularity and hardware/software relative simplicity compared to other interfaces such as USB 3.0, Firewire or Gigabit, which are also faster, but would increase weight and cost. The camera module was successfully studied and tested throughout different configurations. USB camera modules are relatively simple imaging systems based on an image sensor, a microcontroller, and a USB 2.0 interface. With a relatively wide variety of image sensor sizes, which in turn provide several resolution options, USB camera modules are a compact, simple, and efficient solution for aerial imaging. These types of cameras are an alternative option to higher end consumer cameras, offering a simpler hardware

that incorporates only the necessary components. This approach provides higher flexibility when it comes to developing custom imaging systems.

With the successful results of the USB camera module testing a custom 3-band multispectral imaging system was developed based on similar USB camera modules and optical filters. This proof of concept system used 3 monochromatic camera modules with a 1.2 megapixel CMOS image sensor. The selection of this resolution was based on a basic market research that looked at commercial UAV targeted multispectral cameras. Spectral bands used in these cameras was also studied, and a selection of three bands was made for this custom system. While filters can be easily replaceable, the green, red, and near infrared (NIR) bands were selected. A key factor is the selection of the cameras was the shutter. The cameras used in this system had a rolling shutter, in contrast with the global shutter that is used in commercial multispectral cameras. It was proved that using a rolling shutter for a 1.2 megapixels camera in standard fixed wing UAV flying conditions did not present negative effects. Common imaging problems associated with rolling shutter like skew and motion blur were not visible in any of the images during normal flight. Another key factor was the use of three free running cameras that were capturing images at 30 frames per second each with no synchronization between them. Custom software was written utilizing third party tools so as to interface with the cameras for configuration and image extraction. The developed software was optimized for low CPU usage and multiple camera interface, allowing software synchronization between the three cameras.

After successfully flying the 3-band multispectral imaging system, images were aligned using a custom alignment software written in MATLAB and based on matrix correlation. The software is a simplified implementation of one-dimensional translation that looks for a correlation maxima between two images. While simpler than more advanced image registration and alignment algorithms, it proved effective and fast. After alignment, the Normalized Difference Vegetation Index (NDVI) was calculated using the red and NIR images. Results showed successful and accurate detection of vegetation with clear identification between different levels of vegetation stress.

The subsequent evolution of the project was to develop a 12-band multispectral imaging system. In this case, the same approach of multiple USB cameras was maintained. Monochromatic camera modules with 1.2 megapixel CMOS image sensors were also used. The cameras selected for this system have a global shutter and an external trigger. The external trigger is a key feature of the system, allowing cameras to be accurately synchronized. A custom base board was designed containing a configurable USB HUB network and an onboard microcontroller that takes care of triggering the cameras. The system was built and tested with different configurations. The maximum number of simultaneous cameras for a certain configuration was determined. A way of estimating the maximum number of cameras based on resolution, frame rate, and the actual practical throughput of USB 2.0 (35-40 Mbytes/second) was provided. This customizable multi-camera imaging system provides a flexible and versatile development platform for multispectral imaging applications. A method for achieving in-focus for all cameras was presented, based on a custom software that quantifies focus in real-time. Using this focus metric it was possible to bring all cameras to the best possible focus us-

ing a reference target scene. Finally, an alignment method was also introduced based on the ImageJ image processing software. The alignment algorithm uses subpixel registration based on intensity, and can operate using two-dimensional translation, rotation, and isometric scaling.

In terms of costs, the 12-band multispectral imaging hardware presented in this work can achieve a considerably lower cost when compared to similar UAV compatible commercial multispectral cameras for the same number of bands. The custom bridge board is a multifunctional and important piece of hardware with a relatively low cost, which obviously drops as order quantities increase. A lower overall cost, higher development flexibility and control, and capacity for expansion, make this system a viable alternative to commercial off-the-shelf systems.

The whole process presented in this work followed a careful methodology that started with the testing of a single USB 2.0 camera module. After validation, this type of camera became the core of a multi-camera imaging system. The first revision or proof of concept consisted on a combination of 3 cameras and optical filters for the development a 3-band multispectral imaging system. After successful testing, the designed evolved into a 12-band multispectral imaging system with integrated USB HUB and automatic camera triggering system. The work done included hardware and software development, and provides a full imaging solution for custom applications. All the software development and code used in this project and referenced in this thesis can be found in the following github repository: <https://github.com/JLMARIN/imaging.git>.

6.1 Future Work

Future work of this thesis would contemplate the integration of small single board computers (SBC) into the 12-band multispectral imaging system. With the considerably low cost of SBCs, it should be possible to find a small but powerful board with minimal components, that would connect via USB to a group of cameras through the camera bridge board. The SCB would configure and extract images from the cameras, which are all synchronized thanks to the trigger system. With a network of several SBCs connected via a high bandwidth channel like ethernet or WiFi, a master SBC could gather all images from the other computers and have them stored in an SD card or transferred to an external system. The imaging platform and processing computer can be packaged together into a compact device.

A further hardware development step along the multi-camera imaging system would be to design a PCB with image sensors interfaced directly with an FPGA. This approach would allow costs to drop considerably, and would remove the relatively slow and limited USB 2.0 interface. With the FPGA talking directly to the sensors it would be possible to retrieve images from all of them simultaneously and store the images in an SD card.

Finally, it would be interesting and useful to make the system capable of integration with near infrared (NIR) and short-wave infrared (SWIR) cameras, expanding the spectrum coverage of the

overall system. If a trigger is present in such cameras, it can be synchronized with the trigger system that controls the Bridge board, and have the interface computer retrieve and save the images.

Bibliography

- [1] J. Wilford and J. Creasey, "Landsat thematic mapper," *Geophysical and Remote Sensing Methods for Regolith Exploration*, pp. 6–12, 2002.
- [2] B. L. Markham and J. L. Barker, "Spectral characterization of the landsat thematic mapper sensors," *International Journal of Remote Sensing*, vol. 6, no. 5, pp. 697–716, 1985.
- [3] J. Vogelmann, D. Helder, R. Morfitt, M. Choate, and J. Merchant, "Characterization of Landsat Thematic Mapper radiometry and geometry for land cover analysis," *IGARSS '98. Sensing and Managing the Environment. 1998 IEEE International Geoscience and Remote Sensing. Symposium Proceedings. (Cat. No.98CH36174)*, vol. 5, pp. 2405–2407 vol.5, 1998. [Online]. Available: <http://ieeexplore.ieee.org/lpdocs/epic03/wrapper.htm?arnumber=702228>
- [4] D. L. Williams, J. R. Irons, B. L. Markham, R. F. Nelson, D. L. Toll, R. S. Latty, and M. L. Stauffer, "A statistical evaluation of the advantages of Landsat Thematic Mapper data in comparison to Multispectral Scanner data," *IEEE Transactions on Geoscience and Remote Sensing*, vol. GE-22, no. 3, pp. 294–302, 1984.
- [5] R. D. Lees, W. R. Lettis, and R. Bernstein, "Evaluation of Landsat Thematic Mapper Imagery for Geologic Applications," *Proceedings of the IEEE*, vol. 73, no. 6, pp. 1108–1117, 1985.
- [6] D. Lamb, "The use of qualitative airborne multispectral imaging for managing agricultural crops-a case study in south-eastern Australia," *Australian Journal of Experimental Agriculture*, vol. 40, no. 5, pp. 725–738, 2000.
- [7] Y. Huang, S. J. Thomson, Y. Lan, and S. J. Maas, "Multispectral imaging systems for airborne remote sensing to support agricultural production management," *International Journal of Agricultural and Biological Engineering*, vol. 3, no. 1, pp. 50–62, 2010.
- [8] S. Nebiker, N. Lack, M. Abächerli, and S. Läderach, "Light-weight multispectral uav sensors and their capabilities for predicting grain yield and detecting plant diseases," *International Archives of the Photogrammetry, Remote Sensing and Spatial Information Sciences*, vol. 2016-Janua, no. July, pp. 963–970, 2016.

- [9] P. P. J. Roosjen, J. M. Suomalainen, H. M. Bartholomeus, and J. G. P. W. Clevers, "Hyperspectral reflectance anisotropy measurements using a pushbroom spectrometer on an unmanned aerial vehicle-results for barley, winter wheat, and potato," *Remote Sensing*, vol. 8, no. 10, pp. 1–16, 2016.
- [10] S. Candiago, F. Remondino, M. D. Giglio, M. Dubbini, and M. Gattelli, "Evaluating Multispectral Images and Vegetation Indices for Precision Farming Applications from UAV Images," *Remote Sensing*, vol. 7, no. Vi, pp. 4026–4047, 2015.
- [11] K. Themistocleous, A. Agapiou, B. Cuca, and D. G. Hadjimitsis, "Unmanned Aerial Systems and Spectroscopy for Remote Sensing Applications in Archaeology," *ISPRS - International Archives of the Photogrammetry, Remote Sensing and Spatial Information Sciences*, vol. XL-7/W3, no. May, pp. 1419–1423, 2015. [Online]. Available: <http://www.int-arch-photogramm-remote-sens-spatial-inf-sci.net/XL-7-W3/1419/2015/>
- [12] D. Turner, A. Lucieer, Z. Malenovsky, D. H. King, and S. A. Robinson, "Spatial co-registration of ultra-high resolution visible, multispectral and thermal images acquired with a micro-UAV over antarctic moss beds," *Remote Sensing*, vol. 6, no. 5, pp. 4003–4024, 2014.
- [13] L. Hassan-Esfahani, A. Torres-Rua, A. Jensen, and M. McKee, "Assessment of surface soil moisture using high-resolution multi-spectral imagery and artificial neural networks," *Remote Sensing*, vol. 7, no. 3, pp. 2627–2646, 2015.
- [14] Sentek Systems, "GEMS Multispectral Sensor," 2017. [Online]. Available: <http://precisionaguavs.com/sensors/>. [Accessed: 2017-06-23].
- [15] Sentera LLC, "Sentera Quad Sensor," 2017. [Online]. Available: <https://sentera.com/product/sentera-quad-sensor/>. [Accessed: 2017-06-23].
- [16] Parrot SA, "Parrot Sequoia," 2017. [Online]. Available: [https://www.parrot.com/ca/business-solutions/parrot-sequoia{#}parrot-sequoia-](https://www.parrot.com/ca/business-solutions/parrot-sequoia/#)parrot-sequoia-). [Accessed: 2017-06-22].
- [17] B. E. A. Saleh and M. C. Teich, *Fundamentals of Photonics*, 2nd ed. Hoboken, N.J.: Wiley-Interscience, 2007.
- [18] Wikimedia Commons, "Angle of view," 2012. [Online]. Available: en.wikipedia.org/wiki/File:Angle_of_view.svg. [Accessed: 2017-06-11].
- [19] Panasonic, "How Focal Length Affects Viewing Angle." [Online]. Available: <http://av.jpn.support.panasonic.com/support/global/cs/dsc/knowhow/knowhow12.html>. [Accessed: 2017-06-11].
- [20] LEMKE, "Do you know the difference between the CCD and CMOS chip technology?" 2014. [Online]. Available: <http://www.lemkevision.com/cn/news/>. [Accessed: 2017-06-11].

- [21] FLIR Knowledge Base, “Key differences between rolling shutter and frame (global) shutter,” 2015. [Online]. Available: www.ptgrey.com/kb/10028{#}. [Accessed: 2017-11-06].
- [22] T. York and R. Jain, “Fundamentals of Image Sensor Performance,” pp. 1–8, 2011. [Online]. Available: <http://www.cse.wustl.edu/{~}jain/cse567-11/ftp/imgsens/index.html>
- [23] P. Swain and D. Cheskis, “Back-Illuminated Image Sensors Come to the Forefront,” 2008. [Online]. Available: www.photonics.com/Article.aspx?AID=34685
- [24] V. Suntharalingam, R. Berger, S. Clark, J. Knecht, A. Messier, K. Newcomb, D. Rathman, R. Slattery, A. Soares, C. Stevenson, K. Warner, D. Young, P. Ang, Lin, B. Mansoorian, and D. Shaver, “A 4-side tileable back illuminated 3d-integrated Mpixel CMOS image sensor,” *Digest of Technical Papers - IEEE International Solid-State Circuits Conference*, pp. 38–40, 2009.
- [25] Edmund Optics, “Introduction to Modulation Transfer Function.” [Online]. Available: www.edmundoptics.com/resources/application-notes/optics/introduction-to-modulation-transfer-function/. [Accessed: 2017-11-16].
- [26] A. A. Michelson, *Studies in Optics*. Chicago, Ill: The University of Chicago Press, 1927.
- [27] Dxomark, “MTF.” [Online]. Available: <https://www.dxomark.com/glossary/mtf-2/>. [Accessed: 2017-11-27].
- [28] ISO, “ISO 12233:2017, Photography – Electronic still picture imaging – Resolution and spatial frequency responses,” 2017.
- [29] P. D. Burns, “Slanted-Edge MTF for Digital Camera and Scanner Analysis,” in *Proc. IS&T 2000 PICS Conference*, vol. 3, 2000, pp. 135–138.
- [30] S. E. Reichenbach, S. K. Park, and R. Narayanswamy, “Characterizing digital image acquisition devices,” *Optical Engineering*, vol. 30, no. 2, pp. 170–177, 1991.
- [31] D. Williams, “Benchmarking of the ISO 12233 Slanted-edge Spatial Frequency Response Plug-in Don,” in *IS&T's 1998 PICS Conference*, 1998.
- [32] P. D. Burns, “Refined slanted-edge measurement for practical camera and scanner testing,” *IS&T PICS Conference*, pp. 191–195, 2002.
- [33] P. D. Burns and D. Williams, “Digital Camera and Scanner Performance Evaluation : Standards and Software,” in *SPIE/IS&T Electronic Imaging Symposium*, 2014, pp. 1–41.
- [34] P. D. Burns and D. Williams, “Sampling Efficiency in Digital Camera Performance Standards,” in *Proc. SPIE*, vol. 6808, 2008, pp. 1 – 5.

- [35] M. H. Schimek, B. Dirks, H. Verkuil, and M. Rubli, *Video for Linux two API specification - Revision 0.24*, 2008.
- [36] L. Yinli, Y. Hongli, and Z. Pengpeng, "The Implementation of Embedded Image Acquisition Based on V4L2," *2011 International Conference on Electronics, Communications and Control (Icecc)*, pp. 549–552, 2011.
- [37] S. D. Burks and J. M. Doe, "GStreamer as a framework for image processing applications in image fusion," *Proc. SPIE 8064, Multisensor, Multisource Information Fusion: Architectures, Algorithms, and Applications 2011*, vol. 8064, pp. 80 640M–80 640M–7, 2011. [Online]. Available: <http://dx.doi.org/10.1117/12.884797>
- [38] Gstreamer.freedesktop.org, "What is GStreamer?" [Online]. Available: <https://gstreamer.freedesktop.org/documentation/application-development/introduction/gstreamer.html>. [Accessed: 2018-01-18].
- [39] Tetracam Inc., "Tetracam ADC Micro," 2017. [Online]. Available: [http://tetracam.com/Products-ADC\[_\]Micro.htm](http://tetracam.com/Products-ADC[_]Micro.htm). [Accessed: 2017-06-22].
- [40] Tetracam Inc., "Tetracam Mini MCA," 2017. [Online]. Available: [http://www.tetracam.com/Products-Mini\[_\]MCA.htm](http://www.tetracam.com/Products-Mini[_]MCA.htm). [Accessed: 2017-06-22].
- [41] A. Burkart, S. Cogliati, A. Schickling, and U. Rascher, "A novel UAV-Based ultra-light weight spectrometer for field spectroscopy," *IEEE Sensors Journal*, vol. 14, no. 1, pp. 62–67, 2014.
- [42] J. Suomalainen, N. Anders, S. Iqbal, G. Roerink, J. Franke, P. Wenting, D. Hünninger, H. Bartholomeus, R. Becker, and L. Kooistra, "A lightweight hyperspectral mapping system and photogrammetric processing chain for unmanned aerial vehicles," *Remote Sensing*, vol. 6, no. 11, pp. 11 013–11 030, 2014.
- [43] F. Agüera, F. Carvajal, and M. Pérez, "Measuring Sunflower Nitrogen Status From an Unmanned Aerial Vehicle-Based System and an on the Ground Device," *ISPRS - International Archives of the Photogrammetry, Remote Sensing and Spatial Information Sciences*, vol. XXXVIII-1/, no. September, pp. 33–37, 2011.
- [44] J. S. West, C. Bravo, R. Oberti, D. Lemaire, D. Moshou, and H. A. McCartney, "The Potential of Optical Canopy Measurement for Targeted Control of Field Crop Diseases," *Annual Review of Phytopathology*, vol. 41, no. 1, pp. 593–614, 2003. [Online]. Available: <http://www.annualreviews.org/doi/10.1146/annurev.phyto.41.121702.103726>
- [45] S. Jacquemoud and S. L. Ustin, "Leaf optical properties: a state of the art," *Proc. 8th International Symposium Physical Measurements & Signatures in Remote Sensing*, no. January, pp. 223–232, 2001. [Online]. Available: citeulike-article-id:7215646

- [46] Y. Wang, G. Li, J. Ding, Z. Guo, S. Tang, R. Liu, and J. Chen, "A combined GLAS and MODIS estimation of the global distribution of mean forest canopy height," *Remote Sensing of Environment*, vol. 174, pp. 24–43, 2016. [Online]. Available: <http://dx.doi.org/10.1016/j.rse.2015.12.005>
- [47] Y. Knyazikhin, M. A. Schull, P. Stenberg, M. Möttus, M. Rautiainen, Y. Yang, A. Marshak, P. Latorre Carmona, R. K. Kaufmann, P. Lewis, M. I. Disney, V. Vanderbilt, A. B. Davis, F. Baret, S. Jacquemoud, A. Lyapustin, and R. B. Myneni, "Hyperspectral remote sensing of foliar nitrogen content." *Proceedings of the National Academy of Sciences of the United States of America*, vol. 110, no. 3, pp. E185–92, 2013. [Online]. Available: <http://www.pnas.org/content/110/3/E185.short>
- [48] M. Kneubühler, B. Koetz, S. Huber, M. E. Schaepman, and N. E. Zimmermann, "Space-based spectrodirectional measurements for the improved estimation of ecosystem variables," *Canadian Journal of Remote Sensing*, vol. 34, no. 3, pp. 192–205, 2008.
- [49] Z. Wang, C. A. Coburn, X. Ren, and P. M. Teillet, "Effect of soil surface roughness and scene components on soil surface bidirectional reflectance factor," *Canadian Journal of Soil Science*, vol. 92, no. 2, pp. 297–313, 2012.
- [50] P. P. J. Roosjen, H. M. Bartholomeus, and J. G. P. W. Clevers, "Effects of soil moisture content on reflectance anisotropy - Laboratory goniometer measurements and RPV model inversions," *Remote Sensing of Environment*, vol. 170, pp. 229–238, 2015. [Online]. Available: <http://dx.doi.org/10.1016/j.rse.2015.09.022>
- [51] A. Bannari, D. Morin, F. Bonn, and A. R. Huete, "A review of vegetation indices," *Remote Sensing Reviews*, vol. 13, no. 1, pp. 95–120, 1995. [Online]. Available: <http://dx.doi.org/10.1080/02757259509532298>
- [52] A. Matese, F. Capraro, J. Primicerio, G. Gualato, S. Gennaro, and G. Agati, "Mapping of vine vigor by UAV and anthocyanin content by a non-destructive fluorescence technique," in *Stafford J.V. (eds) Precision agriculture '13*. Wageningen: Wageningen Academic Publishers, 2013, pp. 201–208.
- [53] A. a. Gitelson, Y. Gritz, and M. N. Merzlyak, "Relationships between leaf chlorophyll content and spectral reflectance and algorithms for non-destructive chlorophyll assessment in higher plant leaves." *Journal of plant physiology*, vol. 160, no. 3, pp. 271–82, 2003.
- [54] H. Zheng, X. Zhou, T. Cheng, X. Yao, Y. Tian, W. Cao, and Y. Zhu, "Evaluation of a UAV-based Hyperspectral Frame Camera for Monitoring the Leaf Nitrogen Concentration in Rice," in *Geoscience and Remote Sensing Symposium (IGARSS)*, 2016, pp. 7350–7353.

- [55] I. Pölönen, H. Saari, J. Kaivosoja, E. Honkavaara, and L. Pesonen, "Hyperspectral imaging based biomass and nitrogen content estimations from light-weight UAV," in *Proceedings of SPIE - The International Society for Optical Engineering*, 2013.
- [56] V. P. Polischuk, T. M. Shadchina, T. I. Kompanetz, I. G. Budzanivskaya, A. L. Boyko, and A. A. Sozinov, "Changes in reflectance spectrum characteristic of nicotiana debneyi plant under the influence of viral infection," *Archives Of Phytopathology And Plant Protection*, vol. 31, no. 1, pp. 115–119, 1997. [Online]. Available: <http://dx.doi.org/10.1080/03235409709383221>
- [57] R. Näsi, E. Honkavaara, P. Lyytikäinen-Saarenmaa, M. Blomqvist, P. Litkey, T. Hakala, N. Viljanen, T. Kantola, T. Tanhuanpää, and M. Holopainen, "Using UAV-based photogrammetry and hyperspectral imaging for mapping bark beetle damage at tree-level," in *Remote Sensing*, no. 11, 2013, pp. 15 467–15 493.
- [58] F. Garcia-Ruiz, S. Sankaran, J. M. Maja, W. S. Lee, J. Rasmussen, and R. Ehsani, "Comparison of two aerial imaging platforms for identification of Huanglongbing-infected citrus trees," *Computers and Electronics in Agriculture*, vol. 91, pp. 106–115, 2013. [Online]. Available: <http://dx.doi.org/10.1016/j.compag.2012.12.002>
- [59] J. Flexas, J. M. Escalona, and H. Medrano, "Water stress induces different levels of photosynthesis and electron transport rate regulation in grapevines," *Plant, Cell and Environment*, vol. 22, no. 1, pp. 39–48, 1999.
- [60] J. Flexas, J. M. Escalona, S. Evain, J. Gulías, I. Moya, C. B. Osmond, and H. Medrano, "Steady-state chlorophyll fluorescence (Fs) measurements as a tool to follow variations of net CO₂ assimilation and stomatal conductance during water-stress in C₃ plants," *European Space Agency, (Special Publication) ESA SP*, no. 527, pp. 26–29, 2002.
- [61] P. J. Zarco-Tejada, V. González-Dugo, and J. A. J. Berni, "Fluorescence, temperature and narrow-band indices acquired from a UAV platform for water stress detection using a micro-hyperspectral imager and a thermal camera," *Remote Sensing of Environment*, vol. 117, pp. 322–337, 2012. [Online]. Available: <http://dx.doi.org/10.1016/j.rse.2011.10.007>
- [62] E. Honkavaara, M. A. Eskelinen, I. Polonen, H. Saari, H. Ojanen, R. Mannila, C. Holmlund, T. Hakala, P. Litkey, T. Rosnell, N. Viljanen, and M. Pulkkanen, "Remote Sensing of 3-D Geometry and Surface Moisture of a Peat Production Area Using Hyperspectral Frame Cameras in Visible to Short-Wave Infrared Spectral Ranges Onboard a Small Unmanned Airborne Vehicle (UAV)," *IEEE Transactions on Geoscience and Remote Sensing*, vol. 54, no. 9, pp. 5440–5454, 2016.
- [63] R. Bryant, D. Thoma, S. Moran, C. Holifield, D. Goodrich, T. Keefer, G. Paige, David, Williams, and S. Skirvin, "Evaluation of Hyperspectral, Infrared Temperature and Radar

- Measurements for Monitoring Surface Soil Moisture,” *First Interagency Conference in the Watersheds*, pp. 528–533, 2003.
- [64] M. P. Finn, M. D. Lewis, D. D. Bosch, M. Giraldo, K. Yamamoto, D. G. Sullivan, R. Kincaid, R. Luna, G. K. Allam, C. Kvien, and M. S. Williams, “Remote Sensing of Soil Moisture Using Airborne Hyperspectral Data,” *GIScience & Remote Sensing*, vol. 48, no. 4, pp. 522–540, 2011.
- [65] C. S. Allen, M. P. S. Krekeler, C. Scott Allen, and M. P. S. Krekeler, “Reflectance spectra of crude oils and refined petroleum products on a variety of common substrates,” *Proceedings of SPIE*, vol. 7687, no. May 2012, pp. 76 870L–1–76 870L–13, 2010.
- [66] B. Hörig, F. Kühn, F. Oschütz, and F. Lehmann, “HyMap hyperspectral remote sensing to detect hydrocarbons,” *International Journal of Remote Sensing*, vol. 22, no. 8, pp. 1413–1422, 2001.
- [67] I. Leifer, W. J. Lehr, D. Simecek-Beatty, E. Bradley, R. Clark, P. Dennison, Y. Hu, S. Matheson, C. E. Jones, B. Holt, M. Reif, D. A. Roberts, J. Svejksky, G. Swayze, and J. Wozencraft, “State of the art satellite and airborne marine oil spill remote sensing: Application to the BP Deepwater Horizon oil spill,” *Remote Sensing of Environment*, vol. 124, pp. 185–209, 2012. [Online]. Available: <http://dx.doi.org/10.1016/j.rse.2012.03.024>
- [68] R. N. Clark, G. A. Swayze, I. Leifer, K. E. Livo, R. Kokaly, T. Hoefen, S. Lundeen, M. Eastwood, R. O. Green, N. Pearson, C. Sarture, I. Mccubbin, D. Roberts, E. Bradley, D. Steele, T. Ryan, R. Dominguez, and Airborne Visible/Infrared Imaging Spectrometer (AVIRIS) Team, “A method for quantitative mapping of thick oil spills using imaging spectroscopy,” Tech. Rep. 1167, 2010.
- [69] B. Rivard, J. Feng, V. Bushan, and M. Lipsett, “Infrared reflectance hyperspectral features of Athabasca oil sand ore and froth,” *Workshop on Hyperspectral Image and Signal Processing, Evolution in Remote Sensing*, pp. 0–3, 2011.
- [70] B. Rivard, D. Lyder, J. Feng, A. Gallie, E. Cloutis, P. Dougan, S. Gonzalez, D. Cox, and M. G. Lipsett, “Bitumen content estimation of Athabasca oil sand from broad band infrared reflectance spectra,” *Canadian Journal of Chemical Engineering*, vol. 88, no. 5, pp. 830–838, 2010.
- [71] D. Hausamann, W. Zirnig, G. Schreier, and P. Strobl, “Monitoring of gas pipelines - a civil UAV application,” *Aircraft Engineering and Aerospace Technology*, vol. 77, no. 5, pp. 352–360, 2005. [Online]. Available: <http://www.emeraldinsight.com/doi/10.1108/00022660510617077>

- [72] J. Tuominen and T. Lipping, "Detection of Environmental Change Using Hyperspectral Remote Sensing at Olkiluoto Repository Site," POSIVA OY, Eurajoki, Finland, Tech. Rep., 2011.
- [73] A. J. S. McGonigle, A. Aiuppa, G. Giudice, G. Tamburello, A. J. Hodson, and S. Gurrieri, "Unmanned aerial vehicle measurements of volcanic carbon dioxide fluxes," *Geophysical Research Letters*, vol. 35, no. 6, pp. 3–6, 2008.
- [74] A. Agapiou, D. G. Hadjimitsis, and D. D. Alexakis, "Evaluation of broadband and narrow-band vegetation indices for the identification of archaeological crop marks," *Remote Sensing*, vol. 4, no. 12, pp. 3892–3919, 2012.
- [75] M. Doneus, G. Verhoeven, C. Atzberger, M. Wess, and M. Rus, "New ways to extract archaeological information from hyperspectral pixels," *Journal of Archaeological Science*, vol. 52, pp. 84–96, 2014.
- [76] D. C. Cowley, C. Moriarty, G. Geddes, G. L. Brown, T. Wade, and C. J. Nichol, "UAVs in Context: Archaeological Airborne Recording in a National Body of Survey and Record," *Drones*, vol. 2, no. 2, pp. 1–16, 2018.
- [77] C. Moriarty, "Deploying Multispectral Remote Sensing for Multitemporal Analysis of Archaeological Crop Stress at Ravenshall, Fife," Master's Thesis, University of Edinburgh, 2017.
- [78] H. Chao, Y. Cao, and Y. Chen, "Autopilots for small unmanned aerial vehicles: A survey," *International Journal of Control, Automation and Systems*, vol. 8, no. 1, pp. 36–44, 2010.
- [79] H. Lim, J. Park, D. Lee, and H. J. Kim, "Build your own quadrotor: Open-source projects on unmanned aerial vehicles," *IEEE Robotics and Automation Magazine*, vol. 19, no. 3, pp. 33–45, 2012.
- [80] E. Ebeid, M. Skriver, and J. Jin, "A Survey on Open-Source Flight Control Platforms of Unmanned Aerial Vehicle," in *Euromicro Symposium on Digital Systems Design*. IEEE, 2017.
- [81] B. Remes, P. Esden-Tempski, F. Van Tienen, E. Smeur, C. De Wagter, and G. De Croon, "Lisa-S 2.8g autopilot for GPS-based flight of MAVs," *IMAV 2014, International Micro Air Vehicle Conference and Competition 2014*, pp. 280–285, 2014.
- [82] R. W. Beard, D. Kingston, M. Quigley, D. Snyder, R. Christiansen, W. Johnson, T. McLain, and M. Goodrich, "Autonomous Vehicle Technologies for Small Fixed-Wing UAVs," *Journal of Aerospace Computing, Information, and Communication*, vol. 2, no. 1, pp. 92–108, 2005.

- [83] D. Stojcsics and A. Molnár, "AirGuardian - UAV hardware and software system for small size UAVs," *International Journal of Advanced Robotic Systems*, vol. 9, pp. 1–8, 2012.
- [84] MicroPilot Company, "MP2128-3X MicroPilot's Triple Redundant UAV Autopilot," Tech. Rep. [Online]. Available: <https://www.micropilot.com/pdf/white-papers/mp21283x.pdf>
- [85] J. Marin, R. Augustine, M. Lipsett, and Duncan G. Elliott, "An Open Source Comprehensive System Board for UAVs with Redundant Power," in *Unmanned Canada 2016 Conference*, Edmonton, 2016.
- [86] B. Gati and Paparazzi Community, "Open Source Autopilot for Academic Research - The Paparazzi System," *Proceeding of the American Control Conference 2013*, pp. 1478–1481, 2013.
- [87] P. Brisset, A. Drouin, M. Gorraz, P.-s. Huard, and J. Tyler, "The Paparazzi Solution," *MAV 2006, 2nd US-European Competition and Workshop on Micro Air Vehicles*, pp. 1–15, 2006.
- [88] G. Hattenberger, M. Bronz, and M. Gorraz, "Using the Paparazzi UAV System for Scientific Research," *IMAV 2014, International Micro Air Vehicle Conference and Competition 2014*, pp. 247–252, 2014.
- [89] P. Burns, "sfrmat3: SFR evaluation for digital cameras and scanners," 2015. [Online]. Available: <http://losburns.com/imaging/software/SFRedge/>. [Accessed: 2017-04-10].
- [90] J. P. Jhan, J. Y. Rau, N. Haala, and M. Cramer, "Investigation of parallax issues for multi-lens multispectral camera band co-registration," *International Archives of the Photogrammetry, Remote Sensing and Spatial Information Sciences - ISPRS Archives*, vol. 42, no. 2W6, pp. 157–163, 2017.
- [91] A. Bhandari, A. Kumar, and G. Singh, "Feature Extraction using Normalized Difference Vegetation Index (NDVI): A Case Study of Jabalpur City," *Procedia Technology*, vol. 6, pp. 612–621, 2012.
- [92] QImaging, "Global Shutter vs. Rolling Shutter Readouts," pp. 1–9, 2014. [Online]. Available: <https://www.qimaging.com/ccdorscmos/pdfs/RollingvsGlobalShutter.pdf>
- [93] W. Hong, D. Wei, and A. U. Batur, "Video stabilization and rolling shutter distortion reduction," in *Proceedings - International Conference on Image Processing, ICIP*, 2010, pp. 3501–3504.
- [94] Z. W. Pan, H. L. Shen, C. Li, S. J. Chen, and J. H. Xin, "Fast Multispectral Imaging by Spatial Pixel-Binning and Spectral Unmixing," *IEEE Transactions on Image Processing*, vol. 25, no. 8, pp. 3612–3625, 2016.

- [95] Arduino, “Arduino - Home Page,” 2018. [Online]. Available: <https://www.arduino.cc/>. [Accessed: 2018-02-05].
- [96] J. C. Martínez-Santos, O. Acevedo-Patino, and S. H. Contreras-Ortiz, “Influence of Arduino on the Development of Advanced Microcontrollers Courses,” *Revista Iberoamericana de Tecnologías del Aprendizaje*, vol. 12, no. 4, pp. 208–217, 2017.
- [97] A. Orebaugh, G. Ramirez, and J. Beale, *Wireshark & Ethereal Network Protocol Analyzer Toolkit*. Elsevier, 2006.
- [98] S. Pertuz, D. Puig, and M. A. Garcia, “Analysis of focus measure operators for shape-from-focus,” *Pattern Recognition*, vol. 46, no. 5, pp. 1415–1432, 2013. [Online]. Available: <http://dx.doi.org/10.1016/j.patcog.2012.11.011>
- [99] J. Pech-Pacheco, G. Cristobal, J. Chamorro-Martinez, and J. Fernandez-Valdivia, “Diatom autofocusing in brightfield microscopy: a comparative study,” *Proceedings 15th International Conference on Pattern Recognition. ICPR-2000*, vol. 3, pp. 314–317, 2000. [Online]. Available: <http://ieeexplore.ieee.org/document/903548/>
- [100] P. Thévenaz, U. E. Ruttimann, and M. Unser, “A pyramid approach to subpixel registration based on intensity,” *IEEE Transactions on Image Processing*, vol. 7, no. 1, pp. 27–41, 1998.
- [101] C. T. Rueden, J. Schindelin, M. C. Hiner, B. E. DeZonia, A. E. Walter, E. T. Arena, and K. W. Eliceiri, “ImageJ2: ImageJ for the next generation of scientific image data,” *BMC Bioinformatics*, vol. 18, no. 1, pp. 1–26, 2017.
- [102] J. Schindelin, I. Arganda-Carreras, E. Frise, V. Kaynig, M. Longair, T. Pietzsch, S. Preibisch, C. Rueden, S. Saalfeld, B. Schmid, J. Y. Tinevez, D. J. White, V. Hartenstein, K. Eliceiri, P. Tomancak, and A. Cardona, “Fiji: An open-source platform for biological-image analysis,” *Nature Methods*, vol. 9, no. 7, pp. 676–682, 2012.

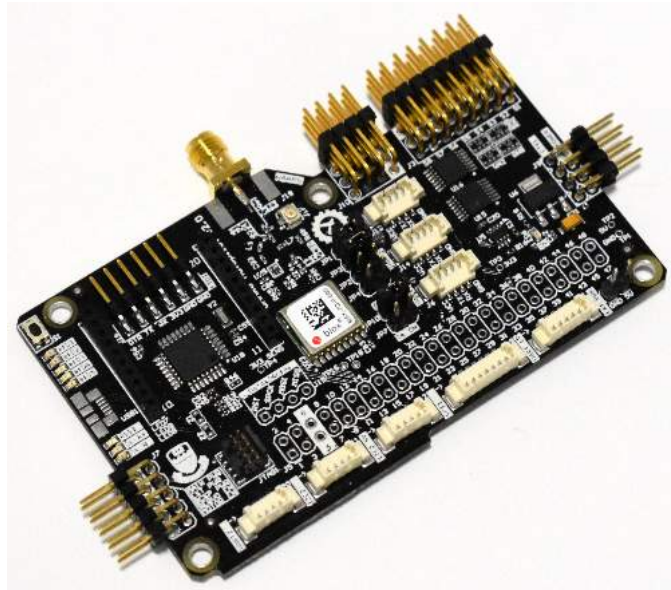
Appendix A

UAV System Board User Guide

Autopilot Embedded System Board - Falcon I User Guide

Jorge Marin and Duncan G. Elliott

Rev. 1.5 - March 29, 2018



Introduction

This user guide introduces the Autopilot Embedded System Board as part of the *Falcon I* project developed in the University of Alberta, and describes the use and development capabilities for Unmanned Aerial Vehicle (UAV) applications. This project was developed with the support and assistance of Rijesh Augustine, and the University of Alberta Aerial Robotics Group (UAARG).

Scope

This guide provides details on the Falcon I Autopilot system. It is made up of four main sections:

- Section 1 - describes the Falcon I Autopilot main features.
- Section 2 - provides instructions to power up the Falcon I Autopilot board.
- Section 3 - provides an overview of the Falcon I Autopilot board.
- Section 4 - describes the Falcon I Autopilot board components.

Related Items

- [STMicroelectronics STM32F405 Datasheet](http://www.st.com/content/ccc/resource/technical/document/datasheet/ef/92/76/6d/bb/c2/4f/f7/DM00037051.pdf/files/DM00037051.pdf/jcr:content/translations/en.DM00037051.pdf) (<http://www.st.com/content/ccc/resource/technical/document/datasheet/ef/92/76/6d/bb/c2/4f/f7/DM00037051.pdf/files/DM00037051.pdf/jcr:content/translations/en.DM00037051.pdf>)

Contents

| | | |
|----------|---|-----------|
| 1 | Specifications | 4 |
| 1.1 | Electrostatic Warning | 4 |
| 1.2 | Power Supply Warning | 4 |
| 2 | Power Up | 5 |
| 2.1 | Power Up the Board | 5 |
| 2.2 | Programming | 5 |
| 3 | Hardware Introduction | 6 |
| 3.1 | Introduction | 6 |
| 3.2 | Equipment List | 6 |
| 3.3 | Board Features | 6 |
| 4 | Board Components | 7 |
| 4.1 | Board Overview | 7 |
| 4.2 | Function Blocks | 9 |
| 4.2.1 | Microcontroller Unit (MCU) | 9 |
| 4.2.2 | Power Supply | 9 |
| 4.2.3 | Inertial Measurement Unit (IMU) | 9 |
| 4.2.4 | GPS | 10 |
| 4.2.5 | XBee | 10 |
| 4.2.6 | Data-Logger | 10 |
| 4.2.7 | CAN Transceiver | 11 |
| 4.2.8 | Motor/Servo Outputs (PWM) | 11 |
| 4.2.9 | Connectors | 11 |
| 4.2.10 | Jumpers | 23 |
| 4.3 | Board Pictures | 27 |
| 4.4 | Autopilot Board Schematics | 28 |
| 4.5 | Autopilot Board Bill-of-Materials (BOM) | 45 |
| 5 | Revision History | 48 |

1 Specifications

Table 1.1: Board Specifications.

| Characteristic | Specifications |
|--|--------------------------------|
| Temperature: - Operating - Storage | 0°C to +70°C -40°C to +85°C |
| Relative Humidity | 0 to 90% (non-condensing) |
| RoHS status | Compliant |

1.1 Electrostatic Warning



Warning: ESD-Sensitive Electronic Equipment!

The board system must not be subject to high electrostatic potentials.

It is strongly recommended to use a grounding strap or similar ESD protective device when handling the board in hostile ESD environments (for example, places with synthetic carpets). Avoid touching the component pins or any other metallic element on the board.

1.2 Power Supply Warning



Warning: Hardware Power Supply Limitation

Power supply must be 5VDC. Using a power adapter greater than 5VDC may damage the board.

Warning: Hardware Power Budget

Using the USB port as the main power source (max. 500 mA) is acceptable when using the on-board peripherals only.

When connecting external peripherals or add-on boards, it is recommended the use of an external power source connected to the J9 POWER header (can provide up to 1A on the 3.3V node).

2 Power Up

Several power source options are available to power up the Falcon I Autopilot board.

The board can be:

- USB-powered through the Micro USB connector (USB1 connector).
- Powered through an external 5V source connected via the J9 POWER header. The external power source must be able to supply 200mA just for the board to work with the basic configuration. Additional peripherals or boards connected might require more supply current.
- Powered through an external 5V source connected via the J5 expansion header - pins 1 and 2. Same conditions as above.

Warning: The Falcon I Autopilot board runs at 3.3V. The maximum voltage that the I/O pins can tolerate is 3.3V. Providing higher voltages (e.g. 5V) to an I/O pin could damage the board.

2.1 Power Up the Board

Take the board and connect 5V and GND through the J9 POWER header (check pinout information for J9 to see what pins to use).

Table 2.1: Electrical Characteristics.

| Electrical Parameter | Values |
|-------------------------------|-----------|
| Input Voltage | 5VDC |
| Max DC 3.3V Current Available | 1A |
| I/O Voltage | 3.3V only |

2.2 Programming

The Falcon I Autopilot board is fully compatible with the Lisa MX from 1 Bit Square, and therefore can be programmed using the same external programmer. This programmer is called “*Black Magic Probe*”, and connects directly to the Falcon I Autopilot board through the JTAG port. Connect the other end to a free USB port of your PC using a mini-USB to USB cable.

Open PaparazziUAV, and configure and program the board using the same source files used with the Lisa MX.

3 Hardware Introduction

3.1 Introduction

The Falcon I Autopilot board is a fully-featured development platform for UAV applications. It integrates all major components needed for UAV autopilot control.

3.2 Equipment List

The Falcon I Autopilot board is built around the integration of a Cortex®-M4-based microcontroller with floating-point unit, 3-axis accelerometer, gyroscope, and magnetometer, barometer, GPS unit, secondary microcontroller with SD card for data-logging, 8 PWM outputs for motors/servos and expansion headers and connectors.

3.3 Board Features

Table 3.1: Board Specifications.

| Characteristics | Specifications |
|----------------------|---|
| PCB characteristics | 90 x 52 x 11mm (4-layers) |
| Microcontroller | STM32F405VGT6 - 168MHz 32-bit ARM® Cortex® M4 MCU with 192KB RAM, 1024KB Flash, and floating point unit (FPU) |
| USB | One Micro-USB |
| 10 DOF IMU | 3 axis accelerometer 3 axis gyroscope 3 axis magnetometer barometer |
| Remote Control | Two UART ports for remote control receivers |
| Telemetry | One socket for XBee radio |
| GPS | One uBlox MAX-7Q GPS unit The GPS on-board circuitry includes: - SAW filter - Optional LNA - Selectable uFL or SMA connector for GPS antenna |
| Debug Port | One JTAG interface connector |
| PWM Outputs | Eight PWM outputs for motors/servos |
| Data-logger | Secondary MCU and micro-SD card socket for telemetry data-logging |
| Expansion Connectors | - One high speed SPI interface for high speed hardware expansion - Two I2C interfaces for actuators and sensors - One CAN interface (with onboard transceiver) for actuators and sensors - Three General Purpose IO pins - Three analog inputs - One UART port with adjustable level shifter - One 48-pin header with access to multiple MCU pins |
| Board Supply Voltage | 5V from USB or J9 POWER header On-board power regulation to 3.3V is performed by a LDO linear voltage regulator |
| User Interface | Bind button Eight indicator LEDs for status check |

4 Board Components

4.1 Board Overview

The Falcon I Autopilot board integrates several peripherals and interface connectors, as shown in Figures 4.1 and 4.2.

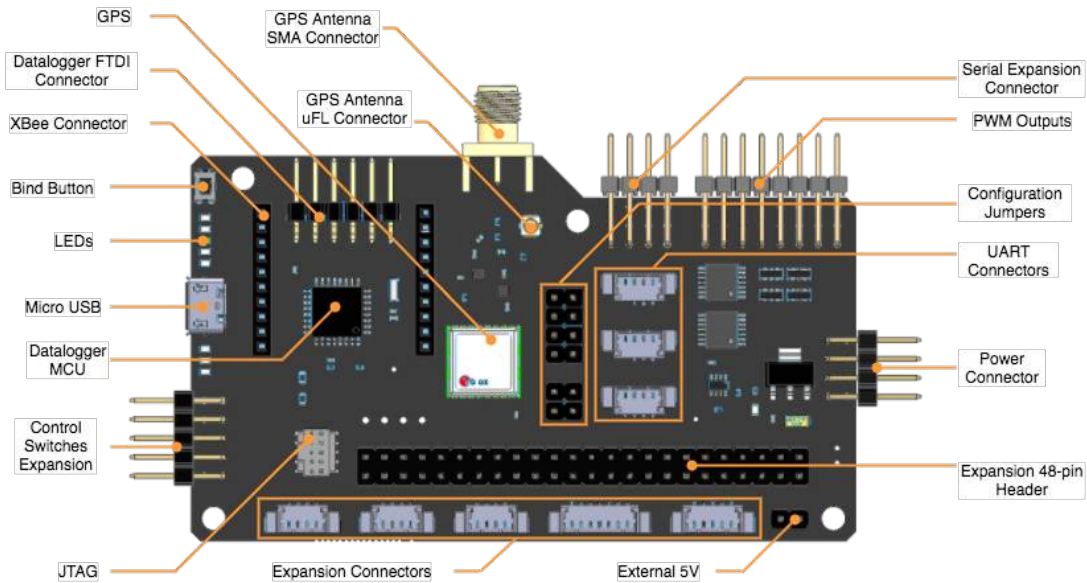


Figure 4.1: Falcon I Autopilot Board Overview (Top).

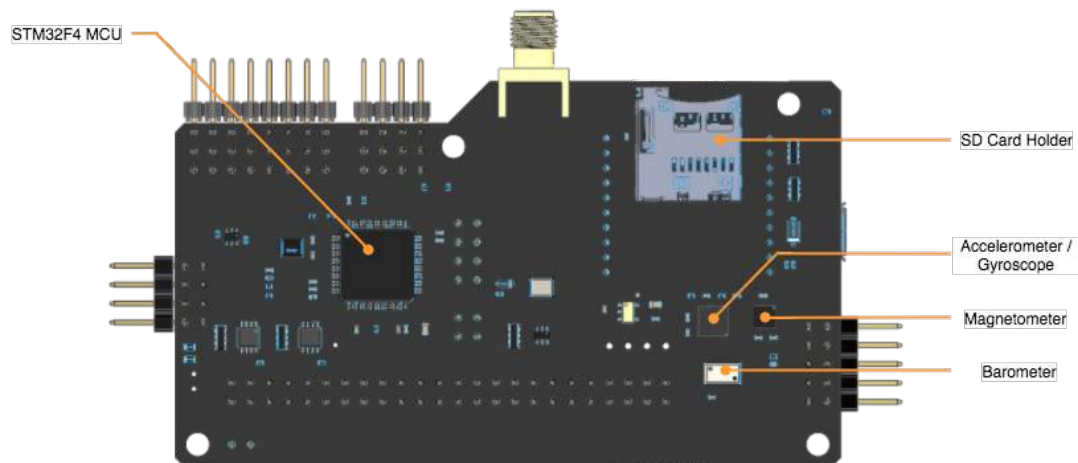


Figure 4.2: Falcon I Autopilot Board Overview (Bottom).

The Falcon I Autopilot board is equipped with the following interface connectors:

- J3: PWM outputs for motors/servos
- J5: Expansion 48-pin header with access to power, GPIO, and communication ports
- J6: UART3 port (connected to GPS)
- J7: Control switches connector
- J9: Main power supply
- J10: Expansion connector with two UART ports (UART1 and UART5) for RC receivers and one I2C port (I2C1)
- J11: I2C 3.3V port (I2C2)
- J12: I2C 5V port (I2C2)
- J13: UART1 port (for RC receiver)
- J14: UART5 port (for RC receiver)
- J15: ISP connector for data-logger MCU
- J16: FTDI connector for data-logger MCU
- J17: uFL connector for GPS antenna
- J18: SMA connector for GPS antenna
- J19: SPI port
- J20: UART2 port (connected to XBee)
- J21: UART port with voltage level converter
- J22: Secondary 5V supply for external system
- JTAG1: JTAG 10-pin connector
- USB1: micro-USB connector
- EX1, EX2: Female sockets for XBee
- Various test points located throughout the board

4.2 Function Blocks

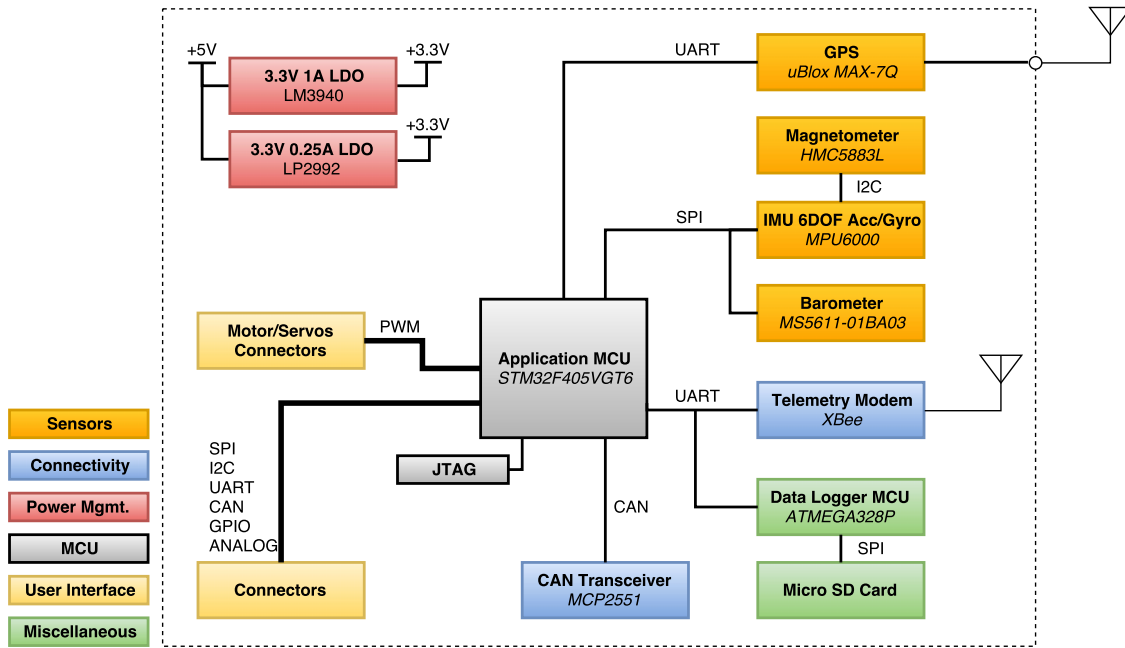


Figure 4.3: Falcon I Autopilot Board Block Diagram.

4.2.1 Microcontroller Unit (MCU)

The Falcon I Autopilot board is built around the STM32F405VGT6, a 32-bit ARM® Cortex® M4 microcontroller running at 168MHz with 192KB RAM, 1024KB Flash, and a floating point unit (FPU). The microcontroller includes CAN, I2C, I2S, SPI and UART communication interfaces, 82 I/O and 10 Timers in a LQFP-100 package.

4.2.2 Power Supply

The on-board power supply is split into two 3.3V Low Drop-Out (LDO) voltage regulators. The first voltage regulator (LP2992AIM5-3.3) supplies power to the accelerometer, gyroscope, magnetometer and barometer sensors, so as to reduce noise in the measurements, while the second voltage regulator (LM3940IMPX-3.3) supplies power to the rest of the board. The latter is capable of delivering up to 1A.

4.2.3 Inertial Measurement Unit (IMU)

The board features a 10 Degrees-of-Freedom (DOF) Inertial Measurement Unit (IMU) comprised by a 3-axis accelerometer and 3-axis gyroscope (MPU6000), a 3-axis magnetometer (HMC5883L) and a barometer (MS5611-01BA03).

The accelerometer/gyroscope and the barometer are connected via SPI interface with the MCU, and the magnetometer is connected to the accelerometer/gyroscope via I2C interface.

The accelerometer/gyroscope acts as a master with the magnetometer, pulling the data and saving it locally, allowing the MCU to extract data from these three sensors directly from the MPU6000 via SPI.

4.2.4 GPS

The board includes a uBlox MAX-7Q GPS module with a super-capacitor for hot start and antenna matching circuitry. The GPS works in the 1575.42Mhz band. The antenna circuitry includes a SAW filter and optional Low Noise Amplifier (LNA) that can be enabled/disabled by means of on-board 0 ohm jumper resistors. The board also includes uFL and SMA connectors for GPS antenna. The connectors can also be selected using 0 ohm jumper resistors.

The default setup includes the SMA connector selected and the LNA disabled, so as to use an active antenna. The use of the on-board LNA is advised only when using passive antennas, since active antennas already have an LNA.

The GPS communication interface is serial and is connected to the MCU using the UART3 port. The board also features jumpers for powering on/off the GPS and connecting/disconnecting the GPS from the UART3 port, in case an external GPS is used. Details on these jumpers can be found on section 4.2.10.

4.2.5 XBee

The board includes a set of female headers for connecting an XBee RF transceiver module for telemetry. It is important to connect the XBee with the right orientation. Figure 4.4 shows an example of an XBee module with SMA connector plugged into the Falcon I Autopilot board. The XBee communication interface is serial and is connected to the MCU using the UART2 port.

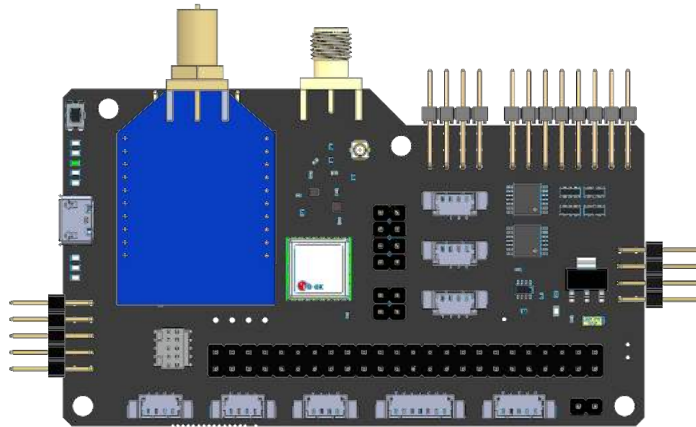


Figure 4.4: Falcon I Autopilot Board Overview with XBee connected.

4.2.6 Data-Logger

A secondary MCU based on an Atmel AVR 8-bits 16Mhz ATMEGA328P takes care of listening to the telemetry serial port (UART2) and saving the data in a micro-SD card that can be connected using the micro-SD card holder located in the bottom of the board. The MCU uses a modified version of the “OpenLog” firmware that was officially adapted by paparazziUAV to work with their system. Once the data-logging firmware is running there is no need to change any settings, as it starts running and saving data automatically after power up.

The board includes a jumper for powering on/off the data-logger. Details on this jumper can be found on section 4.2.10.

4.2.7 CAN Transceiver

The board features a Microchip MCP2551 CAN transceiver supporting 1M/s operation. The CANH and CANL pins are accessible through connector J5. Details on this connector can be found on section 4.2.9.

4.2.8 Motor/Servo Outputs (PWM)

The Falcon I Autopilot board has eight PWM outputs that can be used to control motors and servos. Outputs run through tristate buffers and each signal can be enabled/disabled using one of two user control signals. This functionality is intended for using external kill-switches for motor and servo signals.

PWM outputs and control signals are accessible through connectors J3 and J7 respectively. Details on these connectors can be found on section 4.2.9

4.2.9 Connectors

J3 Header

Figure 4.5 shows the location and pinout of the motor/servo headers. There are eight 3-pin headers, each one with GND, Power and PWM output. The Power pins are all tied together and have 4.8-5.5V range. When an Electronic Speed Controller (ESC) is connected, the power coming from it is used to power the servos.

Each of the 8 PWM outputs can be assigned to one of the two user control switches (as a motor or as a servo), as explained in 4.2.8. This is done via solder jumpers SB6-SB13. Details on these jumpers can be found on section 4.2.10.

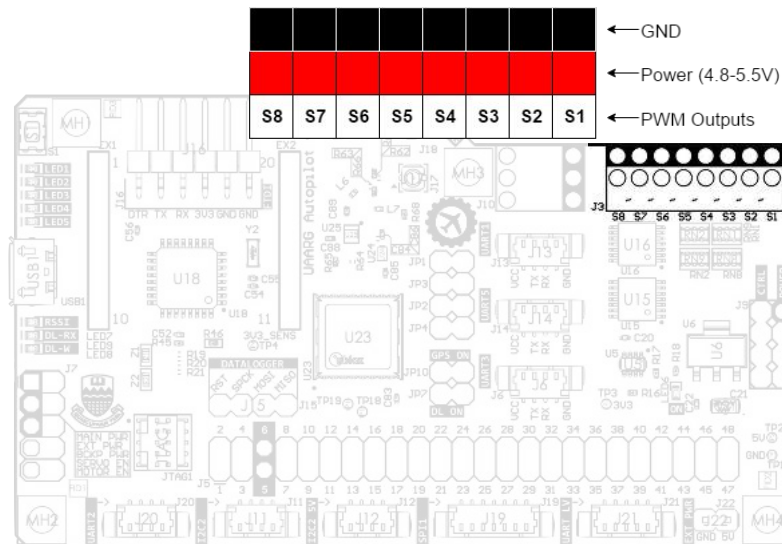


Figure 4.5: J3 Header Pinout.

J5 Header

Figure 4.6 shows the location and pinout of the 48-pin expansion header that can be used to access communication ports, GPIO, Analog inputs, etc.

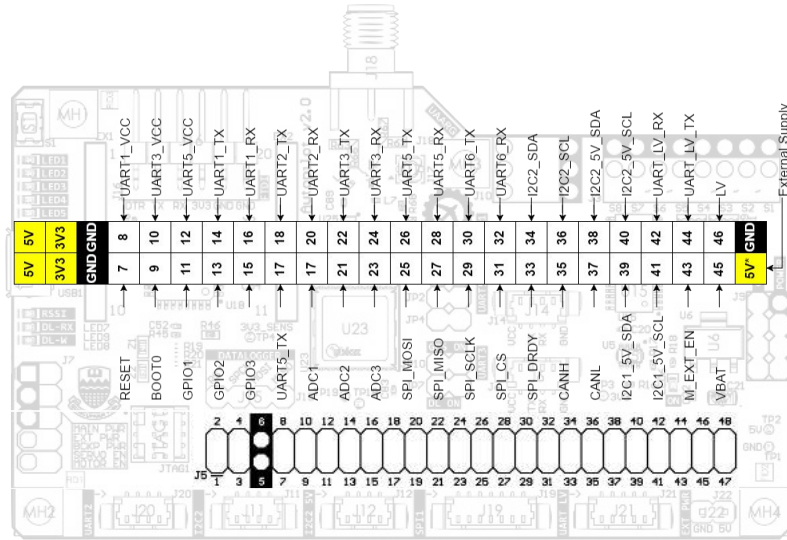


Figure 4.6: J5 Header Pinout.

J6 Header

Figure 4.7 shows the location and pinout of the pico-blade connector for UART3. This serial port can be used to connect an external GPS module. If an external GPS module is used, the on-board GPS module can be disconnected from power using jumper JP10 and the TX and RX lines can be disconnected from the MCU using jumpers JP2 and JP4. Details on these jumpers can be found on section 4.2.10.

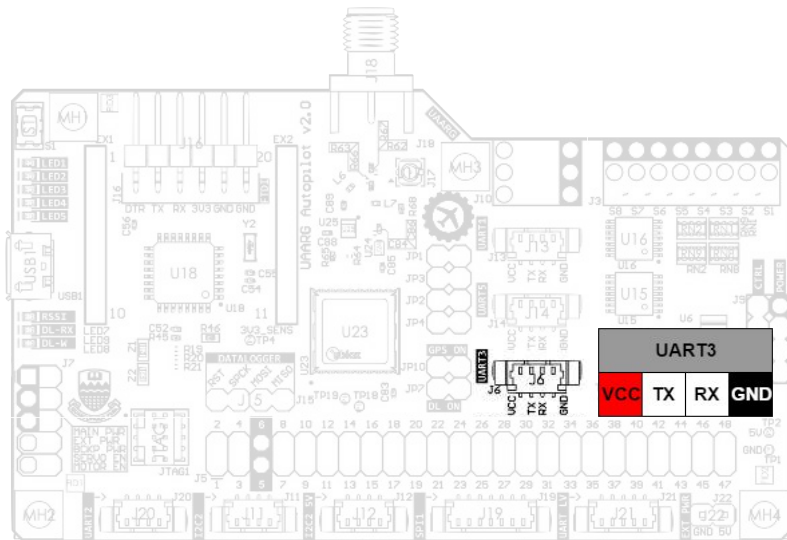


Figure 4.7: J6 Header Pinout.

J7 Header

Figure 4.8 shows the location and pinout of the user control switches. This header can also be used with jumper, but is primarily intended to be used with SPST toggle switches, each one connected between pins 1-2, 3-4, 5-6, 7-8, and 9-10.

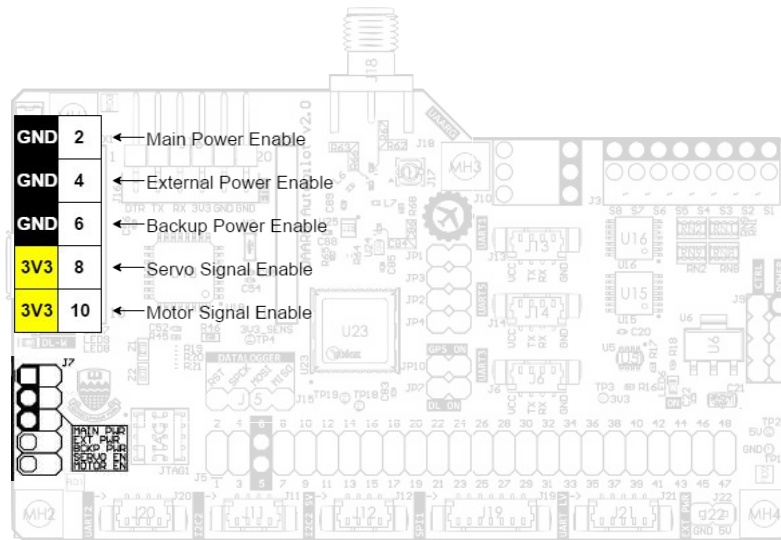


Figure 4.8: J7 Header Pinout.

From top to bottom, the first three pairs are used for enabling/disabling the main power supply, external power supply and backup power supply respectively. When the switch (or jumper) is on, those pins are shorted to GND and power is off for the corresponding function. The last two pairs are used for enabling/disabling the servo and motor signals respectively. When the switch (or jumper) is on, those pins are shorted to 3.3V, and the servo/motor signals are disabled (PWM signal disabled and output pulled-down to GND). Jumper SB6-SB13 are used to select which PWM outputs are assigned to motors and servos. Details on these jumpers can be found on section 4.2.10.

J9 Header

Figure 4.9 shows the location and pinout of the power header. This header is used for powering the board, and also carries external and backup power supplies as well as power enable signals. Table 4.1 shows a description of each pin of this header.

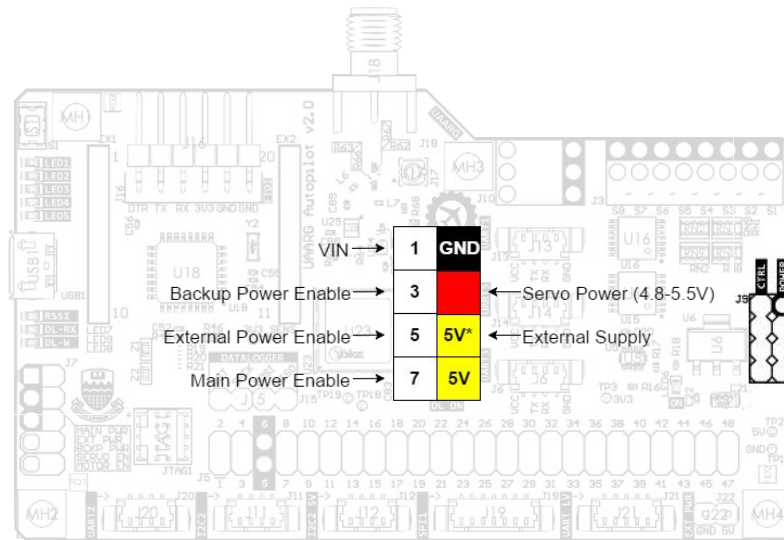


Figure 4.9: J9 Header Pinout.

Table 4.1: J9 Header Pinout Description.

| Pin | Signal | Description |
|-----|-----------------------|--|
| 1 | VIN | Battery voltage for voltage measurement |
| 2 | GND | Ground |
| 3 | Backup Power Enable | Enable signal for backup power |
| 4 | Servo Power | Backup power for servos |
| 5 | External Power Enable | Enable signal for external power |
| 6 | External Supply | External power (5V) for secondary system |
| 7 | Main Power Enable | Enable signal for main power |
| 8 | 5V | Main power (5V) |

J10 Header

Header J10 includes 3 communication ports: 1 x I2C and 2 x UART.

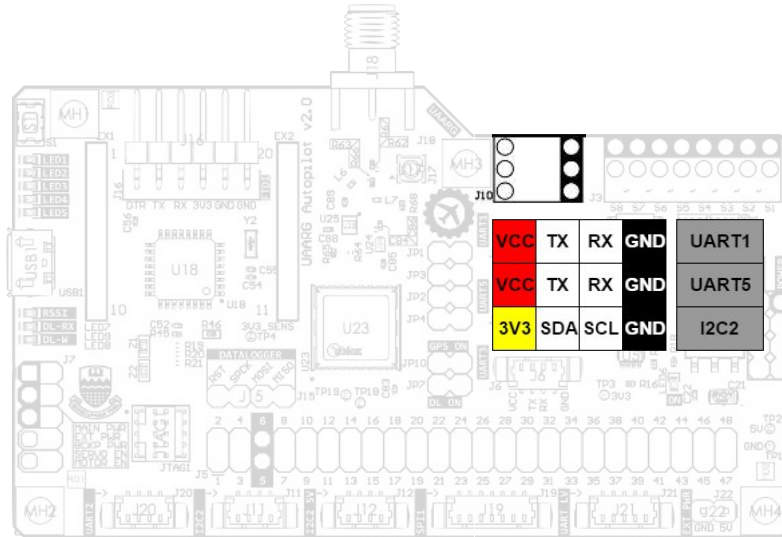


Figure 4.10: J10 Header Pinout.

J11 Header

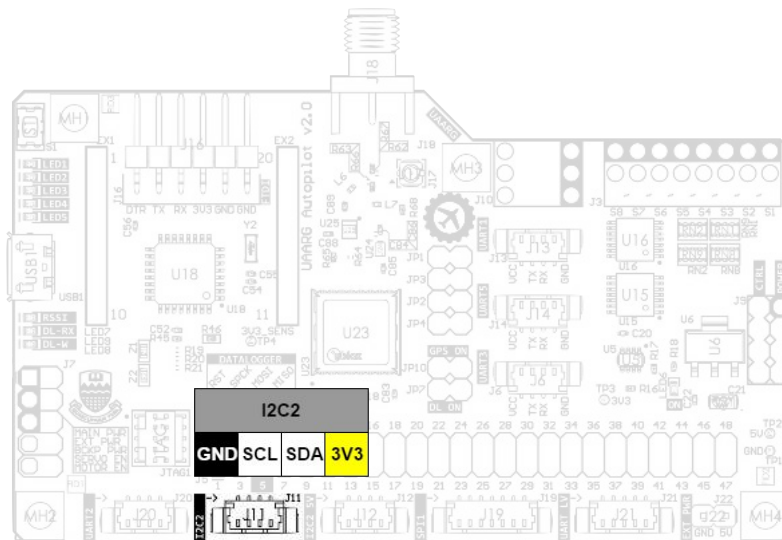


Figure 4.11: J11 Header Pinout.

J12 Header

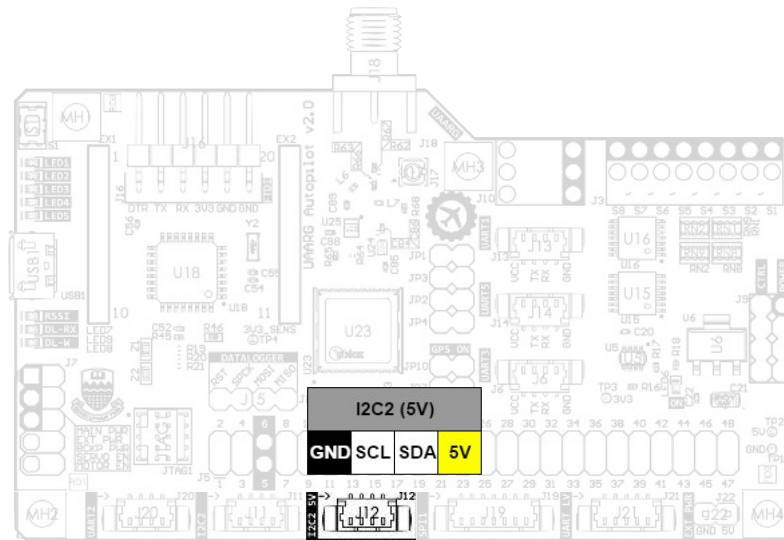


Figure 4.12: J12 Header Pinout.

J13 Header

Figure 4.13 shows the location and pinout of the pico-blade connector for UART1. This serial port is used to connect an RC receiver.

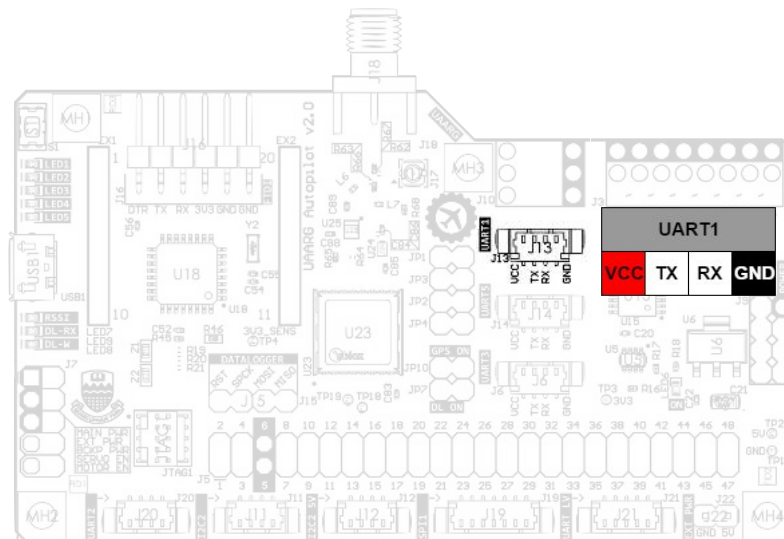


Figure 4.13: J13 Header Pinout.

J14 Header

Figure 4.14 shows the location and pinout of the pico-blade connector for UART5. This serial port is used to connect an RC receiver.

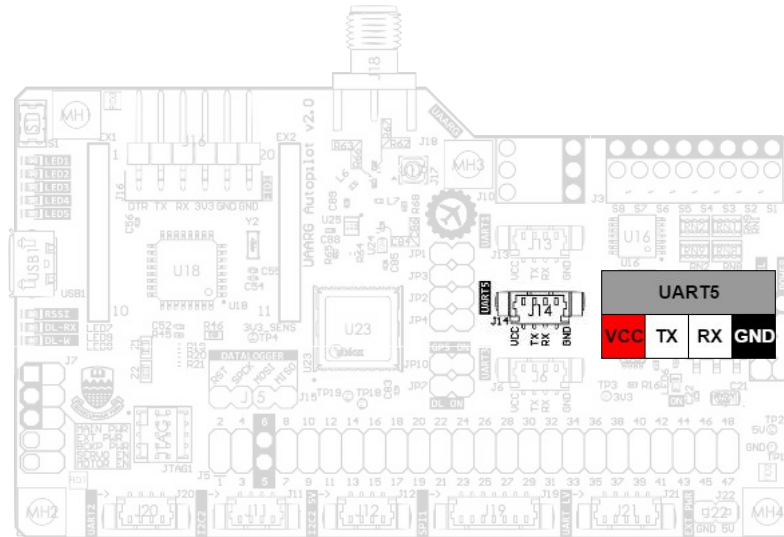


Figure 4.14: J14 Header Pinout.

J15 Header

Figure 4.15 shows the location and pinout of the ISP connector used for programming the data-logger MCU ATMEGA328P.

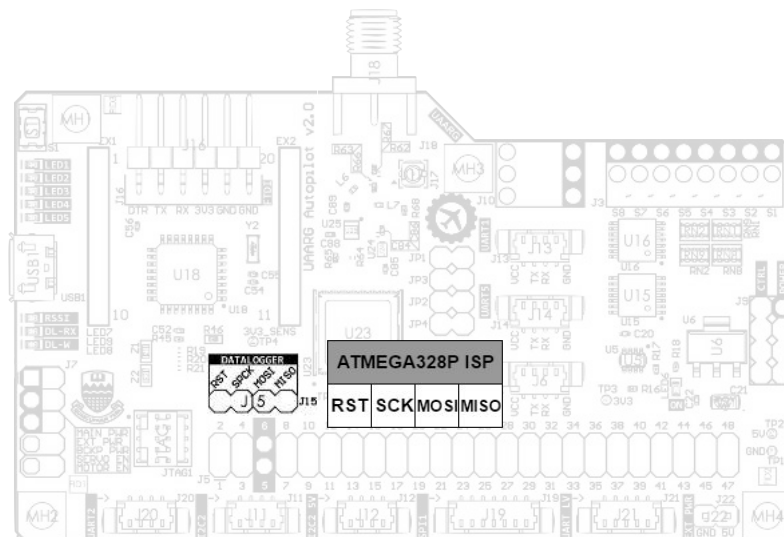


Figure 4.15: J15 Header Pinout.

J16 Header

Figure 4.16 shows the location and pinout of the FTDI connector used for communicating with the data-logger MCU ATMEGA328P.

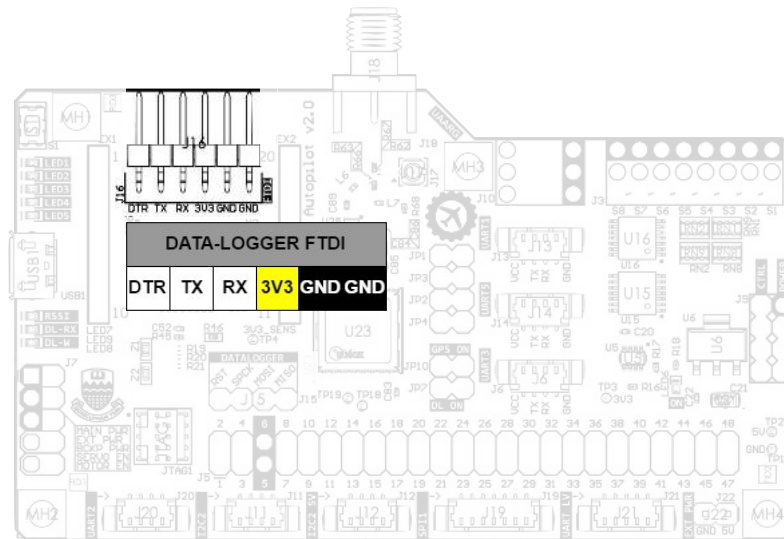


Figure 4.16: J16 Header Pinout.

J17 Header

Figure 4.17 shows the location of the uFL connector for the GPS antenna. This connector can be enabled setting the jumper resistor R62 instead of R67.

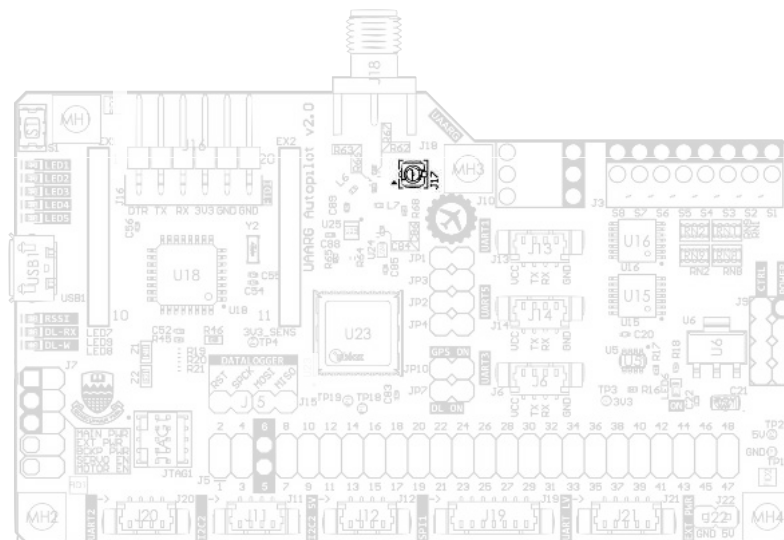


Figure 4.17: J17 Header Pinout.

J18 Header

Figure 4.18 shows the location of the SMA connector for the GPS antenna. This connector can be enabled setting the jumper resistor R67 instead of R62.

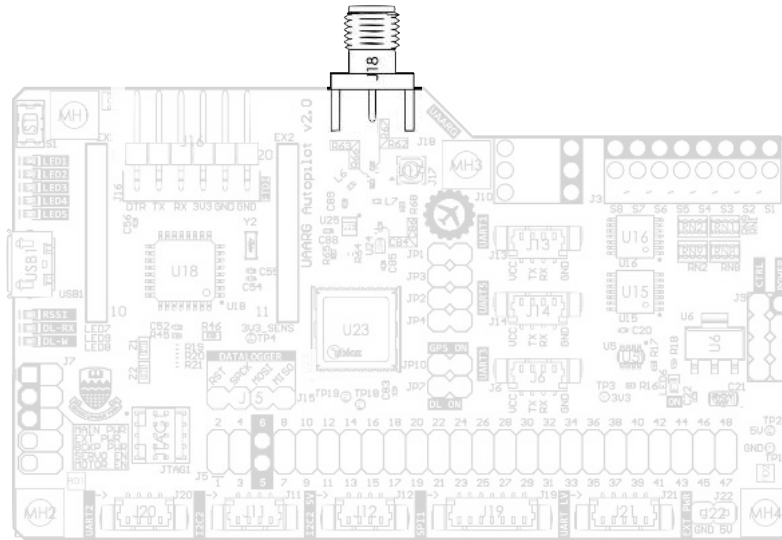


Figure 4.18: J18 Header Pinout.

J19 Header

Figure 4.19 shows the location and pinout of the SPI interface connector.

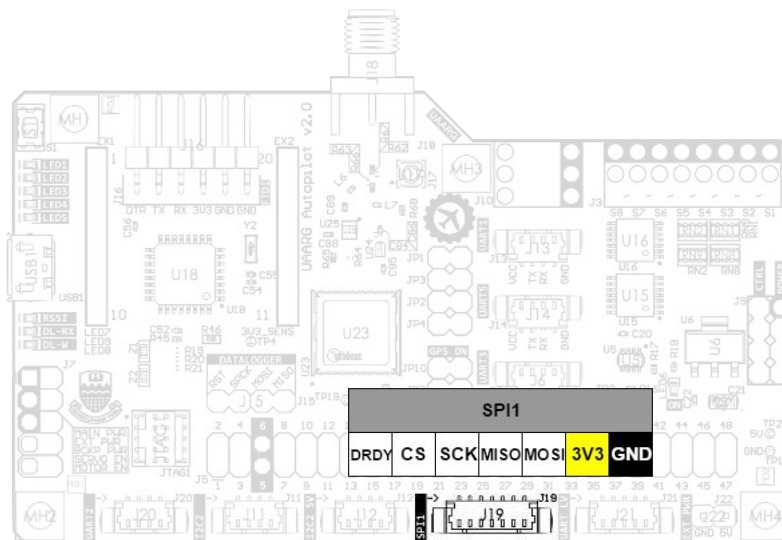


Figure 4.19: J19 Header Pinout.

J20 Header

Figure 4.20 shows the location and pinout of the UART2 connector. This serial port is connected to the XBee module used for telemetry. If an external telemetry module is used, it can be connected to this port while leaving the XBee sockets empty.

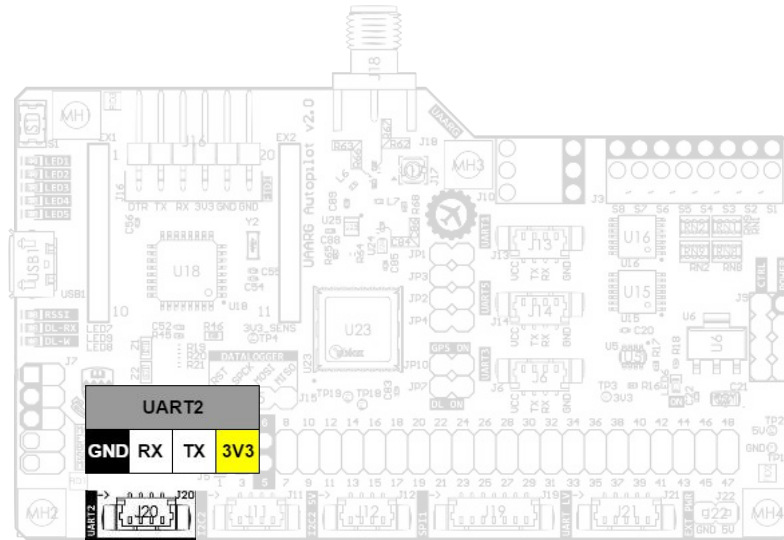


Figure 4.20: J20 Header Pinout.

J21 Header

Figure 4.21 shows the location and pinout of the UART_LV connector. This UART port has a voltage level shifter and can be used for communication with an external system that uses a different voltage level (e.g. ODROID Linux mini-PC using 1.8V logic).

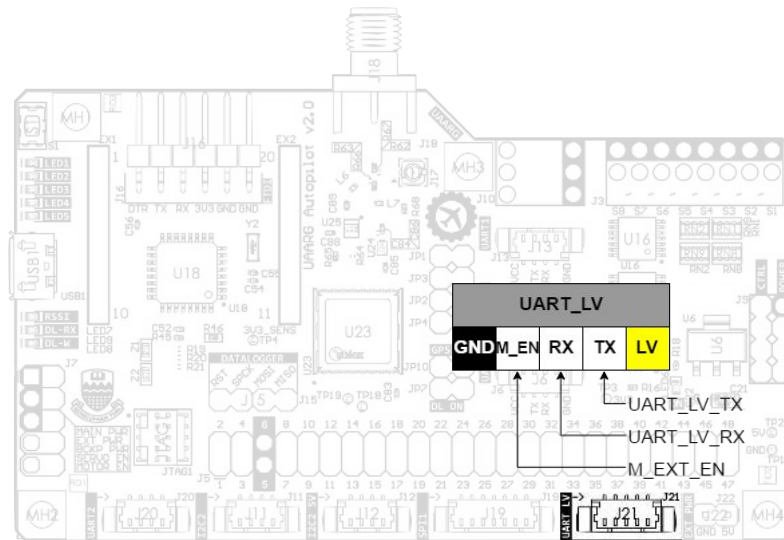


Figure 4.21: J21 Header Pinout.

This serial port can be connected to UART2 (currently used for the XBee telemetry module) in case the secondary system only wants to listen to telemetry information; or it can be connected to UART6, which can be used as a dedicated serial link. This change can be done using SB1 and SB2 solder jumpers. Details on these jumpers can be found on section 4.2.10.

J22 Header

Figure 4.22 shows the location and pinout of the External Power connector. This connector provides power to an external system. Power comes from pin 6 in header J9.

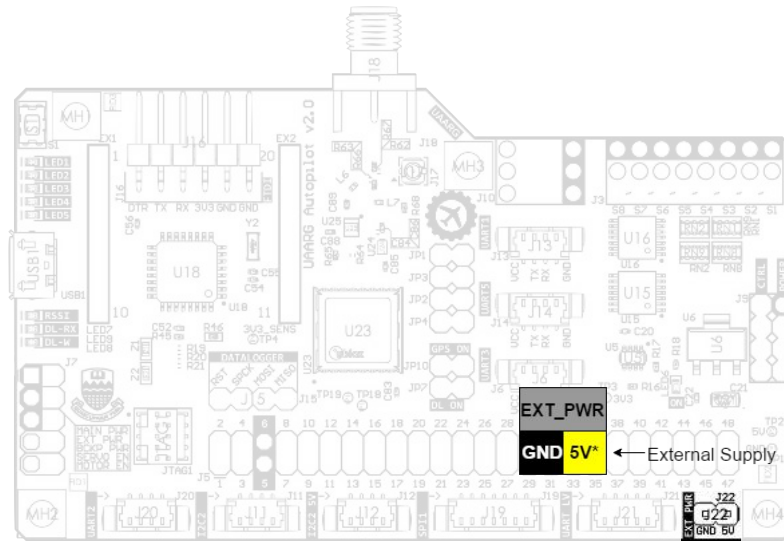


Figure 4.22: J22 Header Pinout.

JTAG1 Header

Figure 4.23 shows the location of the JTAG connector used for programming the STM32F4 MCU.

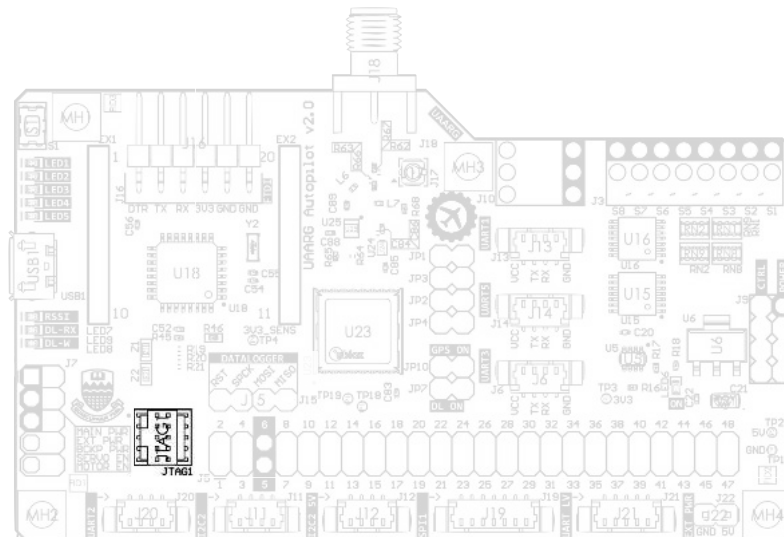


Figure 4.23: JTAG1 Header Pinout.

USB1 Header

Figure 4.24 shows the location of the micro-USB connector.

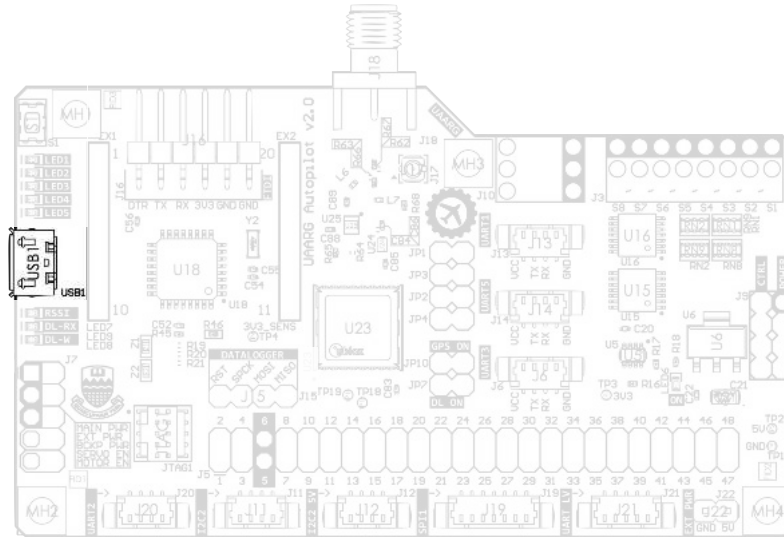


Figure 4.24: USB1 Header Pinout.

EX1, EX2 Headers

Figure 4.25 shows the location of the XBee socket connectors used for plugging the XBee module. Refer to section 4.2.5 for correct orientation of the XBee module.

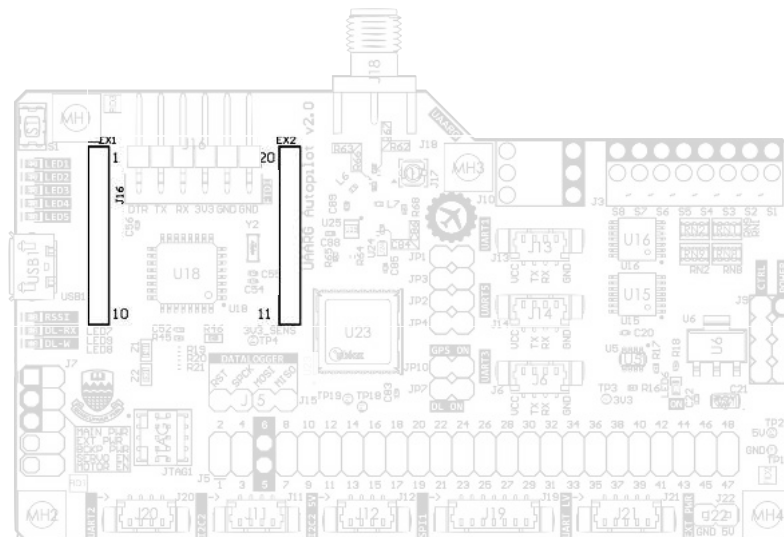


Figure 4.25: EX1, EX2 Headers Pinout.

4.2.10 Jumpers

Solder Jumper SB1-SB13

Figure 4.26 shows the location of the solder jumpers SB1 to SB13 on the bottom side of the Falcon I Autopilot board, and Figure 4.27 shows the three sub-groups of solder jumpers. All solder jumpers have the same 3-pad footprint, where the middle pad is the common pin and the two side pads are the options. To make a connection, place a solder bridge between the middle pad and one of the side pads. Some jumpers come already with a default connection by means of a small exposed track (no solder mask) joining the middle pad with one of the side pads. If the default option is no desired, the track needs to be cut so as to disconnect the pads.



Figure 4.26: Location of all solder jumpers.



Figure 4.27: Solder jumper sub-groups.

Table 4.2 shows the description for each solder jumper and the two options. The location reference for the options (Left, Right, Top, Bottom) is based on the orientation of the jumpers shown in Figure 4.27. Note that SB4 and SB5 have a default option (option 1) already selected by means of a trace connection, so there is no need to place a solder bridge if this option is desired. If option 2 is desired, the trace must be carefully cut using a sharp blade (e.g. scalpel knife) before placing the solder bridge.

Warning: For SB4 and SB5, do not solder bridge option 2 without removing option 1 default connection. Powering the boards like this might damage it.

Table 4.2: Solder jumpers descriptions.

| SB | Option 1 | Option 2 | Description |
|----|----------------------|----------------------|--|
| 1 | (Left) UART6_TX | (Right) UART2_TX | Selects UART (Low Voltage) port (TX pin) |
| 2 | (Left) UART2_RX | (Right) UART6_RX | Selects UART (Low Voltage) port (RX pin) |
| 3 | (Top) 3.3V | (Bottom) 5V | UART3 Power Rail |
| 4 | (Top) 3.3V (default) | (Bottom) 5V | UART1 Power Rail |
| 5 | (Top) 3.3V (default) | (Bottom) 5V | UART5 Power Rail |
| 6 | (Top) Servo Group | (Bottom) Motor Group | PWM signal enable/disable (Output 1) |
| 7 | (Top) Servo Group | (Bottom) Motor Group | PWM signal enable/disable (Output 2) |
| 8 | (Top) Servo Group | (Bottom) Motor Group | PWM signal enable/disable (Output 3) |
| 9 | (Top) Servo Group | (Bottom) Motor Group | PWM signal enable/disable (Output 4) |
| 10 | (Top) Servo Group | (Bottom) Motor Group | PWM signal enable/disable (Output 5) |
| 11 | (Top) Servo Group | (Bottom) Motor Group | PWM signal enable/disable (Output 6) |
| 12 | (Top) Servo Group | (Bottom) Motor Group | PWM signal enable/disable (Output 7) |
| 13 | (Top) Servo Group | (Bottom) Motor Group | PWM signal enable/disable (Output 8) |

GPS Signal Jumpers

Figure 4.28 shows the location of the jumpers used for configuring the GPS signal circuitry. There are three GPS signal setup jumpers used for configuring the signal path. Each jumper consists of an 0402 capacitor/resistor that can be soldered vertically or horizontally. The orientation of these components defines the route of the signal. Table 4.3 shows the description for each setup based on these jumpers.

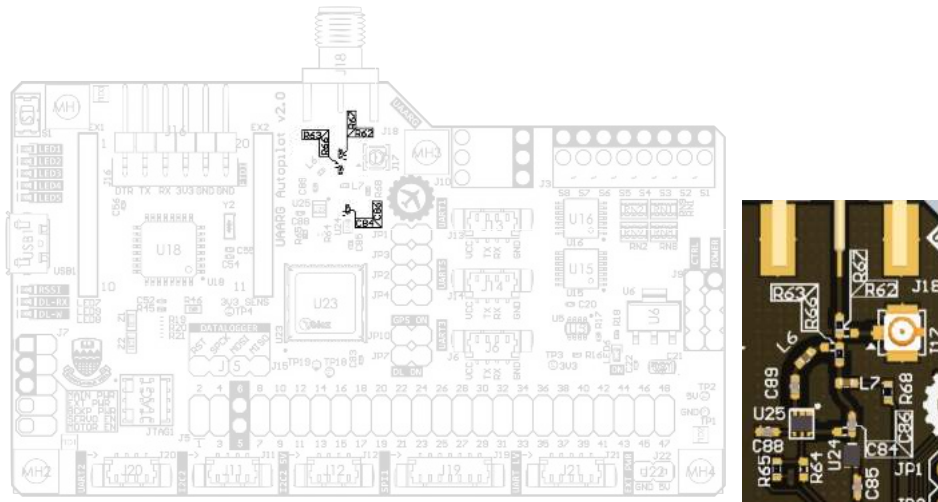


Figure 4.28: Location of GPS signal jumpers.

Table 4.3: GPS signal jumpers descriptions.

| Setup | Description |
|-------------------|-------------------------------|
| C84 On and R63 On | On-board LNA enabled |
| C86 On and R66 On | On-board LNA disabled |
| R62 On | uFL antenna connector enabled |
| R67 On | SMS antenna connector enabled |

GPS and Data-logger Power Jumpers

Figure 4.29 shows the location of the two power jumpers. When JP7 is closed the data-logger is powered and when JP10 is closed the GPS is powered.

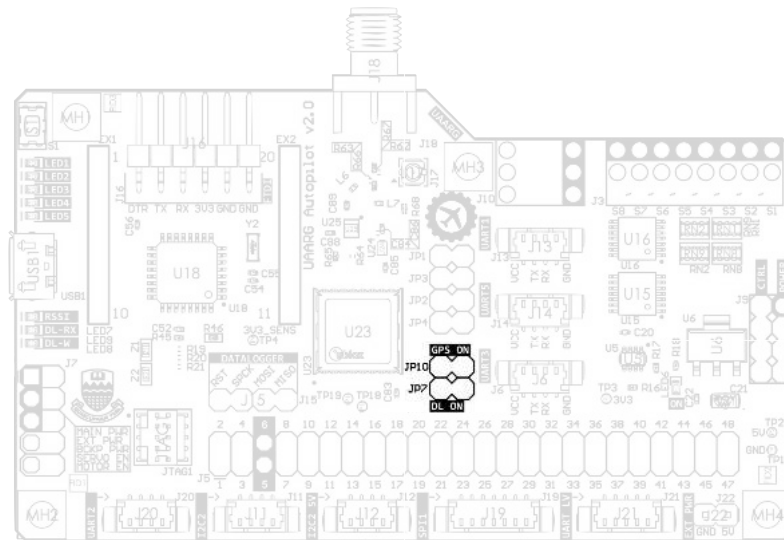


Figure 4.29: Location of power jumpers.

GPS Serial Jumpers

Figure 4.30 shows the location of the GPS serial jumpers. These jumpers form a “T” connection for the UART3 port between the on-board GPS module, MCU and J6 header. JP1 and JP3 connect the RX and TX lines respectively of the on-board GPS module to header J6. JP2 and JP4 connect the TX and RX lines respectively of the MCU to header J6.

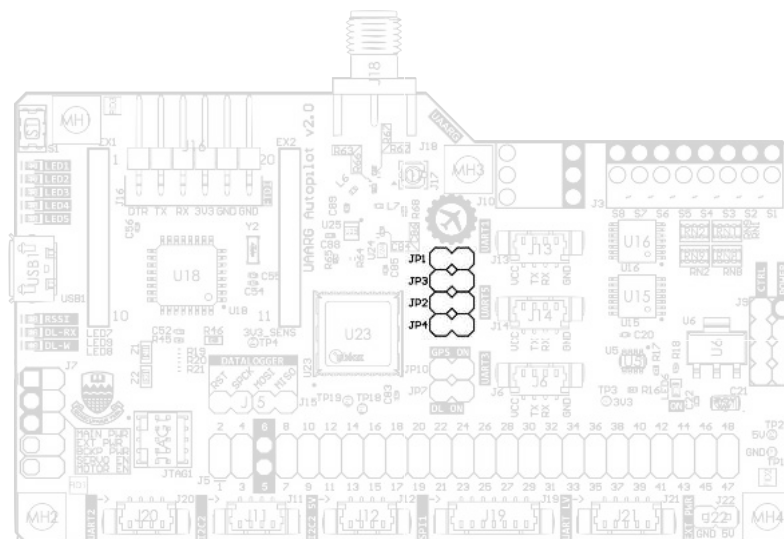


Figure 4.30: Location of GPS serial jumpers.

During normal operation (using the on-board GPS), all 4 jumpers are closed. There are other two cases:

1. JP1 and JP3 can be left open for using an external GPS module connected directly to J6.
2. JP2 and JP4 can be left open for talking directly to the GPS module from an external system through J6. An example of this is connecting to the GPS from a PC in order to configure it.

4.3 Board Pictures

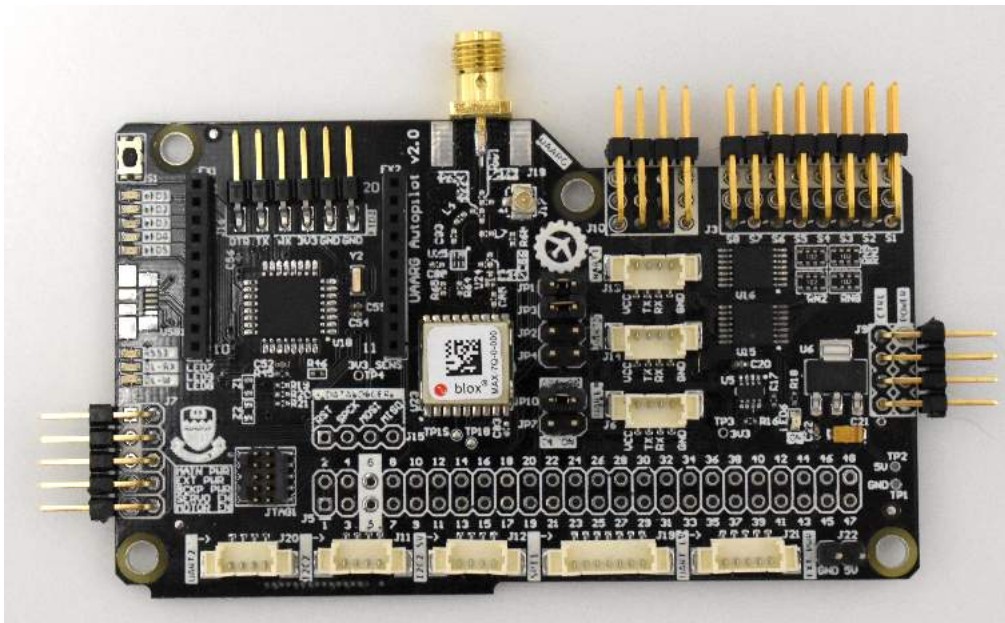


Figure 4.31: Falcon I Autopilot Board (Top).

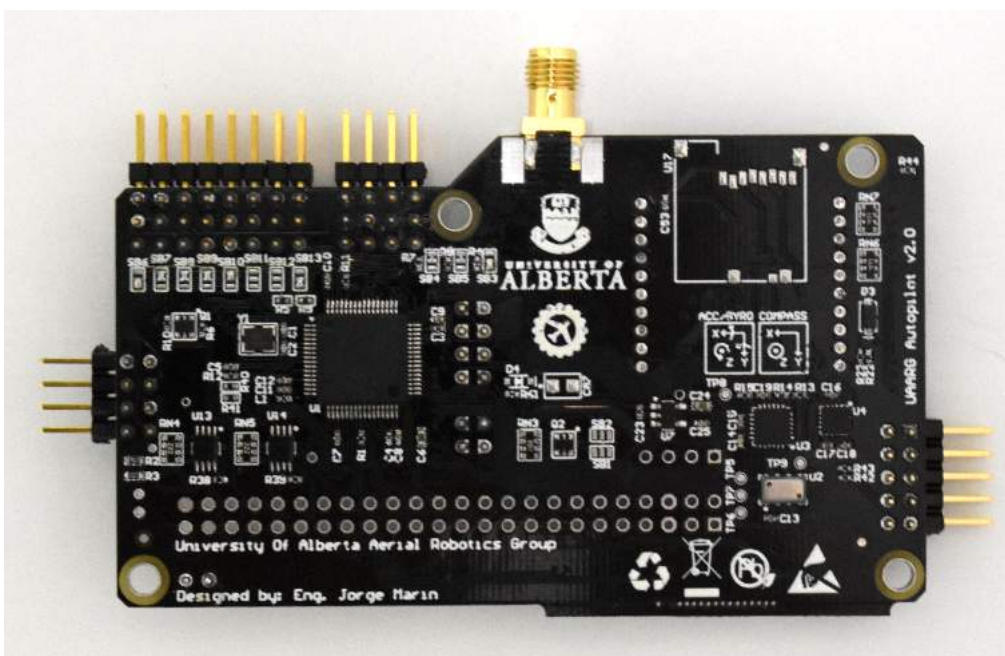


Figure 4.32: Falcon I Autopilot Board (Bottom).

4.4 Autopilot Board Schematics

This section contains the following schematics:

- Index
- UAARG Autopilot
- Connectors
- MCU
- IMU
- GPS
- CAN, JTAG, LDO, USB
- Telemetry, I2C
- Switches, UI
- Data Logger
- Power
- Main Power
- Backup Power
- Notes
- Documentation
- Revision History

Project Title: UAARG Autopilot.PrjPcb
Revision: 2.0 Date: 20-DEC-2015

| Page | Name |
|------|---------------------|
| 1 | Index |
| 2 | UAARG Autopilot |
| 3 | MCU |
| 4 | IMU |
| 5 | GPS |
| 6 | CAN, JTAG, LDO, USB |
| 7 | Telemetry, I2C |
| 8 | Switches, UI |
| 9 | Data Logger |
| 10 | Power |
| 11 | Main Power |
| 12 | Backup Power |
| 13 | Notes |
| 14 | Documentation |
| 15 | Revision History |
| 16 | |
| 17 | |
| 18 | |
| 19 | |
| 20 | |
| 21 | |
| 22 | |
| 23 | |
| 24 | |
| 25 | |
| 26 | |
| 27 | |
| 28 | |

Blocks

U UAARG Autopilot
UAARG Autopilot.SchDoc

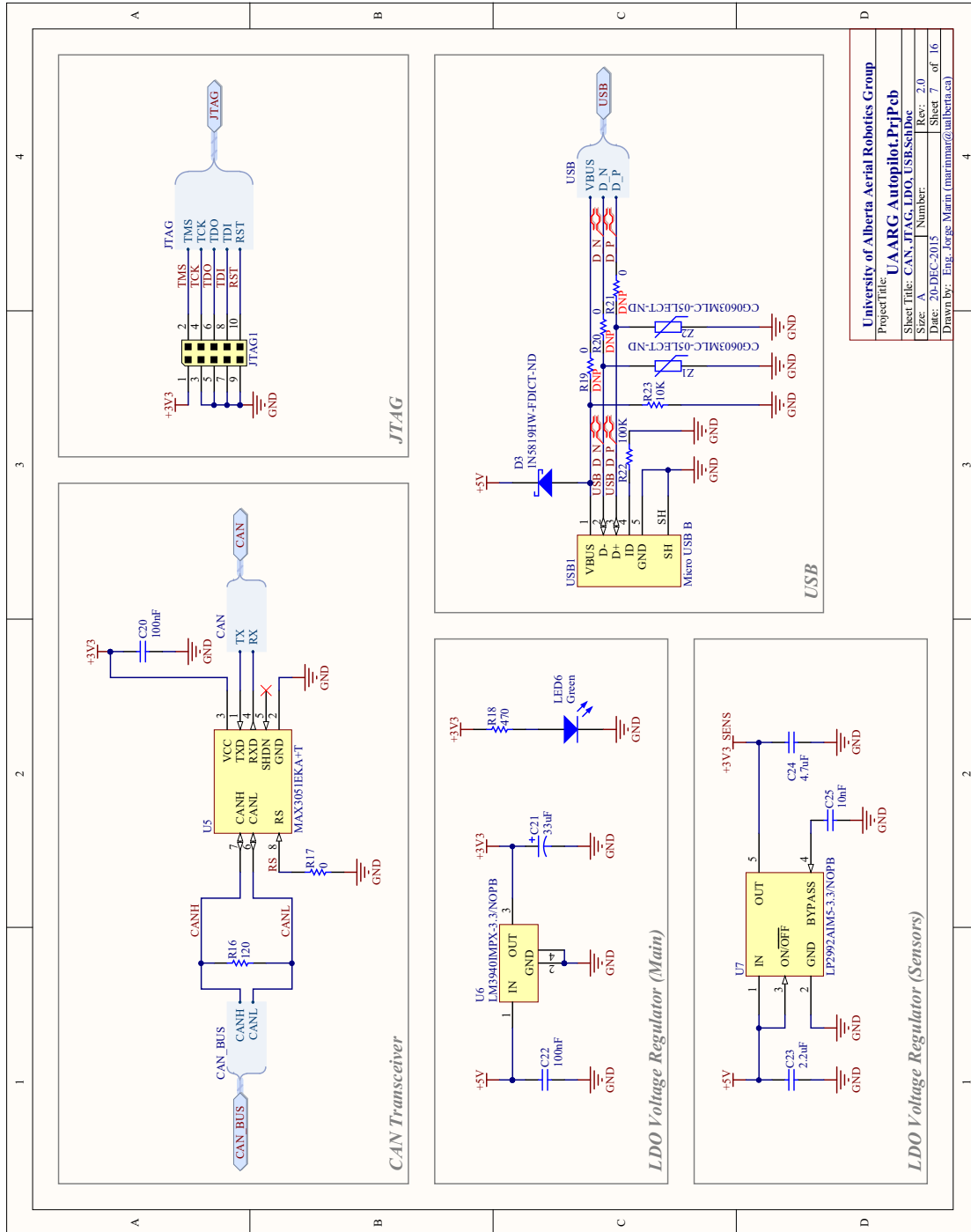
U Power
Power.SchDoc

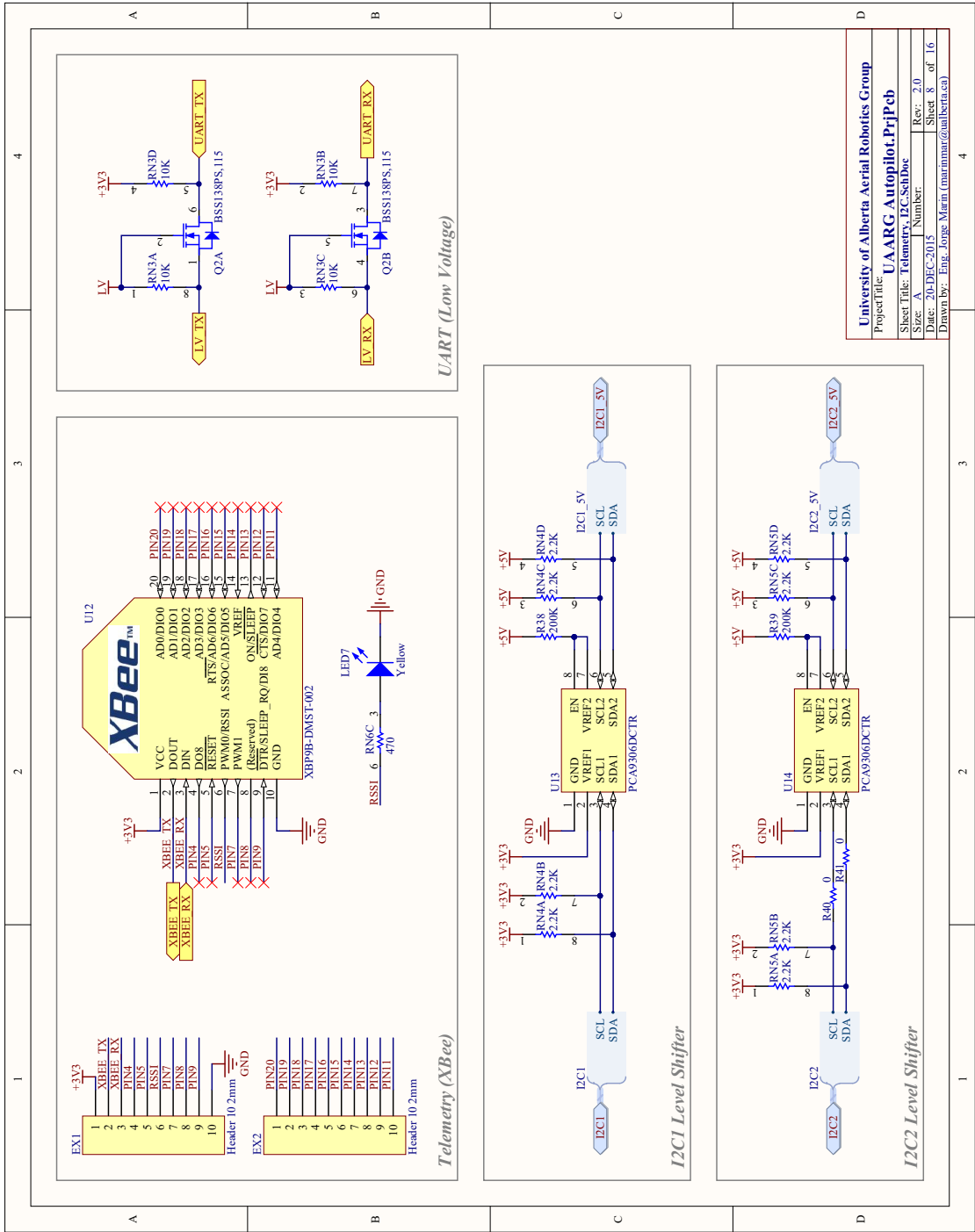
U Notes
Notes.SchDoc

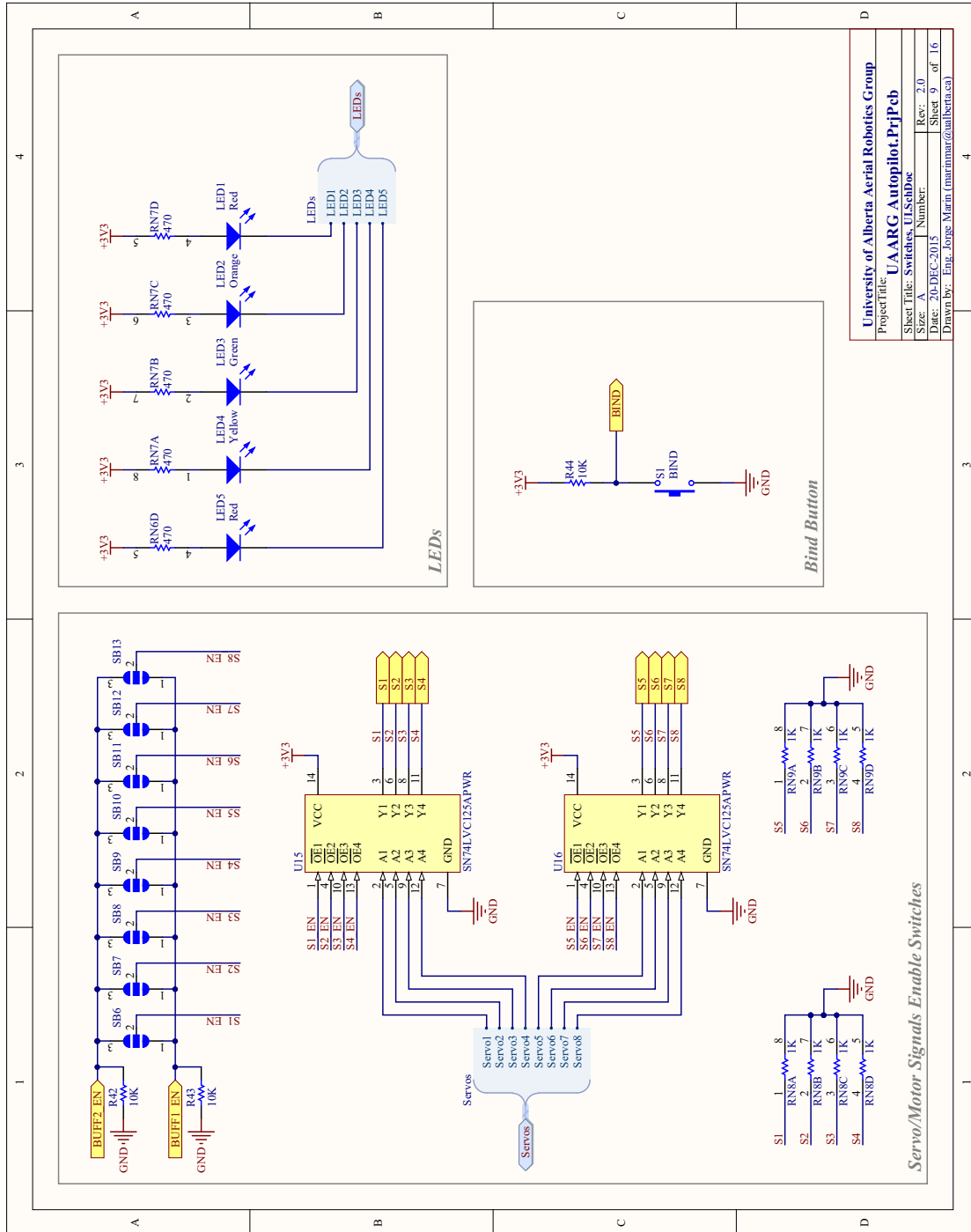
U Documentation
Documentation.SchDoc

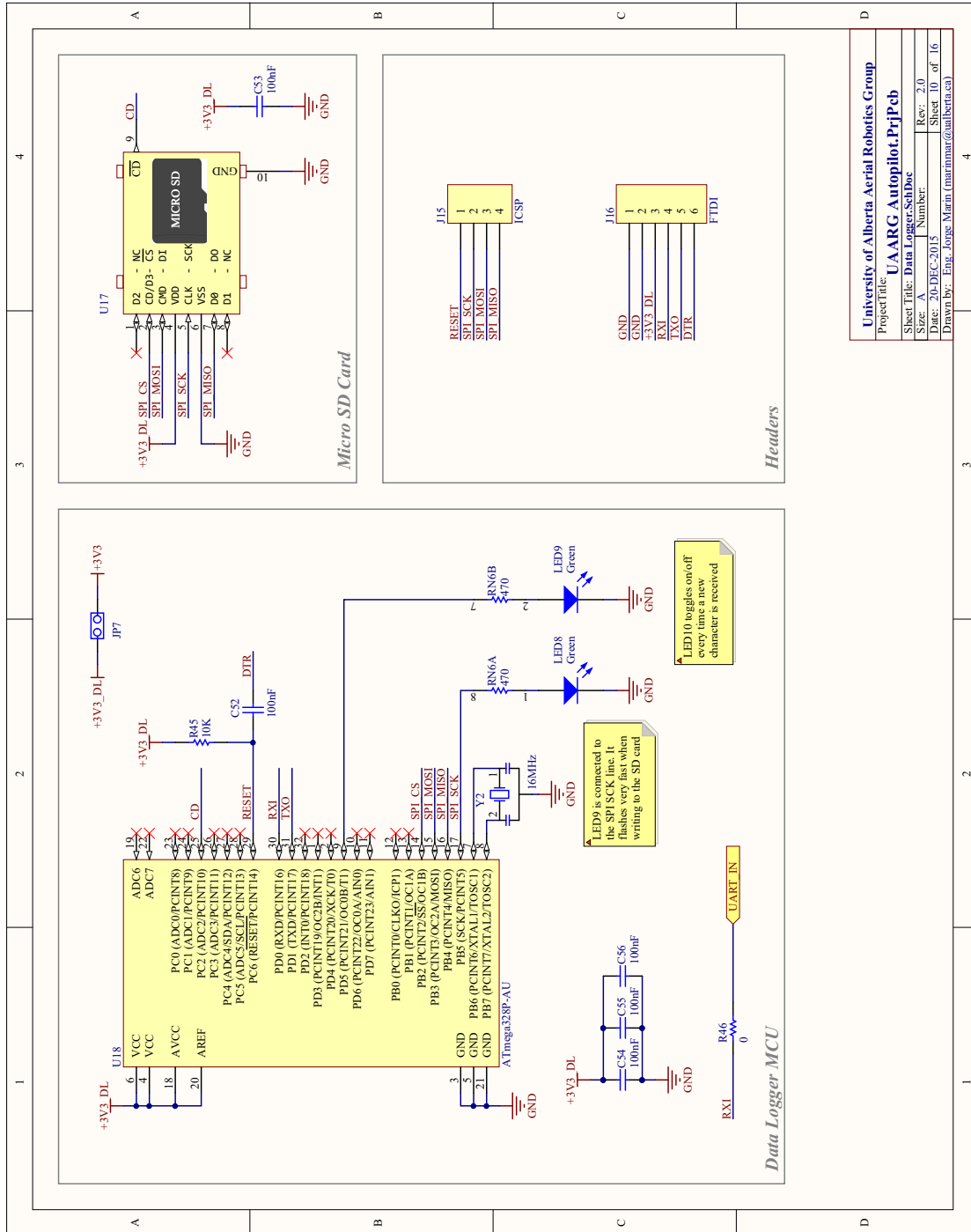
U Revision History
Revision History.SchDoc

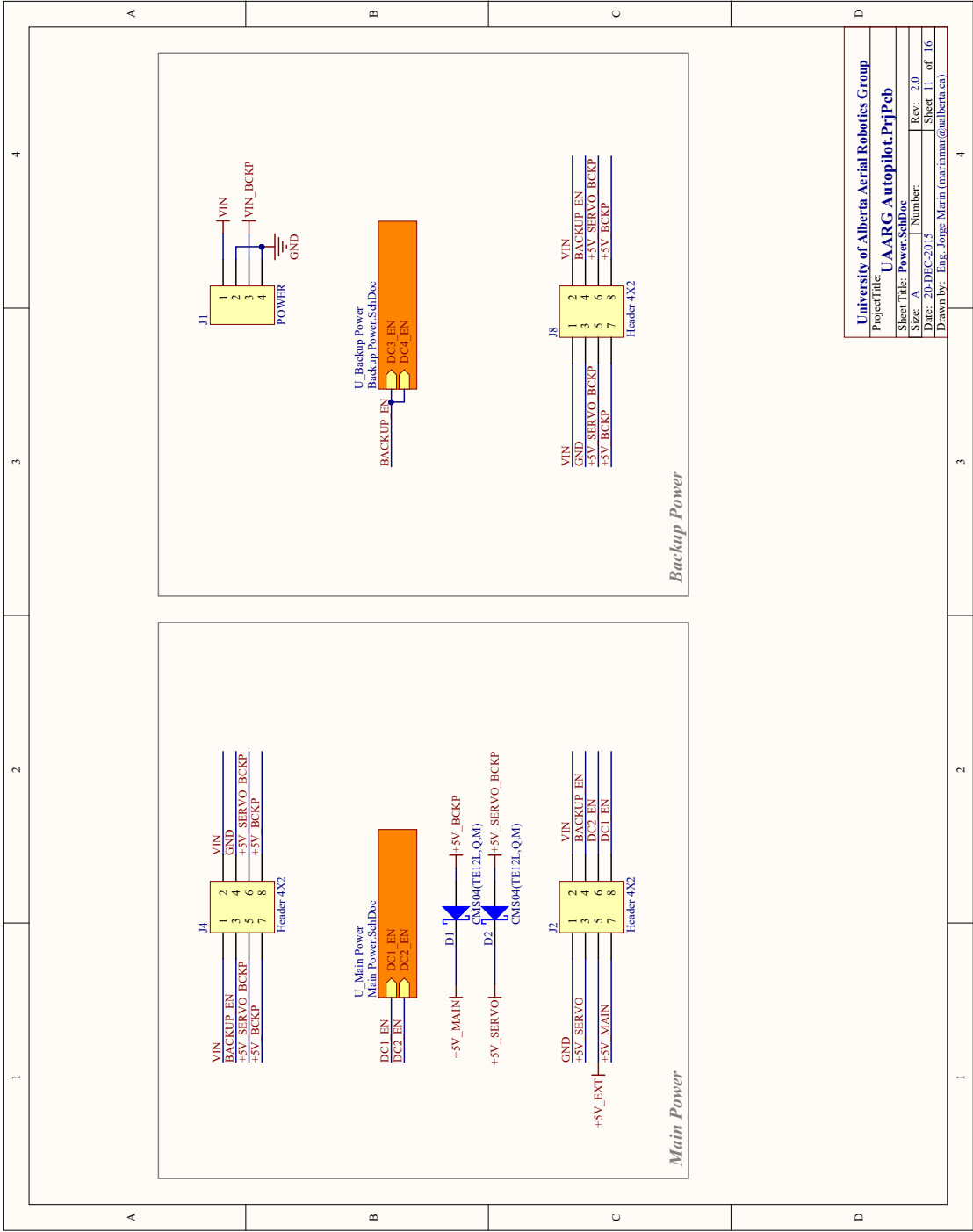
| | | | |
|---|--------------|---|---------------|
| University of Alberta Aerial Robotics Group | | | |
| Project Title: UAARG Autopilot.PrjPcb | | | |
| Sheet Title: | Index.SchDoc | Rev: | 2.0 |
| Size: | A | Number: | Sheet 1 of 16 |
| Date: | 20-DEC-2015 | Drawn by: Eng. Jorge Marin (marinmar@ualberta.ca) | |

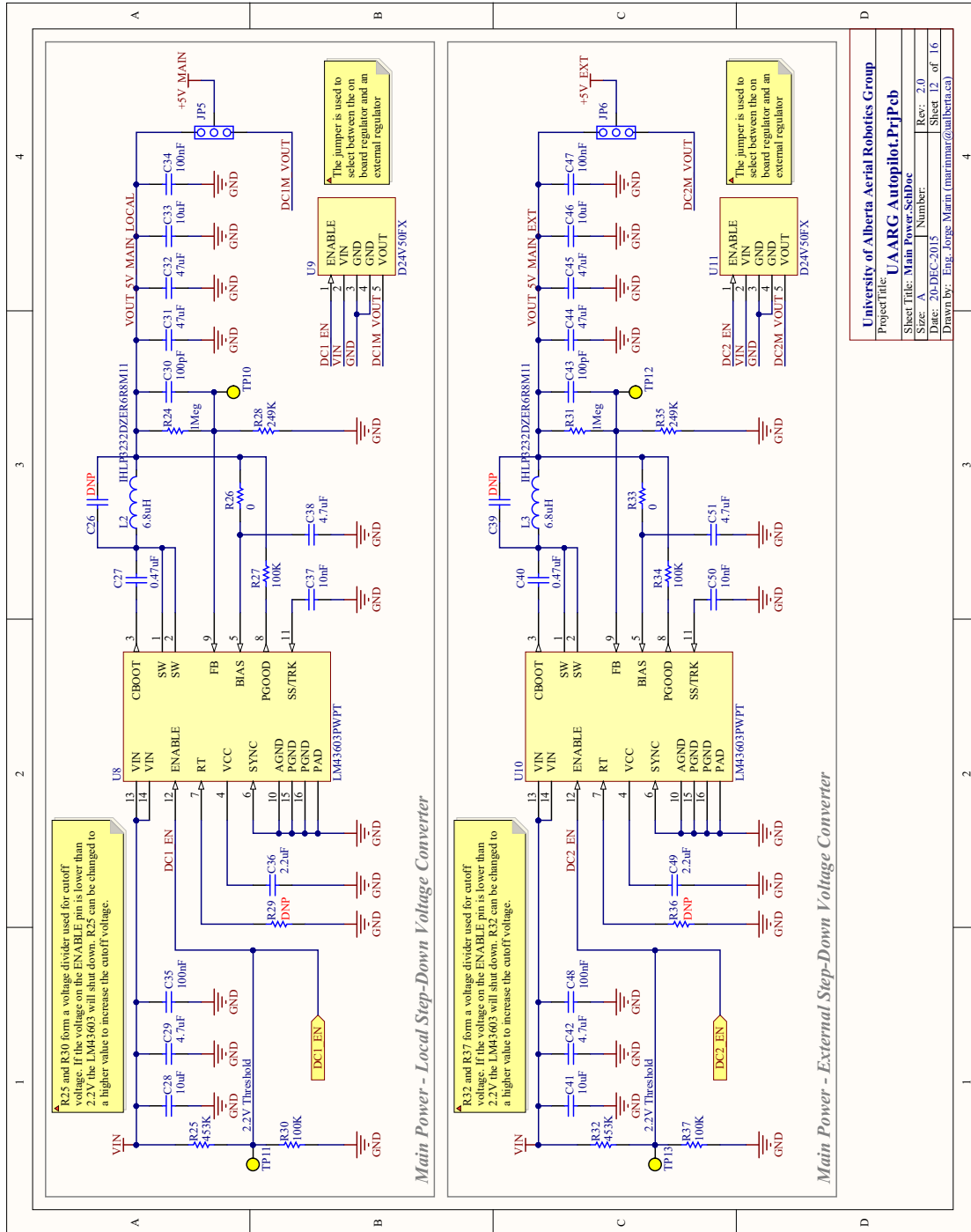


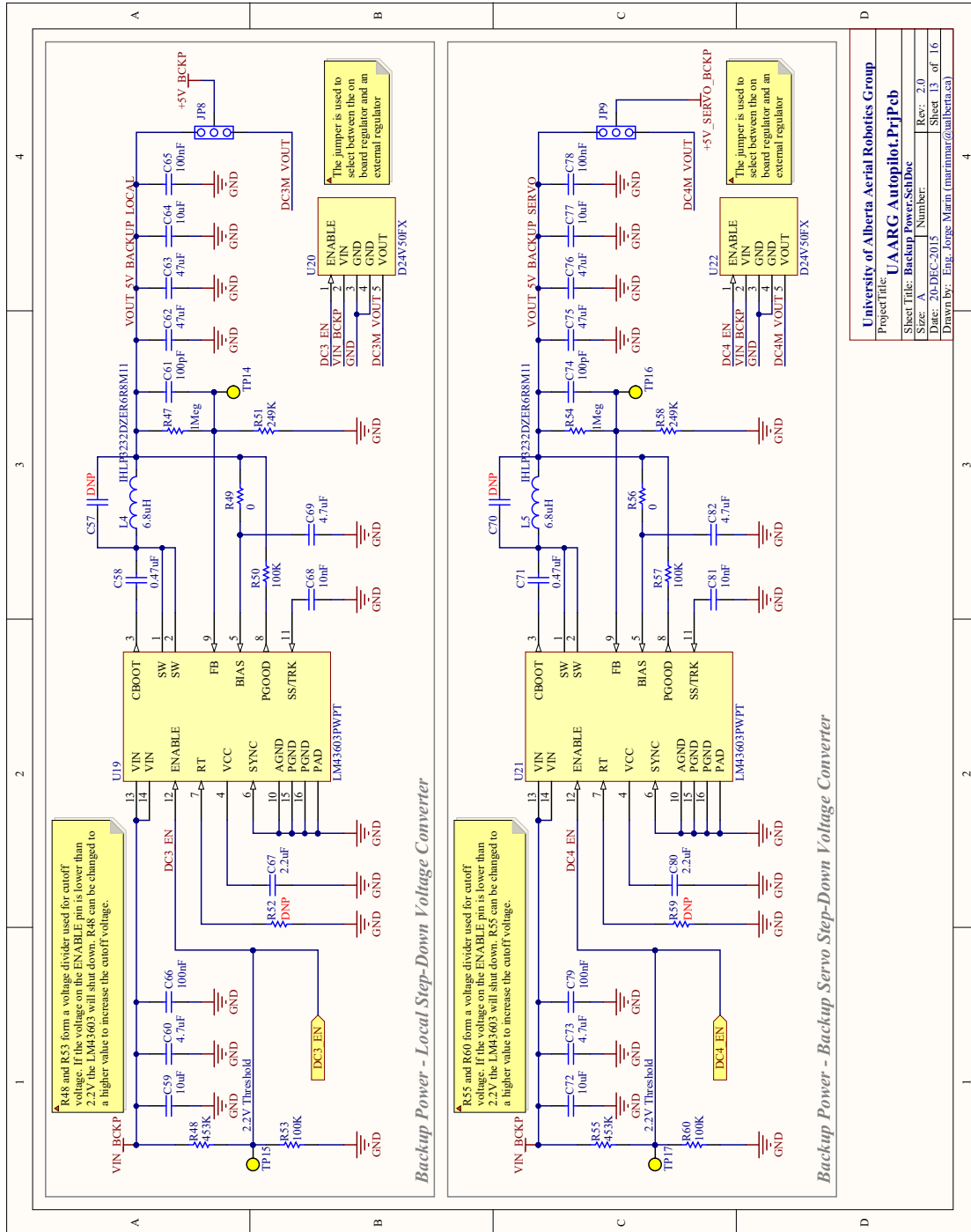












| 1 | | 2 | | 3 | | 4 | | | | | | | | | | | | | | | | | |
|---|---|----------|-------------|---|--|---|--|----------|-------------|-----|---|--|--|---------|-------------|---|---|---|---|---|---|-----------------------------|--|
| A | | B | | C | | D | | | | | | | | | | | | | | | | | |
| <div><div>General Notes</div><div>General notes relating to the design.</div><table><tr><th>Note No.</th><th>Description</th></tr><tr><td></td><td></td></tr></table></div> | | Note No. | Description | | | <div><div>PCB Layout Requirements</div><div>Layout notes referring to specific components or group of components are indicated on the schematics by the note number, enclosed in braces, adjacent to the component. Eg [1].</div><table><tr><th>[Number]</th><th>Description</th></tr><tr><td>[1]</td><td>GPS antenna traces require 50ohm impedance.</td></tr></table></div> | | [Number] | Description | [1] | GPS antenna traces require 50ohm impedance. | <div><div>PCB Assembly Variations</div><div>List of assembly variations. Variants are designated with a letter starting from A. The description shows the Variant name in brackets and then any comments.</div><table><tr><th>Variant</th><th>Description</th></tr><tr><td>A</td><td>[w/o headers] All SMT components soldered. Through-hole headers are not included.</td></tr><tr><td>B</td><td>[w/ headers] All SMT components soldered, including through-hole headers.</td></tr><tr><td>C</td><td>[Assembled] All components are soldered and external components are plugged. Fully assembled board.</td></tr></table></div> | | Variant | Description | A | [w/o headers] All SMT components soldered. Through-hole headers are not included. | B | [w/ headers] All SMT components soldered, including through-hole headers. | C | [Assembled] All components are soldered and external components are plugged. Fully assembled board. | <div><div>Notes</div></div> | |
| Note No. | Description | | | | | | | | | | | | | | | | | | | | | | |
| | | | | | | | | | | | | | | | | | | | | | | | |
| [Number] | Description | | | | | | | | | | | | | | | | | | | | | | |
| [1] | GPS antenna traces require 50ohm impedance. | | | | | | | | | | | | | | | | | | | | | | |
| Variant | Description | | | | | | | | | | | | | | | | | | | | | | |
| A | [w/o headers] All SMT components soldered. Through-hole headers are not included. | | | | | | | | | | | | | | | | | | | | | | |
| B | [w/ headers] All SMT components soldered, including through-hole headers. | | | | | | | | | | | | | | | | | | | | | | |
| C | [Assembled] All components are soldered and external components are plugged. Fully assembled board. | | | | | | | | | | | | | | | | | | | | | | |
| A | | B | | C | | D | | | | | | | | | | | | | | | | | |
| 1 | | 2 | | 3 | | 4 | | | | | | | | | | | | | | | | | |
| A | | B | | C | | D | | | | | | | | | | | | | | | | | |
| | | | | | | <div>Sheet Title: Notes.SchDoc</div> <div>Project Title: UARG Autopilot.PrjPcb</div> <div>Company: UARG Autopilot.PrjPcb</div> <div>Size: A</div> <div>Date: 20-Dec-2015</div> <div>Drawn by: Eng. Jorge Marin (marinmur@ualberta.ca)</div> <div>Rev: 2.0</div> <div>Sheet 14 of 16</div> | | | | | | | | | | | | | | | | | |

| | | | | | | | |
|--|--|-----------------------|--|------------|--|---------------------------------------|--|
| 1 | | 2 | | 3 | | 4 | |
| A | | B | | C | | D | |
| SPI SLAVES AND "CHIP SELECT" PIN MAPPING | | | | | | | |
| NAME | | PERIPHERAL | | MCU CS PIN | | | |
| SPI2 | | MPU-6000 | | PB12 | | | |
| | | MSS611-01BA03 | | PC13 | | | |
| UART PORTS MAPPING | | | | | | | |
| NAME | | FUNCTION | | MCU PIN | | DEFAULT SET | |
| UART1 | | TX | | PA9 | | - | |
| | | RX | | PA10 | | RC Receiver 1 TX | |
| UART2 | | TX | | PA2 | | XBee RX | |
| | | RX | | PA3 | | XBee TX | |
| UART3 | | TX | | PC10 | | GPS RX | |
| | | RX | | PC11 | | GPS TX | |
| UART4 | | TX | | PA0 | | SERVO_5 | |
| | | RX | | PA1 | | SERVO_6 | |
| UART5 | | TX | | PC12 | | GPIO PC12 | |
| | | RX | | PD2 | | RC Receiver 2 TX | |
| UART6 | | TX | | PC6 | | SERVO_1 | |
| | | RX | | PC7 | | SERVO_2 | |
| Sheet Title: | | Documentation.SchDoc | | | | | |
| Project Title: | | UARG Autopilot.PrjPcb | | | | | |
| Company: | | UARG Autopilot.PrjPcb | | | | | |
| Size: | | Number: | | Rev: 2.0 | | Sheet 15 of 16 | |
| Date: | | 20-DEC-2015 | | Drawn by: | | Eng. Jorge Marin (marinm@ualberta.ca) | |
| 1 | | 2 | | 3 | | 4 | |

| | | | | | | | |
|--------------------------------------|--|----------|--|--|--|----------------|--|
| 1 | | 2 | | 3 | | 4 | |
| REVISION HISTORY | | | | | | | |
| DATE | | REVISION | | DESCRIPTION | | | |
| 09-DEC-2015 | | 1.0 | | Initial Release | | | |
| A | | B | | C | | D | |
| Revision History.SchDoc | | | | | | | |
| Project Title: UARG Autopilot.PrjPcb | | | | | | | |
| Company: | | | | | | | |
| Size: A | | Number: | | Rev: 2.0 | | Sheet 16 of 16 | |
| Date: 20-DEC-2015 | | Sheet 16 | | Drawn by: Eng. Jorge Marin (jmarinm@ualberta.ca) | | | |
| 1 | | 2 | | 3 | | 4 | |
| A | | B | | C | | D | |

4.5 Autopilot Board Bill-of-Materials (BOM)

This section contains the list of components used in the design of board, including manufacturer and part numbers.

| Designator | Quantity | Value | Manufacturer | Manufacturer Part Number |
|--|----------|--------|---|--------------------------|
| C1, C2 | 2 | 10pF | Yageo | CC0402JRNPO9BN100 |
| C3, C4, C5, C23, C36, C49, C67, C80 | 8 | 2.2uF | Yageo | CC0402MRX5R5BB225 |
| C6, C24 | 2 | 4.7uF | Yageo | CC0603KRX5R6BB475 |
| C7, C8, C9, C10, C12, C13, C15, C16, C19, C20, C22, C35, C48, C52, C53, C54, C55, C56, C66, C79, C83 | 21 | 100nF | Yageo | CC0402KRX7R6BB104 |
| C11 | 1 | 1uF | Yageo | CC0402KRX5R5BB105 |
| C14 | 1 | 2.2nF | Yageo | CC0402KRX7R9BB222 |
| C17, C38, C51, C69, C82 | 5 | 4.7uF | Yageo | CC0402MRX5R6BB475 |
| C18 | 1 | 220nF | Yageo | CC0402KRX5R5BB224 |
| C21 | 1 | 33uF | Kemet | T491A336K010AT |
| C25, C37, C50, C68, C81 | 5 | 10nF | Yageo | CC0402KRX7R7BB103 |
| C27, C40, C58, C71 | 4 | 0.47uF | Yageo | CC0402ZRY5V7BB474 |
| C28, C41, C59, C72 | 4 | 10uF | Samsung Electro-Mechanics America, Inc. | CL32B106KBJNNNE |
| C29, C42, C60, C73 | 4 | 4.7uF | Samsung Electro-Mechanics America, Inc. | CL32B475KBUYNNE |
| C30, C43, C61, C74 | 4 | 100pF | Yageo | CC0402JRNPO9BN101 |
| C31, C32, C44, C45, C62, C63, C75, C76 | 8 | 47uF | Murata Electronics North America | GRM32ER71A476KE15L |
| C33, C46, C64, C77 | 4 | 10uF | Yageo | CC0805KKX5R7BB106 |
| C34, C47, C65, C78 | 4 | 100nF | Yageo | CC0603KPX7R7BB104 |
| C85, C86 | 2 | 8.2pF | Yageo | CC0402BRNPO9BN8R2 |
| C87 | 1 | 11mF | Seiko Instruments | CPH3225A |
| C88 | 1 | 33nF | Samsung Electro-Mechanics America, Inc. | CL05B333JO5NNNC |
| C89 | 1 | 470pF | TDK Corporation | C1005COG1H471J050BA |
| D1, D2 | 2 | | Toshiba Semiconductor and Storage | CMS04(Te12L,Q,M) |
| D3 | 1 | | Diodes Incorporated | 1N5819HW-7-F |
| D4 | 1 | | Micro Commercial Co | 1N4148WX-TP |
| EX1, EX2 | 2 | | Sullins Connector Solutions | NPPN101BFCN-RC |
| J6, J11, J12, J13, J14, J20 | 6 | | Molex, LLC | 0533980471 |
| J16 | 1 | | 3M | 961106-5500-AR-PR |
| J17 | 1 | | Hirose Electric Co Ltd | U.FL-R-SMT(10) |
| J18 | 1 | | Cinch Connectivity Solutions Johnson | 142-0701-801 |
| J19 | 1 | | Molex, LLC | 0533980771 |
| J21 | 1 | | Molex, LLC | 0533980571 |
| JTAG1 | 1 | | Samtec Inc. | FTSH-105-01-F-DV-K |
| L1 | 1 | | Murata Electronics North America | BLM15AX1025N1D |
| L2, L3, L4, L5 | 4 | 6.8uH | Vishay Dale | IHL P3232DZER6R8M11 |
| L6 | 1 | 6.8nH | Murata Electronics North America | LQW15AN6N8HOOD |
| L7 | 1 | 27nH | Murata Electronics North America | LQW15AN27NJ00D |
| LED1, LED5 | 2 | | Lite-On Inc. | LTST-C190KRKT |
| LED2 | 1 | | Lite-On Inc. | LTST-C190AKT |
| LED3, LED6, LED8, LED9 | 4 | | Lite-On Inc. | LTST-C190KGKT |
| LED4, LED7 | 2 | | Lite-On Inc. | LTST-C190YKT |
| Q1 | 1 | | Diodes Incorporated | MMDT5551-7-F |
| Q2 | 1 | | NXP Semiconductors | BSS138PS,115 |
| R67 | 13 | 0 | Yageo | RC0402JR-070RL |
| R2 | 1 | 9.1K | Yageo | RC0603FR-079K1L |
| R3 | 1 | 2.2K | Yageo | RC0603FR-072K2L |
| R6, R10 | 2 | 1K | Yageo | RC0402FR-071KL |
| R7, R8, R11, R12, R15, R23, R42, R43, R44, R45, R65 | 11 | 10K | Yageo | RC0402FR-0710KL |
| R13, R14 | 2 | 2.2K | Yageo | RC0402FR-072K2L |
| R16 | 1 | 120 | Yageo | RC0402FR-07120RL |
| R18 | 1 | 470 | Yageo | RC0402JR-07470RL |

| | | | | |
|-------------------------|---|------|--|-----------------------|
| R22, R27, R34, R50, R57 | 5 | 100K | Yageo | RC0402FR-07100KL |
| R24, R31, R47, R54 | 4 | 1Meg | Rohm Semiconductor | MCR01MRTF1004 |
| R25, R32, R48, R55 | 4 | 453K | Yageo | RC0603FR-07453KL |
| R28, R35, R51, R58 | 4 | 249K | Rohm Semiconductor | MCR01MRTF2493 |
| R30, R37, R53, R60 | 4 | 100K | Yageo | RC0603FR-07100KL |
| R38, R39 | 2 | 200K | Yageo | RC0402FR-07200KL |
| R61 | 1 | 100 | Yageo | RC0402FR-07100RL |
| R68 | 1 | 10 | Yageo | RC0402FR-0710RL |
| RN1, RN2, RN8, RN9 | 4 | 1K | Yageo | YC164-JR-071KL |
| RN3 | 1 | 10K | Yageo | YC164-JR-0710KL |
| RN4, RN5 | 2 | 2.2K | Yageo | YC164-JR-072K2L |
| RN6, RN7 | 2 | 470 | Yageo | YC164-JR-07470RL |
| S1 | 1 | | C&K Components | KMR221GLFS |
| U1 | 1 | | STMicroelectronics | STM32F405RGT6 |
| U2 | 1 | | Measurement Specialties, Inc. | MS5611-01BA03 |
| U3 | 1 | | InvenSense | MPU-6000 |
| U4 | 1 | | Honeywell Microelectronics & Precision Sensors | HMC5883L-TR |
| U5 | 1 | | Maxim Integrated | MAX3051EKA+T |
| U6 | 1 | | Texas Instruments | LM3940IMPX-3.3/NOPB |
| U7 | 1 | | Texas Instruments | LP2992AIM5-3.3/NOPB |
| U8, U10, U19, U21 | 4 | | Texas Instruments | LM43603PWPT |
| U13, U14 | 2 | | Texas Instruments | PCA9306DCTR |
| U15, U16 | 2 | | Texas Instruments | SN74LVC125APWR |
| U17 | 1 | | GLOBAL CONNECTOR TECHNOLOGY | MEM2051-00-195-00-A |
| U18 | 1 | | Atmel | ATMEGA328P-AU |
| U23 | 1 | | u-blox | MAX-7Q |
| U24 | 1 | | Murata Electronics North America | SF1186K-3 |
| U25 | 1 | | Maxim Integrated | MAX2659ELT+T |
| USB1 | 1 | | Molex, LLC | 0473460001 |
| Y1 | 1 | | Abracon LLC | ABM8G-12.000MHZ-4Y-T3 |
| Y2 | 1 | | Murata Electronics North America | CSTCE16MOV53-R0 |
| Z1, Z2 | 2 | | Bourns Inc. | CG0603MLC-05LE |

5 Revision History

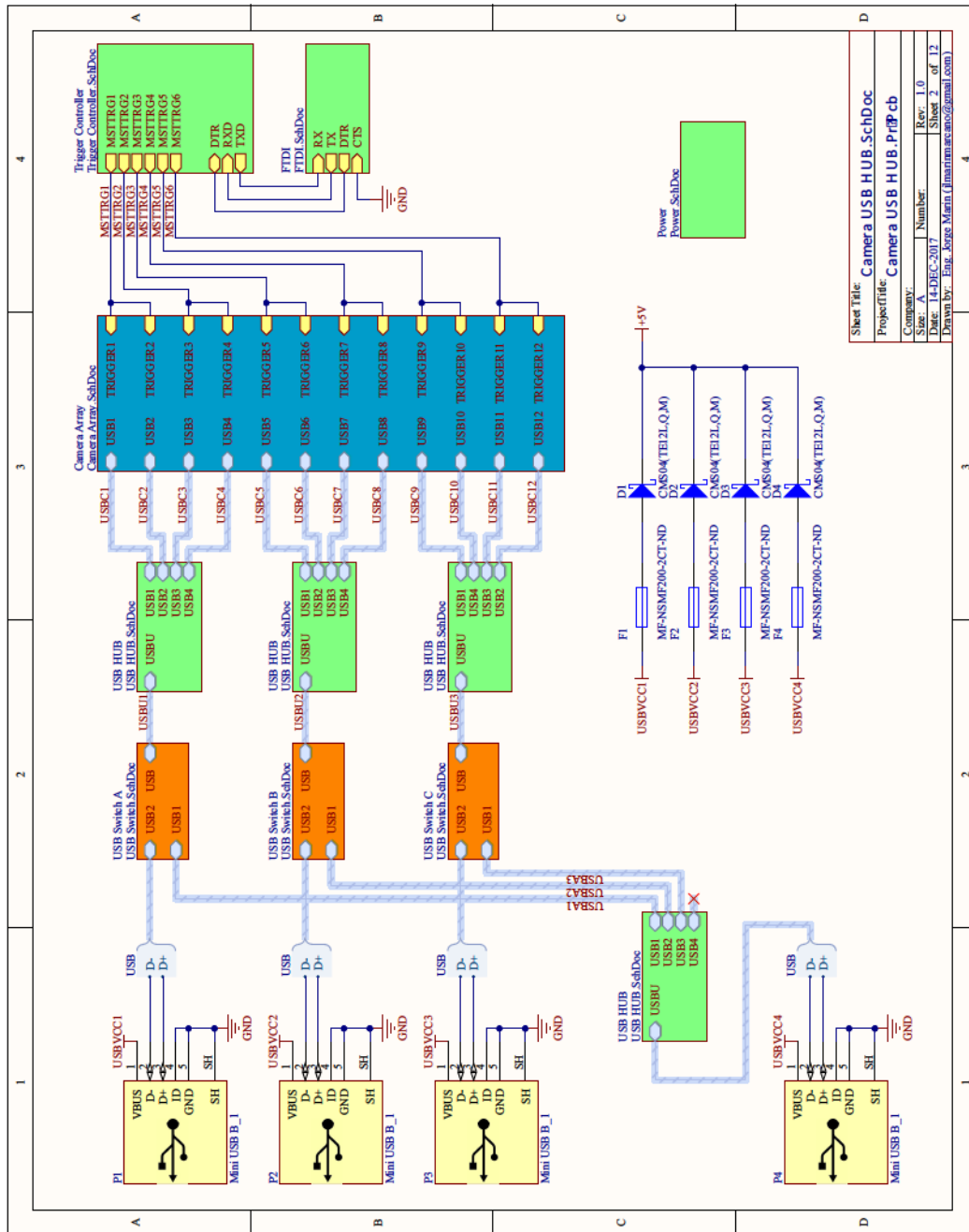
Table 5.1: Falcon I Autopilot Board User Guide Revision History.

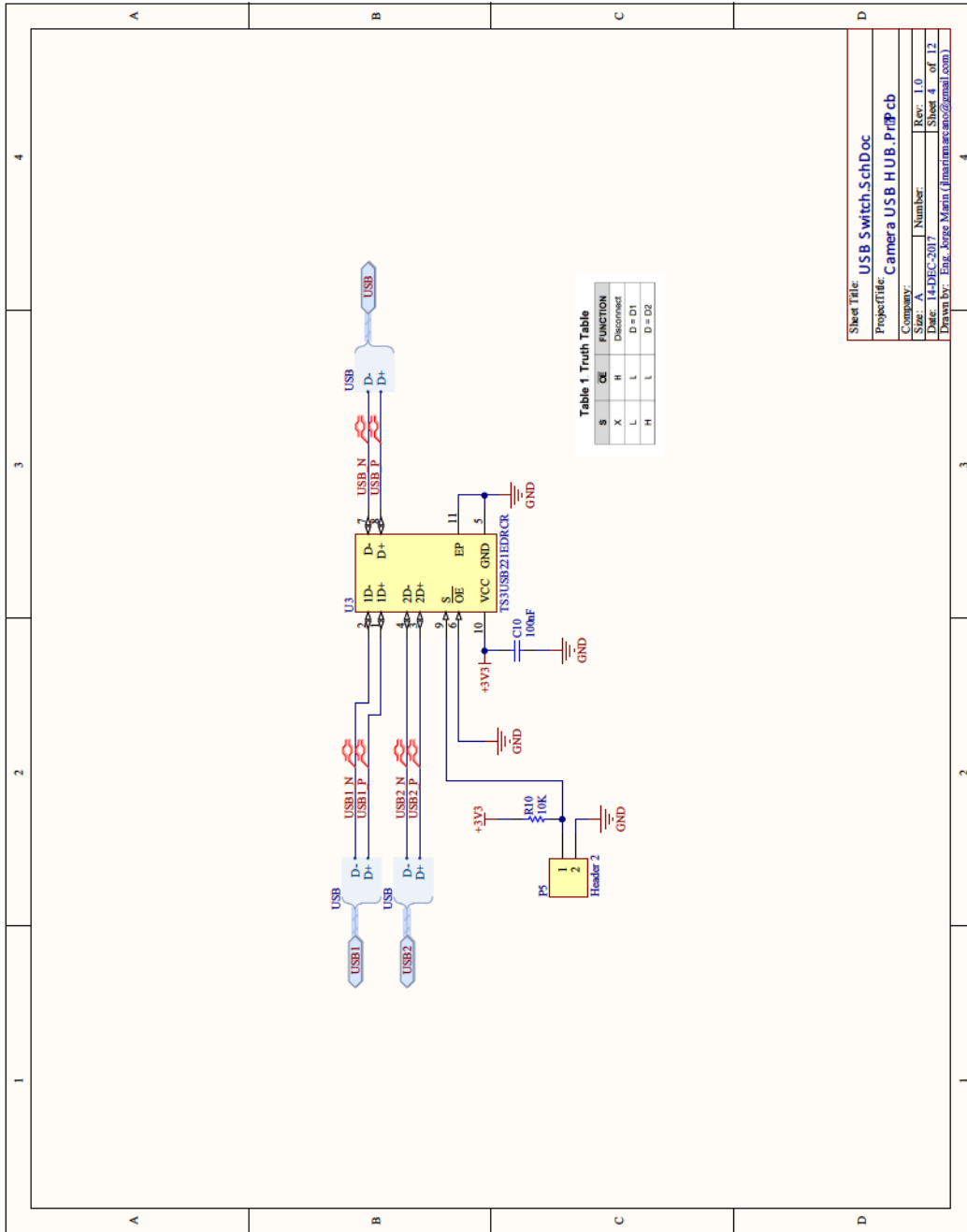
| Rev. | Date | Changes |
|------|-------------|--|
| 1.0 | 04-Aug-2016 | First issue. |
| 1.1 | 29-Nov-2016 | Changed board name, updated introduction and updated jumper table to indicate default jumpers. Added note on solder jumpers section. |
| 1.2 | 04-Jan-2017 | Fixed typographic errors and updated IMU and GPS paragraphs. |
| 1.3 | 25-Jan-2017 | Updated cover page picture and added board pictures section. |
| 1.4 | 15-Mar-2018 | Added text link to STM32 MCU datasheet. Updated block diagram. |
| 1.5 | 29-Mar-2018 | Updated authors. Added BOM. |

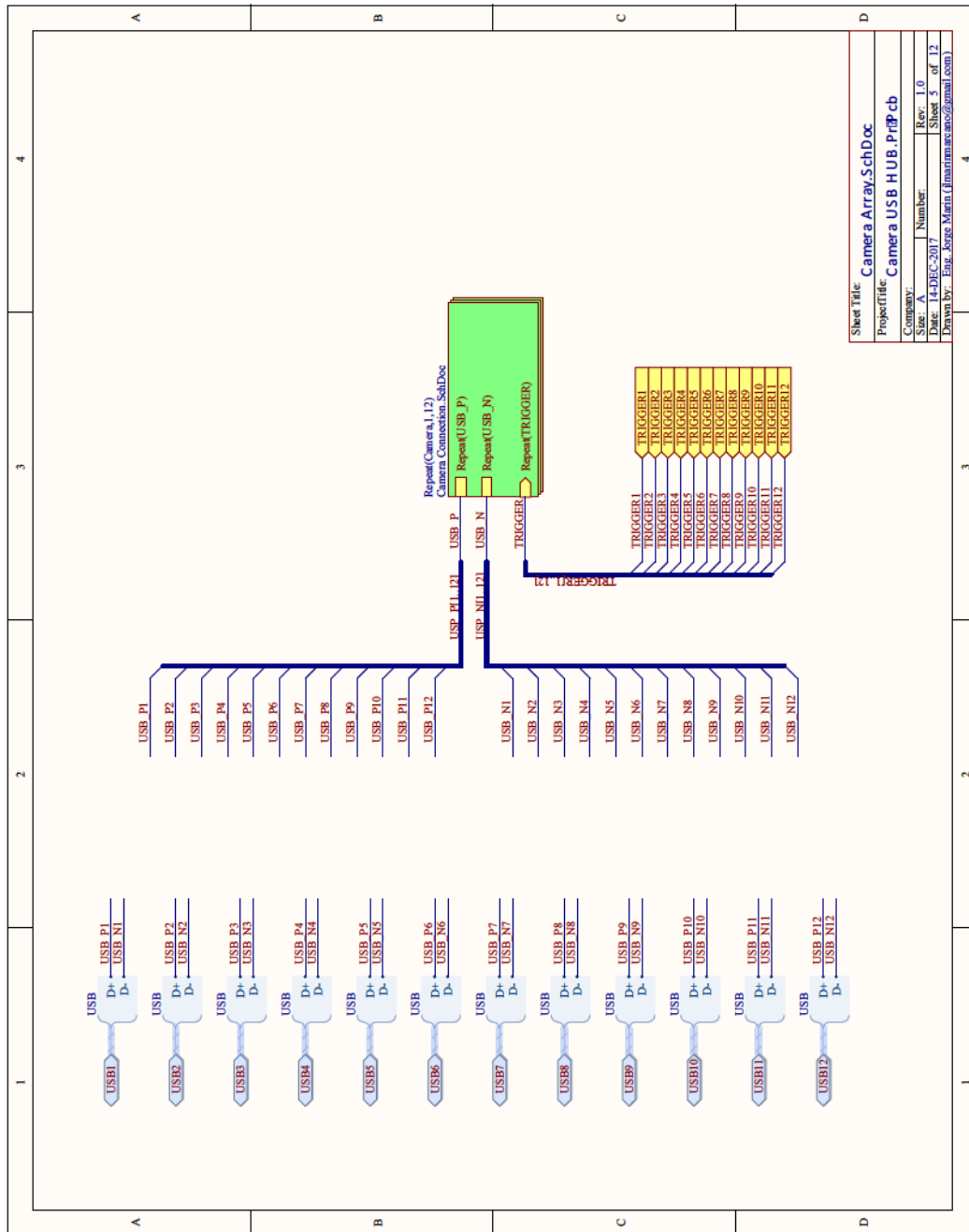
Appendix B

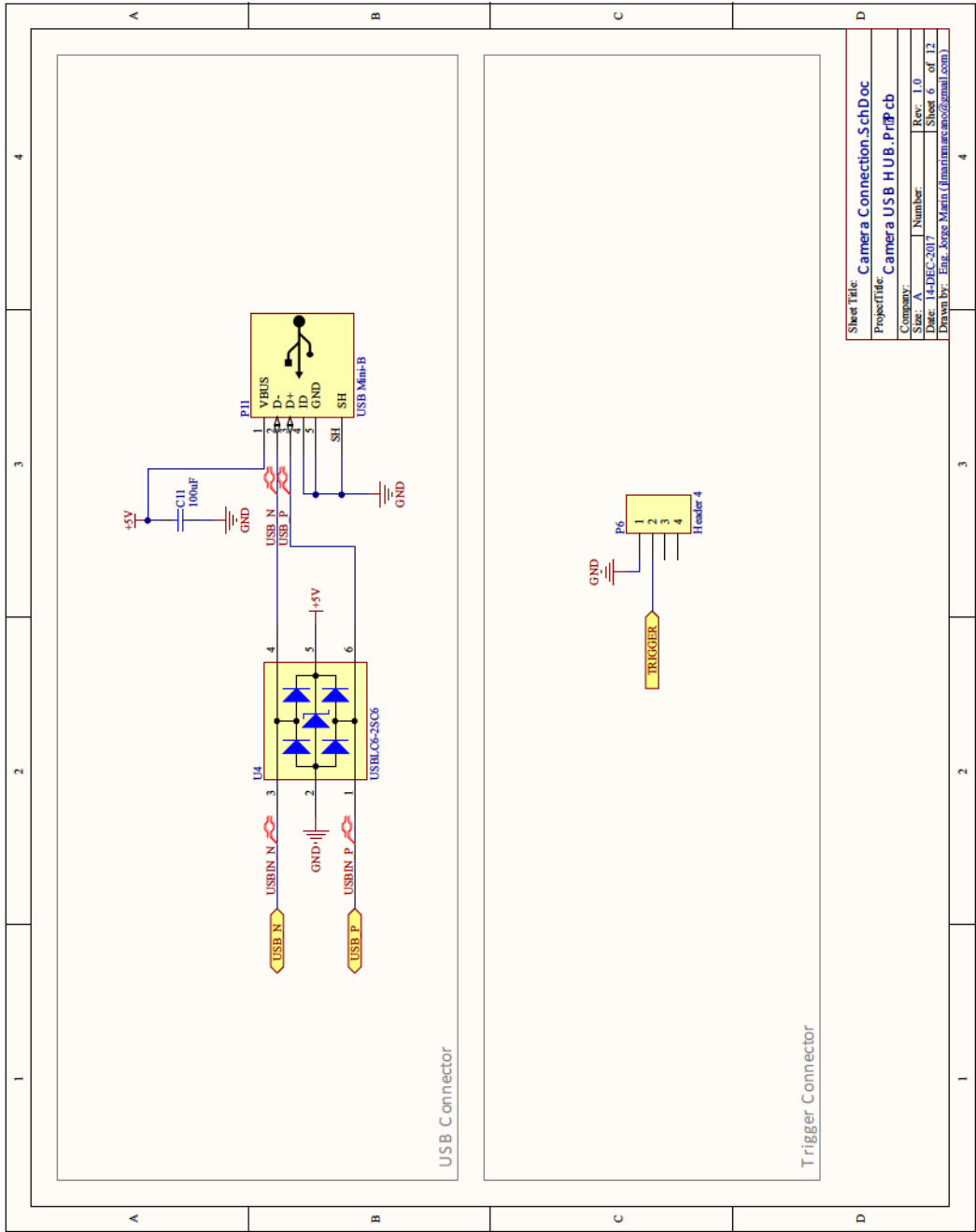
Camera Bridge Board Schematics

| | | | |
|--|---|---|---|
| 1 | 2 | 3 | 4 |
| Project Title: Camera USB HUB.PrjPcb Revision: 1.0 Date: 14-DEC-2017 | | | |
| A | B | C | D |
| Blocks | | | |
| U. Camera USB HUB Camera USB HUB.SchDoc | | | |
| U. Notes Notes.SchDoc | | | |
| U. Documentation Documentation.SchDoc | | | |
| U. Revision History Revision History.SchDoc | | | |
| Sheet Title: Index.SchDoc Project Title: Camera USB HUB.PrjPcb Company: A Size: A Date: 14-DEC-2017 Drawn by: Eng. Jorge Maria (jmaria@cambo.com) | | | |
| 1 | 2 | 3 | 4 |

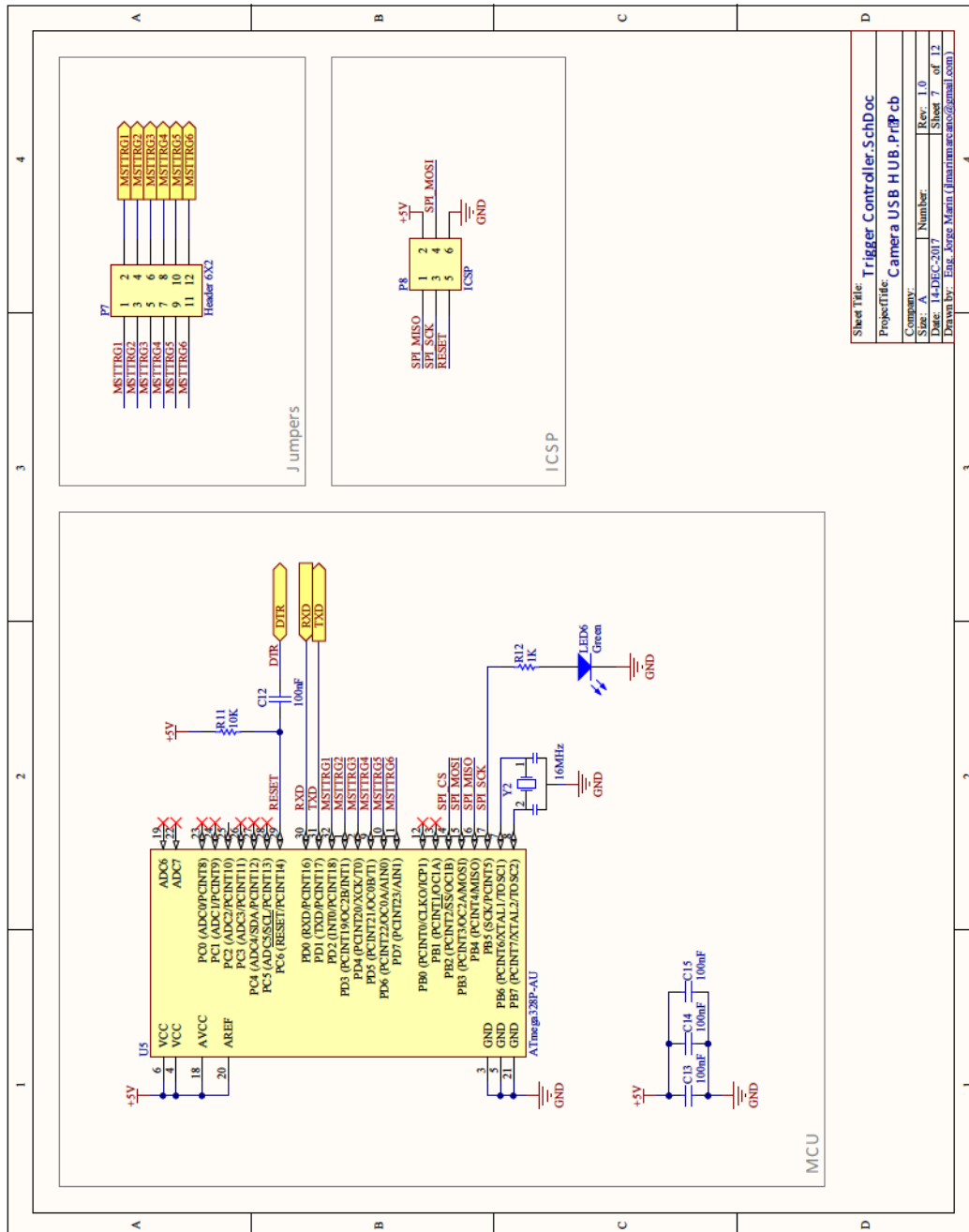


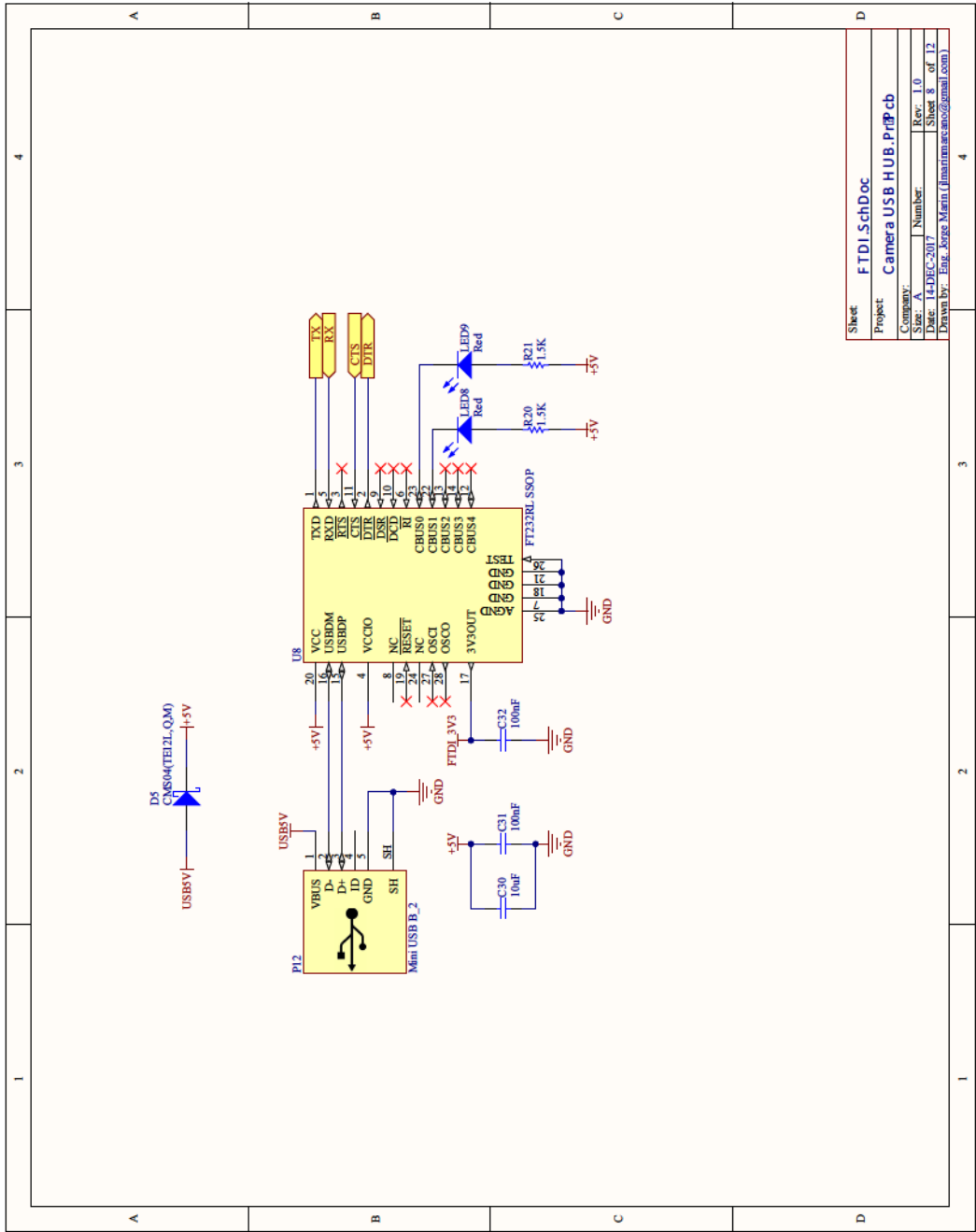




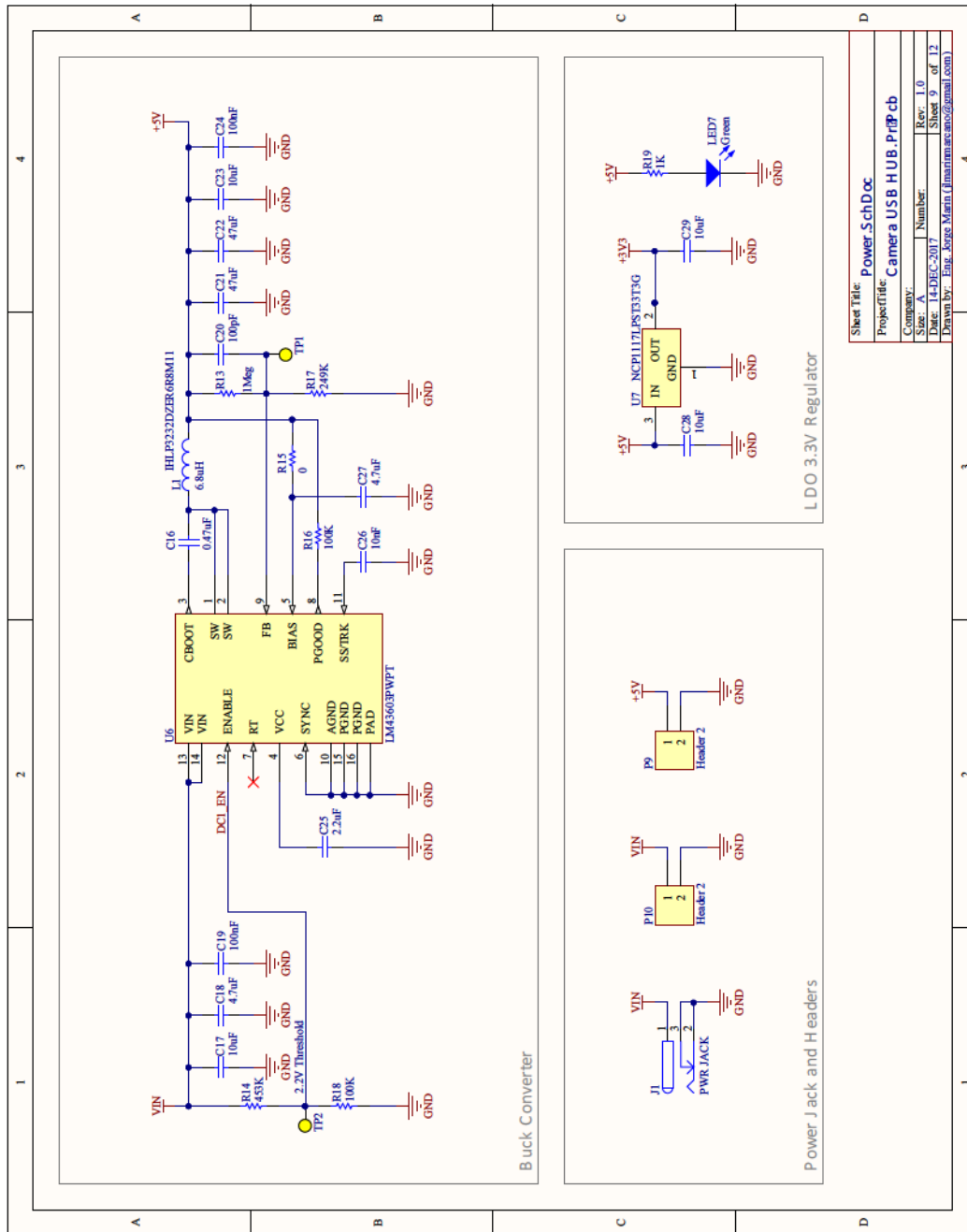


| | |
|--------------|------------------------------------|
| Sheet Title: | Camera Connection.SchDoc |
| Project: | Camera USB HUB.Prip.cb |
| Company: | |
| Size: | A |
| Date: | 14-DEC-2017 |
| Drawn by: | Engr. Jorge Maria (jmaria@mac.com) |
| Rev: | 1.0 |
| Sheet 6 | of 12 |





| | |
|----------|---|
| Sheet | FTDI.SchDoc |
| Project | Camera USB HUB.Prip.cb |
| Company | |
| Size | Number |
| Date | Rev: 1.0 |
| Drawn by | Sheet 8 of 12 |
| | Drawn by: Eng. Jorge Maria (jmaria@mac.com) |



| 1 | | 2 | | 3 | | 4 | | | | | | | | | |
|---|---|----------|-------------|---|---|--|--|--|-------------|---|---|--|--|--|--|
| <div><div>General Notes</div><div>General notes relating to the design.</div><table border="1"><thead><tr><th>Note No.</th><th>Description</th></tr></thead><tbody><tr><td colspan="2" rowspan="2"></td></tr></tbody></table></div> | | Note No. | Description | | | <div><div>PCB Layout Requirements</div><div>Layout notes referring to specific components or group of components are indicated on the schematic by the note number, enclosed in boxes, relevant to the component. Eg [1].</div><table border="1"><thead><tr><th>[Number]</th><th>Description</th></tr></thead><tbody><tr><td>[1]</td><td>90ohm impedance for USB differential pairs.</td></tr></tbody></table></div> | | [Number] | Description | [1] | 90ohm impedance for USB differential pairs. | <div><div>Fiducials</div><div><div>FID1</div><div>FID2</div><div>FID3</div></div><div>FIDUCIALS 3X TOP</div></div> | | <div><div>Mounting Holes</div><div><div>MH1</div><div>MH2</div><div>MH3</div><div>MH4</div></div><div>BOARD MOUNTING HOLES</div><div>Mounting Holes 3.175mm (125mil) pad, 5.714mm (225mil) drill</div></div> | |
| Note No. | Description | | | | | | | | | | | | | | |
| | | | | | | | | | | | | | | | |
| | | [Number] | Description | | | | | | | | | | | | |
| [1] | 90ohm impedance for USB differential pairs. | | | | | | | | | | | | | | |
| <div><div>PCB Assembly Variations</div><div>List of assembly variations. Variants are designated with a letter starting from A. The description shows the Variant name in brackets and then any comments.</div><table border="1"><thead><tr><th>Variant</th><th>Description</th></tr></thead><tbody><tr><td>A</td><td>[Prototype A] Straight mini USB connectors.</td></tr><tr><td>B</td><td>[Prototype B] R/A mini USB connectors.</td></tr></tbody></table></div> | | Variant | Description | A | [Prototype A] Straight mini USB connectors. | B | [Prototype B] R/A mini USB connectors. | <div><div>Mechanical</div><div>Copyright section (if applicable)</div></div> | | <div><div>Sheet Title: Notes.SchDoc</div><div>Projectfile: Camera USB HUB.PrjPcb</div><div>Company:</div><div>Size: A</div><div>Date: 14-DEC-2017</div><div>Drawn by: Eng. Jorge Marin (jmarin@cambo@gmail.com)</div><div>Number:</div><div>Rev: 1.0</div><div>Sheet 10 of 12</div></div> | | | | | |
| Variant | Description | | | | | | | | | | | | | | |
| A | [Prototype A] Straight mini USB connectors. | | | | | | | | | | | | | | |
| B | [Prototype B] R/A mini USB connectors. | | | | | | | | | | | | | | |
| 1 | | 2 | | 3 | | 4 | | | | | | | | | |

Appendix C

Camera Bridge Board Bill-of-Materials

| Designator | Quantity | Value | Manufacturer | Manufacturer Part Number |
|---|----------|--------|---|--------------------------|
| C1_USB HUB1, C1_USB HUB2, C1_USB HUB3, C1_USB HUB4, C5_USB HUB1, C5_USB HUB2, C5_USB HUB3, C5_USB HUB4, C6_USB HUB1, C6_USB HUB2, C6_USB HUB3, C6_USB HUB4, C8_USB HUB1, C8_USB HUB2, C8_USB HUB3, C8_USB HUB4, C9_USB HUB1, C9_USB HUB2, C9_USB HUB3, C9_USB HUB4, C30 | 21 | 10uF | Yageo | CC0603MRX5R5BB106 |
| C2_USB HUB1, C2_USB HUB2, C2_USB HUB3, C2_USB HUB4, C3_USB HUB1, C3_USB HUB2, C3_USB HUB3, C3_USB HUB4 | 8 | 20pF | Yageo | CC0603JRNPO9BN200 |
| C4_USB HUB1, C4_USB HUB2, C4_USB HUB3, C4_USB HUB4 | 4 | 10nF | Yageo | CC0603KRX7R8BB103 |
| C7_USB HUB1, C7_USB HUB2, C7_USB HUB3, C7_USB HUB4, C10_USB Switch A, C10_USB Switch B, C10_USB Switch C, C12, C13, C14, C15, C24, C31, C32 | 14 | 100nF | Yageo | CC0603KRX7R9BB104 |
| C11_Camera1, C11_Camera2, C11_Camera3, C11_Camera4, C11_Camera5, C11_Camera6, C11_Camera7, C11_Camera8, C11_Camera9, C11_Camera10, C11_Camera11, C11_Camera12 | 12 | 100uF | Murata Electronics | GRM31CR60J107ME39K |
| C16 | 1 | 0.47uF | Yageo | CC0402ZRY5V7BB474 |
| C17 | 1 | 10uF | Samsung Electro-Mechanics America, Inc. | CL32B106KBJNNNE |
| C18 | 1 | 4.7uF | Samsung Electro-Mechanics America, Inc. | CL32B475KBUYNNE |
| C19 | 1 | 100nF | Yageo | CC0402KRX7R6BB104 |
| C20 | 1 | 100pF | Yageo | CC0402JRNPO9BN101 |
| C21, C22 | 2 | 47uF | Murata Electronics North America | GRM32ER71A476KE15L |
| C23, C28, C29 | 3 | 10uF | Yageo | CC0805ZKY5V6BB106 |
| C25 | 1 | 2.2uF | Yageo | CC0402MRX5R5BB225 |
| C26 | 1 | 10nF | Yageo | CC0402KRX7R7BB103 |
| C27 | 1 | 4.7uF | Yageo | CC0402MRX5R6BB475 |
| D1, D2, D3, D4, D5 | 5 | | Toshiba Semiconductor and Storage | CMS04(Te12L,Q,M) |
| F1, F2, F3, F4 | 4 | | Bourns Inc. | MF-NSMF200-2 |
| J1 | 1 | | CUI-Inc. | PJ-075CH-SMT-TR |
| L1 | 1 | 6.8uH | Vishay Dale | IHLP3232DZER6R8M11 |

| | | | | |
|--|----|------|---------------------|------------------|
| LED1_USB HUB1, LED1_USB HUB2, LED1_USB HUB3, LED1_USB HUB4, LED2_USB HUB1, LED2_USB HUB2, LED2_USB HUB3, LED2_USB HUB4, LED3_USB HUB1, LED3_USB HUB2, LED3_USB HUB3, LED3_USB HUB4, LED4_USB HUB1, LED4_USB HUB2, LED4_USB HUB3, LED4_USB HUB4, LED6, LED7 | 18 | | Kingbright | APT1608SGC |
| LED5_USB HUB1, LED5_USB HUB2, LED5_USB HUB3, LED5_USB HUB4, LED8, LED9 | 6 | | Kingbright | APT1608SURCK |
| P1, P2, P3, P4, P12 | 5 | | TE Connectivity AMP | 1734510-1 |
| P6_Camera1, P6_Camera2, P6_Camera3, P6_Camera4, P6_Camera5, P6_Camera6, P6_Camera7, P6_Camera8, P6_Camera9, P6_Camera10, P6_Camera11, P6_Camera12 | 12 | | Molex,-LLC | 530480410 |
| P11_Camera1, P11_Camera2, P11_Camera3, P11_Camera4, P11_Camera5, P11_Camera6, P11_Camera7, P11_Camera8, P11_Camera9, P11_Camera10, P11_Camera11, P11_Camera12 | 12 | | Hirose Electric | UX20-MB-5P |
| R1_USB HUB1, R1_USB HUB2, R1_USB HUB3, R1_USB HUB4, R3_USB HUB1, R3_USB HUB2, R3_USB HUB3, R3_USB HUB4, R10_USB Switch A, R10_USB Switch B, R10_USB Switch C, R11 | 12 | 10K | Yageo | AC0603FR-0710KL |
| R2_USB HUB1, R2_USB HUB2, R2_USB HUB3, R2_USB HUB4, R4_USB HUB1, R4_USB HUB2, R4_USB HUB3, R4_USB HUB4, R5_USB HUB1, R5_USB HUB2, R5_USB HUB3, R5_USB HUB4, R18 | 13 | 100K | Yageo | RC0603FR-07100KL |
| R6_USB HUB1, R6_USB HUB2, R6_USB HUB3, R6_USB HUB4 | 4 | 2.7K | Yageo | RC0603FR-072K7L |
| R7_USB HUB1, R7_USB HUB2, R7_USB HUB3, R7_USB HUB4, R8_USB HUB1, R8_USB HUB2, R8_USB HUB3, R8_USB HUB4, R9_USB HUB1, R9_USB HUB2, R9_USB HUB3, R9_USB HUB4, R12, R19 | 14 | 1K | Yageo | RC0603FR-071KL |
| R13 | 1 | 1Meg | Rohm Semiconductor | MCR01MRTF1004 |
| R14 | 1 | 453K | Yageo | RC0603FR-07453KL |
| R15 | 1 | 0 | Yageo | RC0402JR-070RL |
| R16 | 1 | 100K | Yageo | RC0402FR-07100KL |
| R17 | 1 | 249K | Rohm Semiconductor | MCR01MRTF2493 |
| R20, R21 | 2 | 1.5K | Yageo | RC0603FR-071K5L |

| | | | | |
|---|----|--|---|------------------|
| U1_USB HUB1, U1_USB HUB2, U1_USB HUB3, U1_USB HUB4 | 4 | | Terminus Tech | FE1.1s |
| U3_USB Switch A, U3_USB Switch B, U3_USB Switch C | 3 | | Texas Instruments | TS3USB221EDRCR |
| U4_Camera1, U4_Camera2, U4_Camera3, U4_Camera4, U4_Camera5, U4_Camera6, U4_Camera7, U4_Camera8, U4_Camera9, U4_Camera10, U4_Camera11, U4_Camera12 | 12 | | STMicroelectronics | USBLC6-2SC6 |
| U5 | 1 | | Atmel | ATMEGA328P-AU |
| U6 | 1 | | Texas Instruments | LM43603PWPT |
| U7 | 1 | | ON Semiconductor | NCP1117LPST33T3G |
| U8 | 1 | | FTDI, Future Technology Devices International Ltd | FT232RL-REEL |
| Y1_USB HUB1, Y1_USB HUB2, Y1_USB HUB3, Y1_USB HUB4 | 4 | | ECS International | ECS-120-20-33-TR |
| Y2 | 1 | | Murata Electronics North America | CSTCE16MOV53-R0 |

Appendix D

3D Printer Settings

The following table summarizes the settings used for 3D printing the PLA parts.

Table D.1: 3D printer settings.

| Setting | Units | Value |
|----------------------|-------|-----------------------|
| Layer Height | mm | 0.18 |
| First Layer Height | mm | 0.27 |
| Perimeter Shells | | 2 |
| Top Solid Layers | | 3 |
| Bottom Solid Layers | | 3 |
| Fill Density | % | 15-20 |
| Fill Pattern | | Hexagonal (Honeycomb) |
| Combine Infill | | Every 2 Layers |
| Print Speed | mm/s | 60 |
| Travel Speed | mm/s | 80 |
| Extruder Temperature | °C | 200 |
| Platform Temperature | °C | 50 |